UNIVERSITA' DEGLI STUDI DI PAVIA

FACOLTA' DI INGEGNERIA
DIPARTIMENTO DI INGEGNERIA INDUSTRIALE E DELL'INFORMAZIONE

DOTTORATO DI RICERCA IN BIOINGEGNERIA E BIOINFORMATICA
XXXVII CICLO - 2024

Engineered living materials for sustainable and green applications

PhD Thesis by
FRANCESCA USAI

Advisor:
Prof. Lorenzo Pasotti
Prof. Paolo Magni

PhD Program Chair:
Prof. Silvana Quaglini

Abstract

This PhD thesis investigates the development of engineered living materials (ELMs) for applications in biosensing, biomanufacturing, and environmental sustainability. By combining synthetic biology, bioprinting, and material science, this research focuses on creating functional bacterial systems capable of operating in real-world conditions, with potential use in diagnosis, agricultural monitoring, and carbon capture technologies.

In the first section, a robust bioprinting workflow was developed to fabricate bacterial biosensors. These devices were tested in diverse environments, including nutrient-poor water samples and complex clinical matrices such as culture supernatants and bronchial aspirates. The biosensors demonstrated efficient detection of target molecules, such as bacterial autoinducers from *Vibrio fischeri*, and *Pseudomonas aeruginosa*, under varying conditions. Viability and functional stability of the bioprinted materials were maintained for over two weeks, and the devices could be stored for up to one month under refrigeration. Additionally, incorporating multiple bacterial strains into the biosensors allowed for multiplexed sensing and cell-cell communication, significantly increasing the complexity and utility of the biosensing devices. This work laid the foundation for automating bioprinting processes and designing bacterial-laden biosensors for environmental monitoring and clinical applications.

The second phase of the thesis focused on agricultural and industrial applications, with an emphasis on developing biosensors for detecting volatile organic compounds (VOCs), acetate, nitrates, and phosphates. In particular, these biosensors were proposed as tools to improve sustainable fertilization practices by monitoring nutrient levels in soil, thereby reducing environmental impacts and enhancing crop production, or to improve and optimize biogas processes. Eleven biosensors were characterized, revealing promising candidates for detecting the target molecules. However, factors such as pH and the presence of complex substances in soil and digestate samples affected sensor performance. This highlighted the need for extensive optimization to ensure reliable biosensing in field applications. A biocontainment strategy

using a PDMS-box with a PES filter membrane was also developed to prevent the escape of genetically modified organisms (GMOs), offering a robust solution for the safe deployment of ELMs outside of laboratory environments. Additionally, a low-cost, smartphone-based method for biosensor readout was successfully tested, demonstrating the potential for real-time monitoring in low-resource settings.

In the final section, cyanobacteria were explored as a platform for biomanufacturing and ELMs fro climate change mitigation. The fast growing cyanobacterium *Synechococcus elongatus* UTEX 2973 was engineered to either surface display or secrete proteins and enzymes for a wide range of applications, including therapeutics and carbon negative practices. A novel S-layer protein was characterized, enabling the secretion and display of industrially relevant enzymes. Furthermore, cyanobacteria-based living bricks capable of CO_2 fixation, biocement production, and self-repair were developed. These living bricks showed promising mechanical properties, but challenges such as uneven cell distribution and variability in biomineralization efficiency remain to be addressed. The research also explored the use of engineered carbonic anhydrase enzymes for improving CO_2 capture, with several variants showing potential for enhancing carbonate precipitation. Finally, strategies to improve cyanobacterial resilience in harsh environments, such as desiccation, were investigated by leveraging the expression of tardigrade derived proteins (TDPs), further supporting their use in challenging environmental conditions.

Overall, this PhD research advances the field of engineered living materials by demonstrating their potential for a wide range of applications, from biosensing in clinical and agricultural settings to carbon-negative biomanufacturing. Despite challenges related to sensor optimization and scalability, as well as the relatively limited research on cyanobacteria compared to *E. coli*, this work lays a robust foundation for the future development of sustainable living technologies.

Contents

List of Figures

Chapter 1

Background

1.1 Synthetic biology and its applications

The term synthetic biology appeared in the literature in 1980, when it was used by Barbara Hobom to describe bacteria that had been genetically engineered using recombinant DNA technology [1]. The ability to rationally engineer microrganisms has been a long envisioned goal [2], and thereafter made possible due to prior understanding of how cells and biological systems work, advances in DNA sequencing and synthesis [3]. Since the introduction of the first synthetic gene networks in living cells [4, 5], synthetic biology has emerged as a powerful tool to describe cells as complex information-processing systems, as well as design and build new genetic systems into a host organism, called *chassis*. According to the principles of standardization, modularity, abstraction, and prototyping, cells are engineered and reassembled to make novel biological systems, and each component specifications are well-documented and shared in open registries (e.g., MIT Registry of Standard Biological Parts).

Implementing new functions in known microrganisms means to engineer living cells by inserting exogenous DNA that codes for one or more proteins, making a synthetic circuit. The genetically engineered program is encoded at the DNA level, DNA constitutes these interchangeable parts as toy building bricks, and these bricks interface with each other to create devices into biological systems, following the Design-Build-Test-Learn cycle.

Plasmid-based vectors, circular double-stranded DNA molecules, are widely used to deliver a DNA-encoded gene circuit and are characterized by:

- a *cloning site* in which the circuit DNA can be inserted, that carries the information about the functionality we want to implement;

- an *origin of replication (ORI)* that determines how many copies of plasmid can replicate per cell;
- a *selection marker*, usually the resistance to an antibiotic, which has the purpose of allowing to select only the cells that have incorporated the plasmid upon antibiotic addition to the growth medium. This marker represents an advantage for the bacteria that have incorporated the plasmid, thereby making the lost of the plasmid more difficult, as the bacteria only survive if the genetic program is mantained.

The cloning site is the region that contains the essential parts needed for the genetic program to be implemented. The fundamental components for a gene circuit are:

- **Promoter**, that is a short DNA sequence recognized by RNA-polymerase, important for the initiation of transcription. The strength of a promoter, or transcription rate, is related to the affinity between RNA polymerase and associated factors with its specific DNA sequence. These sequences can be divided into two groups: constitutive, if the transcriptional rate is constant, or inducible, if it can be activated or repressed by transcriptional factor or exogenous molecules.
- **Ribosome binding site (RBS)** represents the sequence in the mRNA to which ribosomes bind to initiate translation. RBSs are located at the 5' UTR of the mRNA molecule, and they are transcribed in mRNA, but not translated into proteins. The absence of these sequences does not enable the binding of mRNA to ribosomes, reducing the translation efficiency. In many prokaryotes, RBSs contain a consensus sequence, known as Shine Dalgarno, which is not the same for all genes, but it is an average sequence obtained from the alignment of mRNA sequences.
- **Coding sequence (CDS)** is a DNA sequence located downstream of an RBS, that is transcribed by RNA polymerase in mRNA and translated in protein by ribosomes. CDSs, or genes, are flanked by a start codon (i.e., ATG) and a stop codon (i.e., TAA, TGA or TAG), respectively to start and stop the translation. In the context of synthetic biology, reporter genes are very useful for the characterization and debugging of biological systems. They encode for proteins whose amount is easily detectable, as fluorescent proteins (e.g., green fluorescent protein, GFP) or enzymes that can be quantified through specific fluorometric assay.
- **Terminators** are the sequences, downstream of the CDS, that determine the end of the transcription process. In prokaryotes, terminators

can be classified in two ways: rho-dependent or rho-independent. The former requires a protein called rho-factor to induce the detachment of RNA polymerase from DNA, the latter consists of a hair- pin containing a CG-rich base region, followed by a T-rich sequence, which allows the separation of RNA polymerase. An important parameter that characterizes the activity of terminator is the efficiency, that is the probability that a successful termination of transcription happens.

The combination of promoter, RBS, CDS and terminator constitutes an individual gene expression cassette. Synthetic circuits may include one or multiple cassettes to meet the design specifications and carry out complex regulatory tasks in living cells.

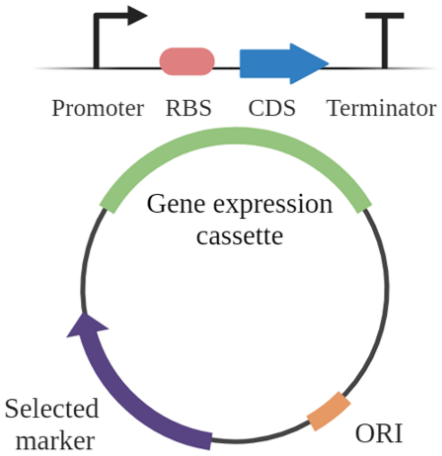

Figure 1.1: Plasmid structure. The structure of a plasmid vector is shown with its main characteristics: cloning site, origin of replication and selection marker. The cloning site includes the DNA insert of interest, which encodes the designed biological function in the form of a synthetic circuit. It comprises promoter, RBS, CDS and terminator.

However, for a more stable and robust recombinant protein expression, integration of the target gene into the genome is preferable, and various strategies have been established so far (e.g., recombineering).

Synthetic biology has always been driven by its practical applications to real-world challenges, impacting healthcare through therapeutic and diagnostic devices [6], as well as improving the environment making sustainable chemicals, fuels, and biomaterials [7]. As proof of this, literature of last decade is plenty of works studying engineered metabolic pathways in microorganisms for drug and biofuel production from renewable sources [8, 9],

biosensors for bioremediation applications [10, 11], solid tumor targeting [12], and also several information processing tasks, such as logic functions [13], waveform generation [14] and robust control [15].

1.2 Synthetic biosensors in bacteria

The term biosensor refers to a biological device which provides specific recognition of a certain target input, and this detection is transduced in an easily detectable and quantifiable output. Biosensors have a wide range of applications across different fields: medical disagnostics, where biosensors can be used to detect pathogens in clinical samples; environmental monitoring, to detect contaminants in water and soil sources; food safety and quality control (e.g., to detect foodborne pathogens or toxins), bioprocess monitoring (e.g., fermentation processes control), agriculture (e.g., for soil nutrient analysis), and security and defense (e.g., to detect unexploded mines).

Traditional detection methods, either based on culture and staining or on complex analytical instruments, are generally expensive. In contrast, a synthetic biology approach to the development of biosensing platforms is low cost and portable, and can be divided into two broad categories: whole-cell biosensors that rely on engineered gene circuits to detect and amplify signals and cell-free sensors that couple enzymatic reactions to user-friendly readouts. Here, the catogory of whole-cell biosensors is discussed in further detail since it represents the technology used in this thesis.

A whole-cell bacterial biosensor consists of a sensing module, often a transcription factor, that controls a signal processing module (i.e., an inducible promoter), which drives a reporting module (e.g., fluorescence). Fluorescent proteins are commonly used in whole-cell biosensors due to their unique and advantageous properties: they are expressed by a single gene; there is a wide variety of fluorescent proteins available, each emitting at different wavelengths (e.g., green, red, yellow), which allows for multiplexing-monitoring; they do not need any substrate; their ease of use and detection [16]. These properties make them highly valuable tools as reporting elements.

Advantages of genetically-encoded biosensors generally include low costs, high usability, and minimal requirement of sample preprocessing, equipment, trained personnel, and output post-processing [17].

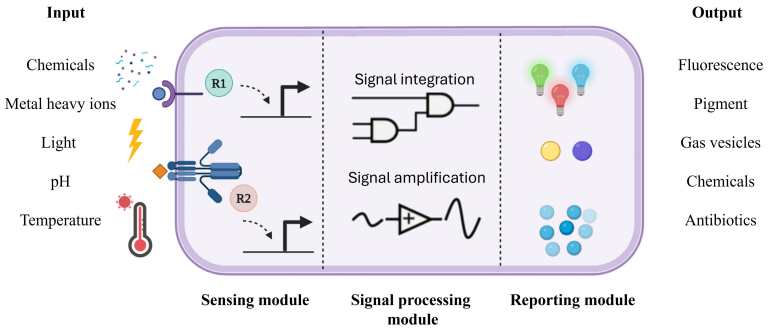

Figure 1.2: Modular and layered design of a synthetic biosensors. Sensing, processing and reporting modules are illustrated along with examples of physical or chemical inputs and outputs that engineered cells could process.

Key factors influencing the efficacy of a bacterial biosensor include its sensitivity (i.e., the lowest detectable analyte concentration), the dynamic range (i.e., the ratio between basal expression and maximum expression of the reporter gene), and the operating range (e.g., the concentrations of target which result in a change of the output). The specificity of biosensors is essential for ensuring reliable and accurate results, and represents the sensor's ability to differentiate between target and non-targeted entities in a sample. Low specificity results in false positives. Another important feature is the time required for the induction, which tipically takes hours, but it would be better for some applications, for instance in diagnosis, to obtain a faster response. Furthermore, a biosensor must detect the target analyte in a dose-dependent manner (often showing a Hill function curve) minimizing cross-talk, while the absence of the target should result in minimal leaky expression.

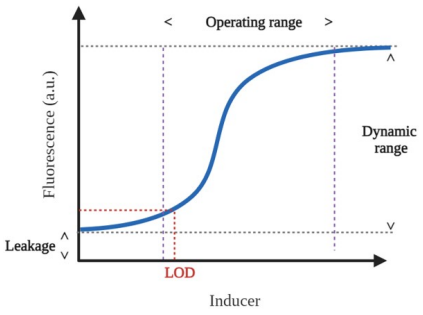

Figure 1.3: Dose and response curve of an ideal biosensor and its key characteristics in terms of operating and dynamic range are shown. The leakage, and the limit of detection (LOD), above referred as sensitivity, are also illustrated.

Examples of whole-cell biosensors for biomedical appications comprise all the devices conceived for diagnosis, often linked, but not limited, to the gut microbiome. There are many of sensors in literature developed to detect quorum sensing signal that mediates communication in both Gram negative and positive bacteria (e.g., AI-2, AHLs), which can be use as bacterial infection biomarkers [18, 19]. For instance, Raut and colleagues created and fine-tuned a biosensing system based on whole cells, enabling the quantitative detection of AI-2 quorum sensing molecules in human samples [20]. When applied to detect AI-2 in physiological specimens, the sensor demonstrated reproducibility, and high sensitivity, with a detection limit of 2.5 x 10^{-8} M. Noteworthy is the use of minimal unprocessed sample volumes (i.e., 1 μl of saliva and less than 1 mg of stool), making it particularly valuable for clinical applications.

A cutting-edge example of a wearable, cell-free biosensor system for chemicals and pathogen detection is represented by the work of Nguyen et al. [21]. They described flexible materials and fabrics enhanced with freeze-dried, cell-free synthetic circuits, including CRISPR-based technologies, designed to detect metabolites, chemicals, and pathogen nucleic acid markers. These wearable devices are activated when exposed to water and indicate the presence of specific molecular targets either through visible color changes or using an optical fiber system that detects fluorescent or luminescent signals. Their sensitivity to nucleic acids is comparable to standard lab techniques like quantitative PCR, achieving femtomolar sensitivities. As an example, they developed a face mask with a freeze-dried CRISPR sensor for noninvasive, wearable detection of SARS-CoV-2 at room temperature within 90 minutes, requiring only the push of a button from the user.

Another research area where whole-cell biosensors can be applied comprises the environmental applications, ranging from climate studies and agriculture to industrial pollution control. The work of Cardemil et al. offers an innovative approach to environmental monitoring, utilizing whole-cell biosensors for real-time data on water quality [22]. The authors developed two *E. coli*-based reporter systems for the measurement of phosphate and ammonia in coastal and suburban watersheds by fusing phoA and glnAp2 promoters in front of the luxCDABE operon of *Vibrio fischeri*, carried either on the chromosome or on a plasmid vector. The biosensors resulted in emission of bioluminescence in response to phosphate or ammonia starvation, with detection range respectively between 1-24 ppm and 0.1-1.6 ppm.

Monitoring bacterial contamination in water is another essential biosensing area for safeguarding human health. Engineered whole-cell biosensors developed through synthetic biology offer considerable potential for the fast and affordable detection of waterborne pathogens. In the work carried out

by Wu et al. [23], researchers designed a biosensor to identify water contamination caused by *Pseudomonas aeruginosa* and *Burkholderia pseudomallei*, two major bacterial pathogens that are commonly associated with waterborne diseases. The biosensor, developed in *E. coli*, works by detecting specific quorum sensing signal molecules produced by these bacteria, with an enhanced green fluorescent protein (eGFP) as reporting system. They then moved on to a paper-based device by embedding the lycopene-based whole-cell biosensor onto paper, aiming to create a prototype for a portable detection system. The biosensor offers a simple, low-cost solution for the timely, point-of-care identification of water contamination, contributing to the protection of human health.

Despite progress in engineering bacterial biosensors, many of them are characterized under laboratory settings, which tipically do not represent actual deployment conditions. The challenges we still need to face range from the reproducibility of the output, the difficulty of keeping cells alive, to the issues associated with accidental release or gene transfer from genetically modified organisms (GMOs). Biocontainment strategies should be employed and applied to microbial biosensors to prevent gene transfer, uptake of foreign DNA, or potentially harmful mutations.

1.3 Engineered living materials

Engineered living materials (ELMs) have rapidly emerged as a cutting-edge field, integrating biological systems into material design to create adaptive, and multifunctional structures. Over the last decade, significant advancements have been made, driven by interdisciplinary research at the intersection of synthetic biology, materials science, and bioengineering.

ELMs represent a new generation of smart materials composed by a living component (e.g., bacteria) from which they inherit the biological functions, and an abiotic component (e.g., hydrogel) serving as structural support. The creation of functional bacteria-laden structures can address various unmet societal needs across a range of applications, including therapeutics, environmental and industrial manufacturing.

Moreover, there have been advancements in the design of ELMs with tunable properties, enabling precise control over their biological and mechanical characteristics. By leveraging synthetic biology tools, researchers are now able to engineer cells with specific gene circuits that can regulate material properties in response to external stimuli. This level of control opens new possibilities for creating adaptive materials that can change their stiffness, permeability, depending on the environmental conditions or the needs of the

application.

The work of Schaffner et al. [24], one of the first bacterial bioprinting work published, represents a source of inspiration in this field. The authours used two bacterial strains *Pseudomonas putida* and *Acetobacter xylinum* and an innovative and biocompatible hydrogel composed by hyaluronic acid (HA), k-carrageenan (k-CA), and fumed silica (FS). In their work two different purposes were presented: the former conceived for phenol degradation from the surrounding environment, the latter capable of in-situ formation of bacterial cellulose. The first was printed in the shape of a grid to increase the contact surface with the phenol contaminated surrounding liquid, and after incubation it was shown that degradation was caused not only by bacteria released from the structure, but also by those inside and on the surface. The second was printed in different shapes and once the cellulose had grown it was observed under a scanning electron microscopy (SEM) and characterized from the point of view of oxygen content and the viscosity of the bioink.

With the aim of dynamic drug delivery, Gonzalez et al. [25] created a wound-shaped patch made with a bioink based on agarose and *Bacillus subtilis* spores. This strain was engineered to detect and/or kill *Staphylococcus aureus*, a human pathogen that causes wide range of infectious conditions. At first, the strain expressed GFP in presence of the pathogen for reporting purposes, then it was engineered to produce the antibiotics lysostaphin or thiocillin, which kill *S. aureus* but not *B. subtilis*. A fundamental challenge for living materials is to keep cells viable for long periods and for this purpose bacterial spores represent a convenient tool. Several experiments have been conducted to evaluate the usability of the printed patches over time and despite the extreme conditions the material has proved to be resilient.

In 2024, Datta et al. demonstrated how cyanobacteria can be engineered to produce photosynthetic living materials capable of functional outputs [26]. A synthetic riboswitch was utilized to regulate the expression of a yellow fluorescent protein reporter in *Synechococcus elongatus* PCC 7942 within a hydrogel matrix. The next step was to produce a laccase enzyme to degrade a textile dye pollutant, reducing the need for harsh reagents and lowering energy consumption. Finally, the cells were engineered with an inducible cell death system as a proof of concept of genetic biocontainment.

Various studies have explored the use of ELMs in environmental applications, showcasing the potential of biosensors to address pressing ecological and agricultural challenges.

For instance, Belkin et al. [27] proposed an innovative method combining a fluorescence sensor and a laser-based optoelectronic system to find mines and explosive devices. *E. coli* was designed to sense chemical signals from TNT/DNT for the detection of buried explosives in the soil. The output of

the detected signal was the green fluorescence emission again. The bacterial sensor was immobilized in hydrogel beads and optimized for dispersion over the minefield.

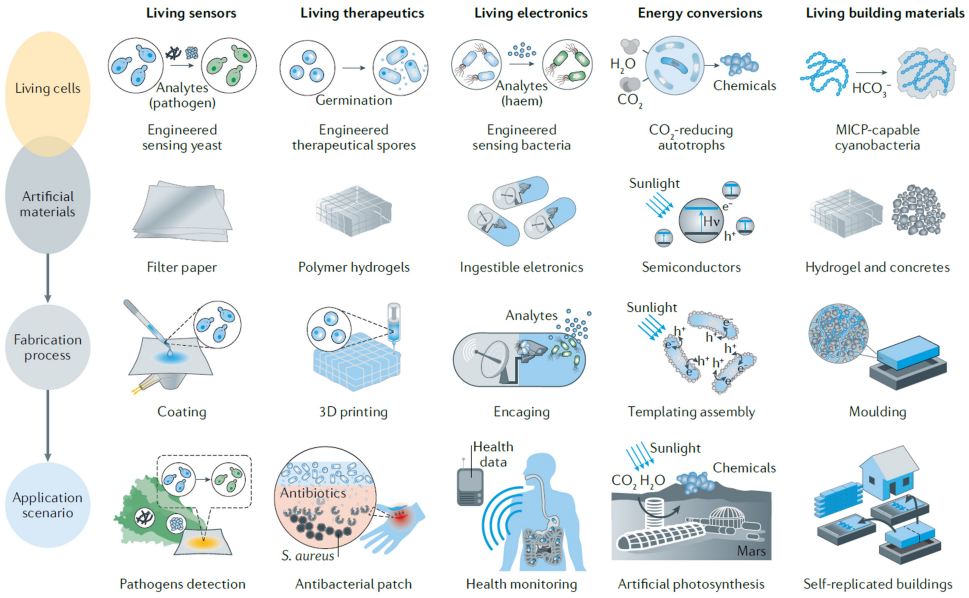

Figure 1.4: Engineered living materials overview. Living cells and materials are mixed to obtain ELMs for a wide range of applications. In the first layer, living cells can be engineered for different purposes, such as sensors, make therapeutics, induce biomineralization. The abiotic compontents, related to their fabrication process, comprise bioprinting techniques, paper-based device and encapsulation, among all. In the last layer different applications are shown. Adapted from [28].

Another example is the study of Ma et al., where the authors focused on the development of a biosensor for detecting volatile organic compounds (VOCs) emitted by infected potato tubers [29]. The sensor employs whole-cell biosensors immobilized in a calcium-alginate matrix (bead and tablet shape), with the primary aim of optimizing membrane uniformity and sensing efficiency. They identified a polymerization time of 20 minutes and an optical density of 0.2 at 600 nm as ideal for bacterial suspension. Additionally, low-viscosity sodium alginate at a concentration of 1.5% (w/v) was found to be the most effective for immobilization, with optimal detection achieved at 4 °C. The sensor was tested for three specific VOCs: nonanal, 3-methyl-1-butanol, and 1-octen-3-ol, achieving detection limits of 0.17 mg/L, 2.03 mg/L, and 2.09 mg/L, respectively, with significant improvements in sensitivity. The biosensor was then integrated into a CMOS platform, enhancing sensitivity by three times and demonstrating the capability of ELMs

in crop health monitoring. While Belkin's research focuses on detecting mines as a proof of concepts of environmental contaminants, Ma's work addresses crop health monitoring, yet both highlight the versatility of ELMs in providing sensitive and effective solutions for real-time detection in environmental contexts.

Lastly, the review article by Tang et al. published in 2021 serves as a comprehensive exploration of how synthetic biology can lead to the creation of smart living materials with applications ranging from environmental monitoring to healthcare innovations [28], focusing not only on bioprinted structures, but also on hybrid materials in which engineered cells can be added to achieve the target function, pointing out either the challenges or the future directions (Fig. 1.4).

Although there have been many advancements, challenges still remain in the field. The long-term stability and safety of ELMs, particularly in therapeutic and environmental applications, are still areas of active investigation. Researchers are working to develop strategies for ensuring that these materials can function reliably over extended periods and in diverse settings without unintended consequences (e.g., using biocontainment to avoid the release of GMOs). Overall, ELMs are poised to revolutionize a wide range of applications, from medicine and environmental remediation to industrial manufacturing, marking a new era in materials science.

1.4 Biocontainment strategies for the safe use of engineered bacteria in field applications

The rapid advancements in synthetic biology have revolutionized various fields, from medicine and agriculture, to environmental science. These innovations bring immense potential for solving complex global challenges, but they also pose significant risks.

As mentioned above, one of the most critical concerns in this field is the potential for unintended consequences if GMOs escape into the environment. Potential hazards include competition with native microbes [30], disruption of ecosystems [31, 32], and the transfer of genetic material, such as antibiotic resistance genes [33], through horizontal gene transfer [34].

To mitigate these risks, biocontainment strategies have emerged as essential tools for ensuring that engineered organisms can be safely managed. This introduction delves into the importance of biocontainment by reviewing state-of-the-art research, emphasizing the necessity for robust containment mechanisms to prevent ecological disruption and ensure public safety.

One of the most promising approaches to biocontainment is the use of programmed cell death (PCD) mechanisms. PCD systems are engineered into GMOs to trigger cell death in response to specific environmental signals, ensuring that these organisms do not persist outside of their intended setting. The review by Molinari et al. [35] highlights the application of PCD in synthetic biology as a fail-safe mechanism that can be programmed into cells. PCD is not only essential for managing the lifecycle of engineered organisms, but also serves as a critical response to environmental triggers, ensuring that these organisms do not survive under uncontrolled conditions.

Furthermore, other reviews [36, 37] point out the advancements in PCD technology, detailing various molecular pathways and genetic circuits that have been engineered to initiate cell death in response to specific environmental cues. The diversity of PCD strategies includes toxin-antitoxin pairs, CRISPR-Cas systems, and synthetic riboswitches, which are triggered by specific stimuli, ensuring that even if an organism were to escape, its survival would be short-lived due to the activation of these self-destructive mechanisms. An example of using synthetic riboswitches it can be found in the work of Datta et al., where authors introduce a PCD approach in cyanobacteria engineered for cell lysis under specific conditions [26]. Their system relies on a riboswitch conformation that changes with the addition of theophylline, leading to the overexpression of the strain, prophage excision, and subsequent cell death. The issue in this type of system is that they are based on exogenous inducers, which are sometimes also toxic to the environment and which in any case do not prevent the release of GMOs until they are added.

Other approaches involve the creation of GMOs with dependencies on synthetic nutrients or unique metabolic pathways that do not exist in nature. For instance, organisms can be engineered to require synthetic molecules for survival, ensuring that they cannot thrive outside of laboratory conditions where these molecules are supplied. In this context, protein engineering plays a pivotal role in the development of biocontainment strategies.

The work of Mandell et al. [38] represents a significant breakthrough in this area, where engineered proteins are designed to require synthetic amino acids that are not naturally found in the environment. This dependence creates a metabolic constraint that prevents GMOs from surviving outside of controlled laboratory conditions. By designing organisms that rely on synthetic amino acids not found in nature, researchers create a metabolic "lock and key" system that ensures these organisms cannot survive without human intervention. This strategy not only limits the potential for escape, but also addresses the risk of horizontal gene transfer, where genetic material could be transferred from GMOs to wild-type organisms.

In addition to genetic and protein engineering methods, physical containment strategies are crucial in managing the risks associated with GMOs. These strategies often involve encapsulating organisms within materials that restrict their movement and interaction with the environment.

Ou et al. explore the use of hydrogel matrices as a partial containment method, where GMOs are embedded within gels that provide a physical barrier, but may not offer complete containment [39]. While effective in limiting movement, these gels might result in some kind of diffusion, highlighting the need for additional safeguards. Moreover, Tang et al. discuss the use of polyacrylamide (PAAm) coating to physically contain GMOs [40]. These matrices provide a robust physical barrier that can restrict the movement of organisms, thereby reducing the likelihood of escape. However, the potential for small-scale leakage remains, indicating that such methods should be combined with genetic safeguards for enhanced security. Guo et al. further investigate the use of adhesin-based matrices, which can limit, but not entirely prevent the escape of GMOs [41]. These matrices are designed to create a physical barrier of 10-100 micrometers, which can contain organisms within a specific area. However, the effectiveness of this method is contingent on the integrity of the matrix, necessitating regular monitoring and maintenance. Liu et al. examine the potential for leakage in systems using polydimethylsiloxane (PDMS) combined with PAAm and agar [42]. These materials are often used to create microenvironments for GMOs, but their containment efficiency can be compromised, particularly over time, as the materials degrade or become porous. This underscores the importance of using these systems in combination with other biocontainment strategies. Volpetti et al. also explore PDMS-based systems with injection ports, which allow for the introduction of nutrients or chemicals into the environment where GMOs are housed [43]. While these systems are effective in maintaining GMOs in liquid media, they are not suitable for the containment of ELMs.

Lastly, Srubar et al. also contribute to this discussion by exploring the broader implications of biocontainment in synthetic biology [44]. Their review provides a comprehensive analysis of the current state of biocontainment technologies, examining the ethical and ecological considerations that accompany the deployment of GMOs. They argue for a "multi-layered" approach to biocontainment, combining physical, chemical, and genetic safeguards to ensure that engineered organisms do not pose a threat to natural ecosystems. This approach underscores the importance of redundancy in biocontainment strategies, recognizing that a single method may not be sufficient to prevent escape and that a combination of methods is necessary to achieve robust containment.

The development and implementation of effective biocontainment strate-

gies will be crucial in ensuring that the risks associated with GMOs are minimized, and these strategies must be rigorously tested and validated before synthetic devices are deployed in real-world applications. The integration of PCD, protein engineering, and physical containment approaches represents the cutting edge of current research and offers a promising path forward. By addressing both the technical and ethical challenges of biocontainment, the scientific community can help protect the environment while unlocking the full potential of synthetic biology.

1.5 Harnessing cyanobacteria for sustainable practices in synthetic biology

The world produces 40 billion tonnes/year in anthropogenic CO_2 emissions [45], which is leading to enduring transformations affecting both human society and biodiversity. In order to mitigate the climate change and meet the sustainable goals, researchers are exploring alternative methods to increase the carbon removal, therefore with CO_2 as an input, rather than an output. In synthetic biology, the carbon footprint can be minimized by exploiting phototrophic microorganisms that harness light and anthropogenic CO_2 to grow, offering a sustainable and cost effective avenue as microbial cell factories.

Cyanobacteria, gram-negative bacteria capable of oxygenic photosynthesis, are promising organisms that could serve as a powerful tool in either carbon neutral (i.e., by balancing the amount of CO_2 emitted with an equivalent amount removed) or carbon negative (i.e., resulting in a net reduction of atmospheric CO_2 levels) technologies. So far only a few species have been explored as synthetic biology targets, including *Synechococcus elongatus* PCC 7942, PCC 7002, and *Synechocystis sp.* PCC 6803. Cyanobacteria have minimal feedstock needs (requiring only sunlight, CO_2, water, and a few nutrients), they are easily genetically modified, and have a rapid growth rate [46].

Beyond their carbon capture capabilities, cyanobacteria offer a more sustainable alternative to traditional heterotrophic counterpart used in bioproduction, as they do not depend on sugar as a feedstock. Current synthetic biology approaches to biomanufacturing are focused on heterotrophic chassis which require a steady source of carbon to grow, with *Saccharomyces cerevisiae* and *E. coli* the most widely used organisms for their quick growth and protein production capabilities. These systems still require feedstocks like sucrose and glucose, which can be carbon-intensive as a feedstock sugar

cultivation means significant amounts of arable land to grow. In addition, unless the final product value is high, feedstocks cost (which constitutes most of the operating costs of a biological process) is not sustainable and could be prohibitive [47]. Therefore, cyanobacteria could represent ideal candidates for sustainable production of bulk products such as food, feed, fuels, reducing the competition with cropland. So far, model cyanobacteria have been used for biosynthesis of multiple products including free fatty acids, isoprene, acetone, butanol, n-alkanes and hydrogen [48].

Two key tools to reduce cost and expand the applications of photosynthetic biomanufacturing are represented by surface display and protein secretion. Surface display technology offers a versatile platform for enabling high-throughput screening of large libraries of proteins with the desired function, accelerating the discovery and optimization process in biomanufacturing [49]. Moreover, it can be used to select for proteins with high secretion efficiency or improve binding properties to a given target, which is valuable in therapeutic protein production and industrial enzyme applications [50, 51]. In addition, displaying enzymes on the surface of cells can increase their stability and activity by immobilizing them in a more favorable orientation or microenvironment [52, 53], and it is useful especially in the production of compounds where multi-step enzymatic reactions are required, or where the enzyme needs to interact with substrates outside the cell. Although literature reports preliminary success in surface display in cyanobacteria [54, 55, 56, 57], ongoing efforts are needed for addressing common issues, such as limited surface accessibility [58]. Regarding protein secretion, the current state-of-the-art solution in cyanobacteria relies on induced cell lysis [26], which is not ideal in large-scale production.

S-layer proteins (SLPs), coupled with the T1SS, could be exploited to develop a platform for surface display and secretion. The Type I secretion system (T1SS), one of the major export systems used by Gram-negative bacteria [59], is not well-characterized in these microorganisms. T1SS is generally based on a continuous tripartite channel, capable of transporting an unfolded substrate in one-step from the cytosol to the external environment. It includes an inner membrane ABC transporter that identifies the secretion signal of the passenger protein, a membrane fusion protein (MFP), and an outer membrane pore protein [60]. Since proteins are secreted directly into the extracellular environment, bypassing the periplasm, T1SS simplifies downstream processing. The absence of cell lysis reduces the need for extensive purification steps, lowering costs and increasing efficiency and yield, which is one reason why T1SS could be exploited for secreting proteins in biomanufacturing [61]. On the other hand, SLPs are composed of a single protein or glycoprotein species of 40-200 kDa [62], and their lattice consti-

tutes a highly porous structure with regularly arranged pores. While SLPs are diverse in their structure and function, some SLPs belong to the Repeat-in-Toxin (RTX) protein family, known to be secreted by the T1SS based on a non cleavable C-terminal signal peptide [63]. The possibility of modifying and changing the natural properties of SLPs by genetic engineering techniques and incorporate specific functional domains while maintaining the self-assembling capability have led to a new era of biotechnology applications, including the development of advanced drug delivery systems, biomaterial scaffolds, and innovative approaches to biosensing and biocatalysis [64]. Therefore, S-layer proteins are able to display foreign peptides and they can be secreted by removing the SLP anchor motif. The work by Molinari et al. on developing a de novo matrix for macroscopic living materials from *Caulobacter crescentus* highlights the potential for engineering SLPs even in other microorganisms, to create customized extracellular matrices that support display, secretion and construction of functional biomaterials all-in-one [65].

Moreover, some cyanobacteria species (e.g., *S. elongatus*) stand out due to their remarkable carbon fixation capabilities and their natural capacity for biomineralization, converting atmospheric CO_2 into organic compounds [66, 67, 68]. These microorganisms can induce the precipitation of calcium carbonate ($CaCO_3$), altering the local pH and creating favorable conditions for mineral deposition. Considering that in 2022 the building and construction sector was significantly responsible for greenhouse gas emissions, accounting for nearly 40% of global energy-related CO_2 emissions [69], cyanobacteria-based solutions could serve as a transition towards more sustainable materials [70]. This dual functionality, that is carbon fixation and bioconcrete precipitation, can provide an eco-friendly alternative to conventional building materials, and a transformative step towards climate change mitigation and sustainability goals.

Different research groups explored the use of living building materials, leveraging the natural capabilities of microorganisms and exploiting sand-hydrogel as structural scaffold. Sea sand is incorporated as a mechanical support component, while hydrogel matrices (e.g., sodium alginate, methylcellulose, gelatine, and trehalose) have been used due to their biocompatibility with cells.

Heveran et al. provide a groundbreaking approach to create and regenerate building materials where both viability and mechanical properties were investigated [71]. Their platform was conceived to alternate liquid stages at 37 °C allowing gene expression and $CaCO_3$ precipitation and stages at 4 °C where the material was solid. Consequently, after each generation, the material proved to be more resistant since the biomineralization increased with

each event. In another work, Reinhardt et al. showed cell viability of *Synechococcus sp.* PCC 7002 within the structure in a time span of 14 days, and biomineralization confirmed by SEM micrographs of the printed constructs after 7 days of cultivation [72].

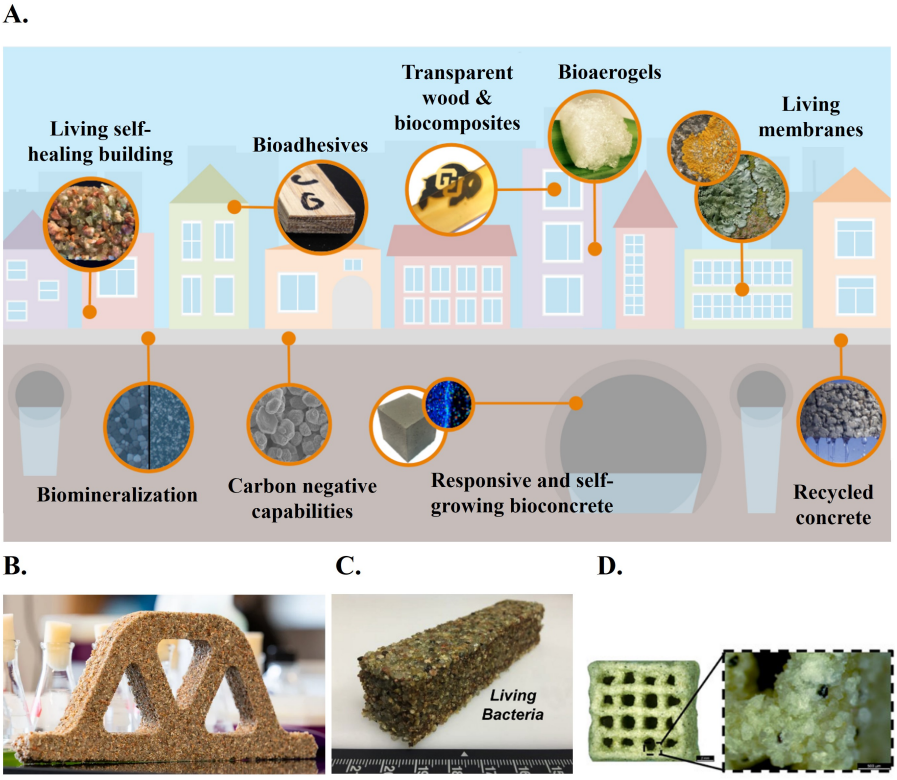

Figure 1.5: Living materials for sustainable buildings. A) Overview of different applications of sustainable living materials for buildings and constructions, with their self-repairing, self-growing, carbon fixation capabilities. Adapted from [73]. B-C) Examples of cyanobacteria based bricks in different shapes, made from the Living Materials laboratory, University of Colorado [71]. D) Bioprinted material based on alginate, methylcellulose, sand and cyanobacteria PCC 7002. On the right, light microscope image of a dry mineralized sample [72].

Surface display of carbonic anhydrase (CA) enzymes on cyanobacteria could be particularly advantageous in the context of biomineralization. CA catalyzes the reversible hydration of carbon dioxide to bicarbonate, a critical step in calcium carbonate formation. By displaying CA on the cyanobacterial surface, the enzyme would be positioned at the cell-environment interface, enabling the interaction with external substrates (e.g., CO and calcium ions) and enhancing the localized biomineralization process. This surface localiza-

tion might help stabilize and promote the formation of calcium carbonate directly at the cell surface, offering a biomimetic advantage that would be less effective with intracellularly expressed or secreted CA alone.

However, the synthetic biology infrastructure in cyanobacteria is still limited as reported technologies showed inferior capacity compared with their counterparts in heterotrophs. Indeed, the growth rates of commonly used cyanobacterial model strains are significantly slower, requiring even months to reach the peak titer that can be performed in *E. coli* or yeast in days [48]. Secondly, many cyanobacteria are polyploid and this means several rounds of segregation for a complete gene knock-out (KO). Therefore, improving genetic engineering techniques in cyanobacteria or exploring new chassis is essential becauase the potential of these microorgamisms can only be fully achieved by adding the synthetic biology approach which can serve to maintain high viability in harsh environments (e.g., dehydration condition), or to enable new functionalities (e.g., improving the biomineralization process).

Overall, with the ability to use novel tools, cyanobacteria could be converted into microbial cell factories as a solution to meet both the increasing demand in the recombinant protein market, and the need to achieve sustainable construction solutions with less of burden on our environment. These advancements open the door to the development of ELMs, where cyanobacteria can play a key role in creating self-healing biomanufacturing platform, rather than eco-friendly building materials that integrate biology with structural design.

1.6 Scope of the work

The great advances in synthetic biology combined with the progress of material science, results today in the realization of smart living materials with unprecedent functionalities, standing as one of the major revolutions in the scientific panorama. As mentioned in Section 1.2, biosensors are devices that allow to sense inputs from the environment and respond with a specific output, and from Section 1.3 we know that living materials can be engineered to make user-friendly devices with biosensing capabilities, overcoming the limitations of microbial cultures in liquid suspensions. Expanding the functional toolkit and application portfolio of bioprinted ELM-based sensing devices is expected to bring significant advantages to various research area, such as environmental monitoring, agriculture, healthcare and materials factory, among others.

This PhD thesis was born as a collaboration between the Bioinformatics, Mathematical Modelling and Synthetic Biology Lab and the Computational

Mechanics and Advanced Materials Group at the University of Pavia with the aim to study the printability of engineered bacterial cells, and their application to practical applications requiring sense-and-respond functions. The first goal was to set up a biofabrication process to create functional living materials acting as synthetic biosensors. To accomplish this, the work required the following key steps: i) selection of materials in terms of bioink, growth medium and bacterial strains based on growth and gene expression tests, ii) design and printing of the structures of interest with diverse geometries, testing reproducibility and tuning different parameters, iii) characterization of the output of our materials, either conceived as sensors with a single bacterial strain or multiple strains.

By doing it, we had to answer several questions, the answers to which are found in Chapter 2 and which is addressed in the publication titled 'Design and biofabrication of bacterial living materials with robust and multiplexed biosensing capabilities' [74]:

- How long do bacteria live in the material?
- Is the living material actually performing the required designed biological function?
- What is the bioprinting fidelity of one or more bacterial strains in the same material?
- How does changing nutrient and incubation conditions affect the biosensor response?
- Does the ELM perform if tested in complex tasks, such as used to sense molecules in clinical samples via user-friendly operations?

Once the workflow was robustly characterized and validated, it was used to create ELMs of interest in the agro-industrial field, which is addressed in Chapter 3.

This second part of the work was carried out within a project in the NODES ecosystem (Digital and Sustainable North-Western Italy), which supports and encourages the transformation of innovative production models to implement green technologies in different industries. The needs arising from two collaborations within NODES were: i) development of biosensors for monitoring acetate levels in biogas plants, as an indicator of process functioning, and ii) nitrate and phosphate monitoring in soil, as an aid to management in agriculture. The first step of the prototyping was searching in literature for inducible promoters in *E. coli* for acetates, nitrates and

phosphates, and once found, characterizing them in liquid, choosing the best candidates and moving on to their ELMs. Subsequently, biosensing tests of the materials with real matrices, i.e., digestate and soil samples, were carried out.

The questions we tried to answer are:

- Once the best biosensors have been chosen in liquid assays, are they compatible with our pipeline proposed above?
- What sensitivity does the biosensor reach detecting the molecules of interest in real digestate and soil samples?

Given the implication of the possible use of these specific ELMs in the environment, the issue of biocontainment was addressed. As mentioned in Section 1.3, one of the major challenges in using ELMs beyond the lab is the risk of engineered bacteria escape into the environment. In this context we sought to implement a biocontainment strategy preventing bacterial escape, and compatible with a method of biosensor readout without having to affect the containment.

As people become more conscious of the need to achieve carbon neutrality and fight climate change, cyanobacteria are attracting more interest in sustainable bioproduction and other biotechnology applications. In this view, this topic has been investigated during a Visiting intership at the Wyss Institute at Harvard University, in the Church lab. As mentioned in Section 1.4, this group of photosynthetic microorganisms are progressively being explored as bioproduction factories, as well as chassis to develop ELMs with both natural CO_2 fixation and biomineralization capabilities. Although engineered cyanobacteria have successfully achieved unnatural functions, there is still an urgent need to identify or develop promising cyanobacteria chassis suitable for biofactory, with rapid growth, strong tolerance, and high biomass accumulation capacity [75], as well as explore new approaches to engineer these microorganisms into efficient biorefineries.

To fill the gap, here, a synthetic biology approach to engineer *Synechococcus elongatus* UTEX 2973, is proposed to convert cyanobacteria in light-driven cell factories for sustainable biomanufacturing and biocement producing ELMs. *S. elongatus* UTEX 2973, a close relative of the model cyanobacterium PCC 7942, represents an ideal chassis candidate, since it has the fastest doubling time among cyanobacteria (about 2 h), in addition to high temperatures and illumination tolerances capabilities. As discussed in Section 1.4, SLPs and their T1SS provide an attractive tool in biotechnology, and prior bioinformatic analysis suggested the existence of these components

in the UTEX 2973 genome. Based on that, the first aim of this project was to develop a sustainable platform for both surface display and protein secretion, serving as a tool to visualize and screen enzymes or peptides libraries, as well as to secrete market relevant proteins (e.g., therapeutics). These tools can therefore be exploited to screen enzymes or secrete proteins for use in the resulting photosynthetic ELMs.

The questions we sought to answer are the following:

- What uncharacterized S-layer protein could suit display and secretion tasks?
- What is the minimal signal peptide of the SLP candidate to successfully secrete target proteins?
- Is the surface of the cell accessible through the SLP for display purposes?

The second goal was to establish a simple workflow to realize cyanobacterial bricks, characterizing both viability and mechanichal properties. As mentioned in section 1.4, cyanobacterial bio-bricks represent an innovative approach with several benefits for our environment, reducing the carbon footprint and serving to mitigate climate change. Moreover, they can represent a novel sustainable building approach, since unlike traditional concrete production, this process does not emit carbon dioxide and it can have carbon fixation, biomineralization and self-reparing capabilities all-in-one. The study and characterization of enzymes to boost biomineralization and proteins to give cells tolerance to dehydrated environments was carried out.

In the same way as in the first ELMs workflow, also in this case the questions asked were:

- Can we develop a protocol to realize living bricks made of cyanobacteria cells?
- What level of compressive pressure can the cyano brick withstand?
- Are carbonic anhydrase enzymes from other species secreted by engineered cyanobacteria also functional? Can we improve the longevity within living bricks in hostile environments by strain engineering?

The answers to all of these last questions can be found in the Chapter 4, dealing with cyanobacteria for carbon negative biomanufacturing.

Overall, this PhD work aims to exploit synthetic biology tools to create useful devices in various fields, from biosensing in agriculture to the production of proteins relevant for the pharmaceutical market, with the possibility

of moving from liquid culture to materials that can be easily used as kits, even directly in the field, with positive impacts on promoting sustainability.

Chapter 2

Design and biofabrication of bacterial living materials for biosensing purposes

This Chapter reports the first results of this PhD thesis, comprising the bacterial bioprinting workflow definition, along with the qualitative and quantitative tests carried out to validate it. We used engineered bacteria capable of molecule sensing and an extrusion-based bioprinting platform to investigate field-relevant unmet needs for biosensing ELM construction: reproducibility and tunability of ELMs, and sensing in harsh environmental or clinical samples. Fabrication of multi-strain materials capable of quantitative readout, multi-input multi-output detection and cell-to-cell communication were also investigated. This study provides key technologies that are adopted in this thesis to construct functional materials with user-defined biosensing capabilities and execute biosensing assays via user-friendly operations.

2.1 Bioprinting workflow

2.1.1 Workflow definition

A commercial extrusion-based bioprinter (CELLINK INKREDIBLE+) was used to define a straightforward workflow realizing bacterial laden structures with predictable shapes. Sodium alginate 8% (w/v) and gelatine 4% (w/v) were used for the hydrogel, exploiting calcium chloride $CaCl_2$ as cross-linking agent. Different parameters and conditions were screened during preliminary tests to optimize the process, also inspired by previous similar

works in literature (see Appendix A). Engineered *E. coli* cells, expressing constitutive RFP in high- or medium-copy plasmid, were used to observe the red color development at naked eye upon growth and protein expression (Fig. 2.1, A). Structures with different shapes and scales were successfully printed, obtaining circular, square, sharp, and hollow features (Fig. 2.1, B), with 10- to 50-mm length and structure height from < 1 mm up to 5.1 mm (17 layers). All of them showed red pigmentation confirming RFP expression, with the strain bearing the expression cassette in high-copy producing a more intense red color than the medium-copy one, as expected.

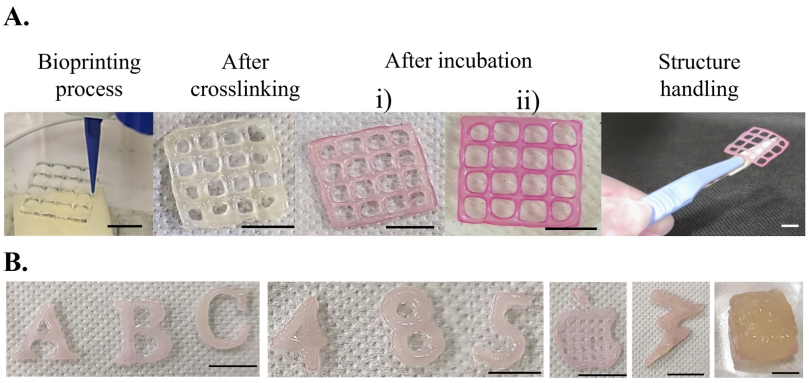

Figure 2.1: Bacteria laden ELMs with different shapes showing RFP expression. A) ELMs pictures during bioink extrusion, just after printing and crosslinking (day 0), after overnight incubation (day 1), and handled after removal from LB agar (day 1). The medium copy (i) and high copy (ii) strains were the living components in this panel. B) Complex structures observed after one overnight incubation. A-B) Scale bar: 1 cm.

2.1.2 Printing fidelity and reproducibility

The shape fidelity and reproducibility of printed structures was quantified by analyzing grids at different heights and distance between filaments. Low variability in filament width and distance was observed, with a CV always lower than 30% among replicated measurements in each analyzed geometry. The average filament width values were about 1.2 mm; they showed a low variation among structures with different heights (CV = 17%) and infill (CV = 12%), with a slight increase of width (1.6 mm) in the 1.8-mm tall structures (Figure 2.2, A-D), as previously reported with other platforms. In our procedure, this increase is most probably due to bioink spreading upon layer addition before crosslinking.

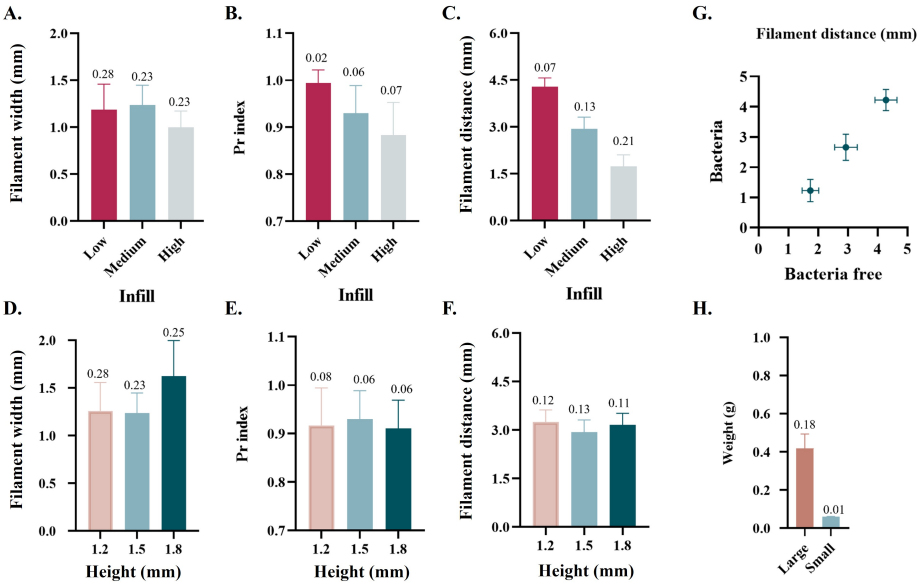

Figure 2.2: Measured printability indexes. Bar charts showing A) filament width, B) Pr index, and C) distance between filaments for grid structures with 1.5-mm height, printed at different infill density (low, medium, high). Bar charts showing D) filament width, E) Pr index, and F) distance between filaments for grid structures printed at medium infill density at different heights (1.2, 1.5, 1.8 mm). G) Scatter plot showing the relation between filament distance measurements in structures with and without bacteria. H) Bar chart showing the weight of 20 x 20 x 2.5 mm grids including the PB5741 strain (Large; N=17) and 10 x 10 x 0.7 mm grids including the MCred strain (Small; N=3). In all panels, bars and data points represent the average values and error bars represent standard deviations. In panels A-G, the coefficient of variation (CV) is reported for each bar (N > 30).

The average distance between filaments varied predictably with the computational design (Figure 2.2, C), accounting for the average filament width measured above, and showed low variation (CV = 5%) for different structure heights (Figure 2.2, F). The average distance values (about 3 mm) were not affected by the slight increase of filament width in the highest structures, described above (1.2 to 1.6 mm), probably because this observed difference (about 0.4 mm) was comparable with the standard deviation of the distance values (0.37 mm). The bioprinting performances were not altered in absence of bacteria in the bioink (Figure 2.2, G), as expected from previous studies with different abiotic and living components. The hollow parts of the fabricated grids had the expected square shape in the lowest-height highestdistance grid (Pr = 0.99). In all the other cases, the Pr value remained around 0.9, demonstrating a reasonable predictability in pore shape (Figure

2.2, B-E). Finally, the weight of structures at day 1, measured on a batch of bioprinted grids, showed an extremely low variability (CV $< 19\%$), indicating that the inter-ELM volume of extruded bioink is highly repeatable (Figure 2.2, H).

2.1.3 Bacterial growth and protein expression in ELMs

The CFU/mg curve increases up to day 2-3, after which cell viability decreases, probably due to the lack of nutrients or accumulation of toxic waste products in solid media (Fig. 2.3, A). Cell growth was then optimized via a subculturing procedure, in which ELMs were moved onto fresh media at specific time points (day 2 and 5) and viability was significantly extended. A drop in cell viability was still observed, probably due to material overcrowding or accumulation of toxic products, but the cell density profile showed a much slower decline than in the no-subculturing condition, reaching a density comparable with the initial one after 2 weeks. This optimization of cell viability is promising especially for biosensing tasks that lean on continuous functioning of the ELM over time.

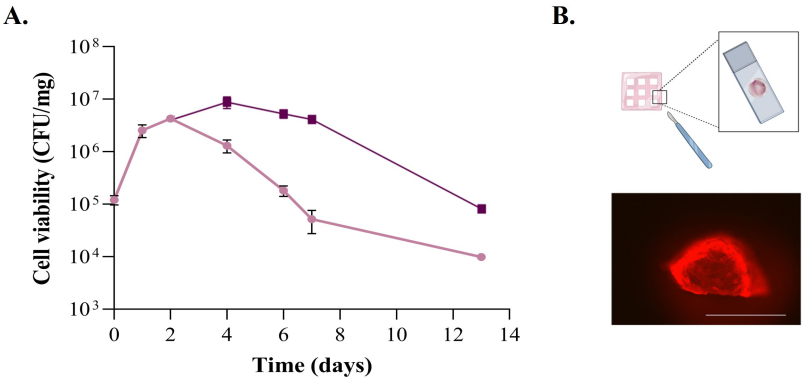

Figure 2.3: ELMs showing cell viability and protein expression. A) Cell viability profile in terms of CFUs per mg of ELM, using a RFP expressing medium copy strain, printed in a set of grid structures (all printed on the same day) which were weighted, entirely dissolved, diluted as appropriate and plated to enable colony count. Solid line represents the mean of three replicates of the same bioprinting batch and error bars represent the standard deviation. The two curves correspond to ELMs that were incubated on the same solid medium for the specified time (pink) or subcultured by moving the structure on fresh medium at day 2 and day 5 (purple). B) Microscopic image of the section of a strand in a 20 x 20 x 1 mm grid structure with MCred strain. The microscopy picture was acquired using the TRITC filter channel, 150 ms exposure. Scale bar: 1 mm.

Moreover, ELMs from the same bioprinting batch showed a low variability in the growth profiles, demonstrating that a high reproducibility persists in cell viability during the bioprinting process. In addition, constitutive RFP-producing bacteria obtained from dissolved ELM formed visibly red colonies, demonstrating a high evolutionary stability over 2 weeks with no detectable mutants for medium copy plasmid.

The spatial distribution of protein expression in ELMs was investigated by analyzing sections of bioprinted structures with fluorescence microscopy. According with the literature [25], fluorescence is more intense at the edge of the structure, although bacteria are homogeneously mixed in the bioink, decreasing at a depth of about 200 μm (Fig. 2.3, B). Since strong fluorescence was observed on top of the construct opposite to the LB agar, RFP heterogeneity is not caused by nutrient limitation preventing growth or gene expression. Oxygen limitation is likely to occur at the center of the structure, reducing bacterial proliferation and RFP maturation.

2.1.4 Printing ELMs with multiple strains

The fabrication of ELMs including multiple bioinks by printing materials with adjacent strains on the same layers was tested. After extrusion, crosslinking was carried out on all the deposited bioinks to generate a unique ELM. We printed two strains constitutively expressing different fluorescent proteins, RFP and GFP (Fig. 2.4). Red and green fluorescence could be conveniently observed with the microscope to assess the absence of cross-contamination between the two compartments and the presence of a net separation between them. We quantified the cross-contamination by detecting green and red fluorescence in the compartments expressing RFP and GFP, respectively, on the ELM surface. Results showed that GFP cross-contamination in the RFP compartment was as low as 0.1%, while no red fluorescence was detected in the GFP compartment. A section of the two-strain ELM also showed net separation between adjacent compartments, demonstrating the reliability of multi-strain ELMs.

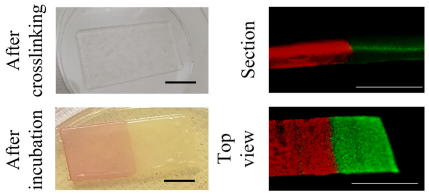

Figure 2.4: ELMs with multiple strains. The ELM (40 x 20 x 1.2 mm) was printed with adjacent strains expressing RFP and GFP, respectively. Scale bar: 1 cm.

2.2 Single-strain biosensing materials

2.2.1 Characterization of a VAI-sensing ELM

The *Vibrio fischerii* autoinducer (VAI) biosensor, with RFP as output, was used as a model system to evaluate the performance of a sensing ELM. First, the dose-response curve of the engineered strain was characterized in liquid assays (Fig. 2.5, A). The bioink was then prototyped with manually extruded materials that were exposed to different concentrations of VAI on agar plates, and produced gradually increasing amounts of RFP, visible as red pigmentation. Comparison between liquid and solid cultures allowed to measure the RFP expression range that corresponds to an RFP pigmentation visible at naked eye and quantifiable via image analysis. The limit of detection (LOD) was between 0.5 and 2 nM of VAI and occurred for per-cell fluorescence values of about 15,000 AU in liquid media. This relation persists for overnight incubated ELMs, while longer periods (> 36 h) correspond to lower LODs due to RFP accumulation. Tunability of the dose-response curve is possible by tuning the expression of the transcriptional activator LuxR, or by replacing the reporter gene with one producing more intense color. Addition of a degradation tag to reporter protein is also possible to increase its turnover and prevent protein accumulation [76]; compared with non-tagged proteins, this intervention would enable the on-to-off transition of biosensors for real-time sensing tasks, but inevitably resulting in a lower per-cell fluorescence and, accordingly, the LOD may increase.

Based on the data above, full induction conditions were applied to the bioprinted sensing patches by using 400 nM of VAI included in LB agar (Fig. 2.5, B). These ELMs were able to produce a visible red color after overnight incubation upon induction at day 0. The continuous monitoring of VAI was then tested: the ELMs were subcultured by moving the structures on fresh LB agar every four days, and induction was tested up to day 8 on previously unexposed ELMs. An intense pigmentation was always observed and unexposed ELMs did not show a significant leakage of RFP, demonstrating that the VAI sensor is fully functional over a long operation time. The red color took about 3 h from induction to develop. This time is probably due to different kinetic steps, such as VAI diffusion through the material and cells, promoter activation, gene expression dynamics (transcription and translation), and RFP maturation, the last being an important rate-limiting step with a time constant of about 1 h.

To test storage conditions relevant to field operations, VAI-sensing ELMs printed at day 0 were stored in a refrigerator at 2-8 °C for 1 month. VAI sensing was still fully functional upon use, after moving the ELM on LB agar

with VAI. In addition to full induction conditions, a dose-response curve was also characterized for VAI-sensing bioprinted patches, by quantifying red pigmentation at different VAI levels (Fig. 2.6, A). Data showed a qualitatively consistent curve compared with manually extruded materials also confirming the LOD value of 0.5 nM, for which ELM output was statistically higher than the no-induction condition ($p < 0.05$, t-test).

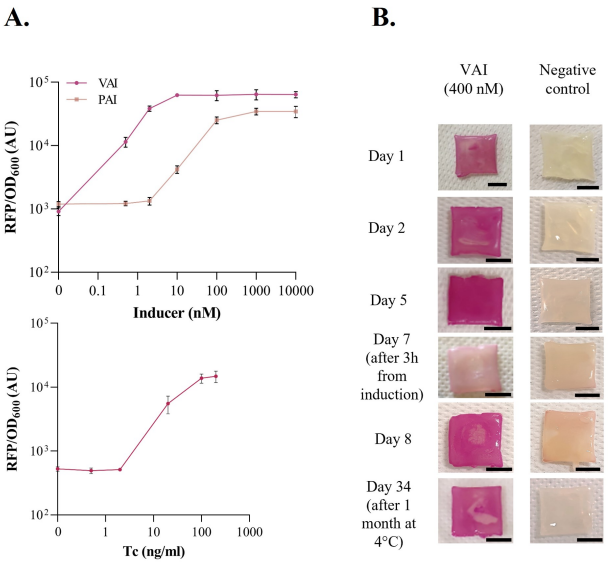

Figure 2.5: Single-strain ELMs for detection of signaling molecules. A) Dose response curves at the steady-state, with per-cell RFP fluorescence as output, of the VAI-sensing strain and the Tc-sensing strain in liquid cultures. Data points represent the average values of three independent measurements and error bars represent the standard deviations. B) Patches of the VAI-sensing ELM after overnight incubation on VAI-containing LB with induction carried out at different days of continuous ELM culturing. Two patches are also shown after 3 h incubation from induction, and upon overnight incubation after conservation in a regular fridge for 1 month. Overnight incubation was carried out at 37 °C and the induction was performed using 400 nM VAI.

The batch-to-batch and day-to-day variabilities of red pigmentation output in patches from independent bacterial batches cultured in the same day and in different days, respectively, were quantified. Experiments showed a similar and modest variability among different bacterial culture batches (CV = 14%) and among different days (CV = 17%), highlighting the reliability of the biosensing devices (Fig. 2.6, A). As expected, the observed red color intensity strongly correlated with red fluorescence ($r = 0.97$, $p < 0.05$),

quantified via plate reader, showing consistent outputs with different detection methods by biosensor users (Fig. 2.6, B).

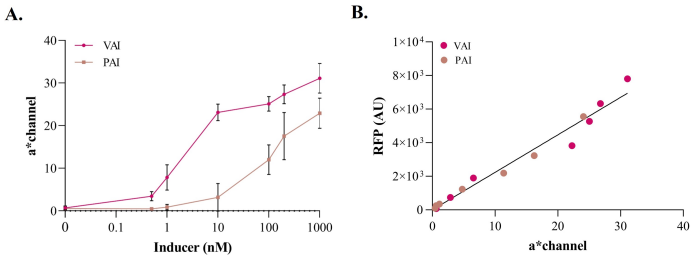

Figure 2.6: Reproducibility of ELM response. A) Dose response curves of bioprinted ELMs induced under VAI and PAI concentrations in LB agar plates. ELMs were stored at 2-8 °C for 1 day before use. Circlesrepresent mean values and error bars represent standard deviations (N = 8). Replicates refer to different bacterial culture batches prepared in 3 different days (2, 3 and 3 different batches, respectively) and used to print ELMs for each VAI concentration tested. B) Relationship between red pigmentation (a* channel values, quantified by image analysis) and red fluorescence (RFP values, quantified by plate reader). Circles represent average values (N = 8) of a* and RFP. The RFP values were obtained by transferring cut pieces of ELMs into 96-well plates and measuring red fluorescence in 3-by-3 square-filled acquisitions per well (RFP gain = 30) and averaging the obtained values. Solid line represents the linear regression fitting of the average values.

2.2.2 Biosensing under non-optimal incubation conditions

The biosensing experiments described above relied on chemical inducers added to solid medium at the desired concentrations by plating. However, practical applications of samples on ELMs may benefit further streamlining, without adopting large amounts of solid media and without the need of plating the samples to be analyzed. To this aim, we carried out biosensing assays in the following conditions:

- in absence of solid media using patches previously grown on LB agar and then removed;
- with a small amount of solid media cut from LB agar;

and in both condition by pipetting a 200 μl drop of inducer on the top of the ELMs, and incubating them at room temperature or at 37 °C. All the four conditions resulted in detectable red pigmentation at the maximum VAI concentration tested of 1000 nM, significantly higher than the non-induced ELMs ($p < 0.05$, t-test), demonstrating that biosensing patches can work

in non-optimal conditions with 2.5- to 40-fold activation range (Fig. 2.7, A). Incubation at room temperature systematically gave less pigmentation than incubation at 37 °C ($p < 0.05$, ANOVA), and incubation of patches on LB agar media gave significantly higher pigment intensity than in absence of solid media ($p < 0.05$, ANOVA). A significant interaction between temperature and media availability also persisted ($p < 0.05$, ANOVA), with the presence of LB medium at 37 °C providing superior color development compared with the other conditions. Although bioprinted ELMs showed responsiveness and highly reproducible output in all the tested conditions, the resulting dose-response curves were different (Fig. 2.7, B). These data were also different from the response of the same sensor tested on LB agar plates, probably due to the different final concentration of VAI between agar plate and applied sample drop. For these reasons, a dramatic variation of biosensing capabilities in terms of LOD value is expected among largely different experimental conditions. For comparison, an output intensity similar to that of agar plate assays at the LOD concentration (i.e., 0.5 nM of VAI) was reached at a VAI concentration of 10 nM for the ELMs in the cut agar condition at both 37 °C and 25 °C. In the 37 °C with no agar condition, a similar value was reached at 1000 nM of VAI, and for ELMs at 25 °C with no agar it was never reached in the tested VAI range (> 2-fold difference).

This feature motivates the need of defining and testing a range of working conditions for ELMs, in which their capability to sensitively discriminate between the target conditions is still acceptable. In qualitative on/off sensing applications, a maximum LOD value should be quantified and molecule concentrations above this threshold can be reliably detected thanks to the high reproducibility of output pigmentation, herein demonstrated. More quantitative detection tasks relying on calibration curves could also be affected by environmental conditions, requiring proper measurements from ELMs incubated in the same condition as in the target assay. To gain further insight into condition-dependent output expression, cell viability was measured for all the conditions above at the end of the experiment. Data showed a strong correlation ($r = 0.98$, $p < 0.05$) between red pigmentation intensity and final cell density in the ELM (Fig. 2.7, C), meaning that the variation in RFP expression can be explained by cell growth, but the regression line has a non-null intercept and for this reason no proportionality persists between the two measured variables.

The feasibility of incubating ELMs at room temperature without specific nutrients will pave the way to biosensing tasks by ELMs in environmental niches, as well as the 37 °C + LB condition will be used as an easy-to-use kit to analyze clinical samples.

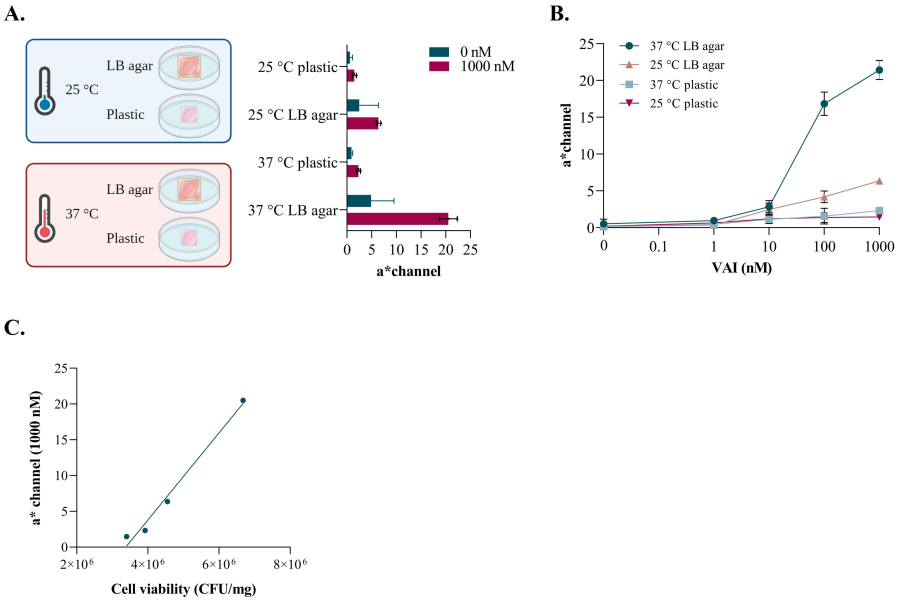

Figure 2.7: VAI-sensing ELM response upon incubation on plastic or cut agar with a 200-μl drop of autoinducer at the indicated concentrations. A) The four experimental conditions are summarized on the left, namely two temperatures (room temperature - about 25 °C, vs. 37 °C) and two nutrient conditions (ELM on plastic Petri dish with no additional nutrients, vs. ELM with a small piece of cut solid medium - LB agar). In the condition without additional nutrients (plastic), ELMs printed at day 0 were incubated overnight on solid medium (LB agar), then moved to a Petri dish at day 1 and incubated overnight in presence of VAI samples; ELM response is then evaluated at day 2. In the condition with cut LB agar, ELMs printed at day 0 were incubated on cut LB agar in presence of VAI samples; ELM response is then evaluated at day 1. Quantification of the red pigmentation, in terms of a* values, are shown in each condition without VAI and with 1,000 nM of VAI. Bars represent mean values with the standard deviations as error bars (N = 3). B) Dose-response curves, in terms of a* values as a function of VAI concentration, of the ELM in the different conditions tested. Data points represent mean values with the relative standard deviations as error bars (N = 3). C) Relationship between cell density in the ELMs (CFU/mg) and intensity of red pigmentation (a* values). Circles represent mean values (N=3) for cell viability and red color intensity. Solid line represents the linear regression fitting of the mean values. Replicates refer to different bacterial culture batches prepared in in the same day and used to print ELMs for each VAI concentration tested.

2.2.3 Biosensing in environmentally relevant samples

VAI-dependent induction was tested by placing ELMs on (or within) VAI-containing soil and immersing them in VAI-containing tap water at room temperature. The sensors showed induction when placed both on the surface and when immersed in soil (Fig. 2C). Although the induced materials showed clearly distinguishable color compared with negative controls without VAI, the color was less intense than the one developing on VAI-containing LB agar, probably due to the lower amount of nutrients in soil than in LB and to the resulting lower concentration of VAI. Induction in tap water was also functional (Fig. 2C). However, red color could not be observed immediately after removing them from the water, and additional 2 h were needed after removal to let the red color develop at room temperature, probably due to RFP maturation which requires oxygen to occur. After that time, the visible color was weak (data not shown) and an intense one could be appreciated only after a further incubation at room temperature.

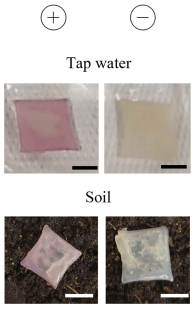

Figure 2.8: Patches of the VAI-sensing ELM after overnight incubation in tap water and soil containing VAI. ELMs were incubated on LB agar overnight after printing, then they were removed from the solid media and applied to the tap water or soil, as indicated. Pictures were taken at day 1 (soil) and 2 (water) upon incubation at room temperature (see text). Tap water contained 400 nM VAI and soil contained 10% of water with 400 nM VAI.

A change of reporter protein could overcome the oxygen requirement and provide a clearly detectable output in a shorter time. These data demonstrate that on/off sensing could effectively occur in field-relevant conditions, in which temperature and nutrients are not optimal for bacterial growth and gene expression. Soil is prone to contaminations by competing microbes due to its composition and immersion in water can result in nutrient washout from ELMs. Also, incubation in a refrigerator for a long time may cause dehydration or crosslinking failure. These challenging conditions were a successful testbed for the fabricated living materials.

2.2.4 Biosensing in clinically relevant samples

The VAI-sensing ELM was used to detect a signaling molecule produced by pathogenic bacteria. In fact, this sensor is also capable of detecting *Pseudomonas aeruginosa* autoinducer, exploiting non-specific activation of the lux-based machinery by this molecule. Based on per cell RFP values in liquid cultures and red pigmentation of ELMs on agar plates, the LOD of PAI increases significantly compared with VAI, resulting in a limit about 10 nM, for which ELM output becomes statistically higher than the no-induction condition ($p < 0.05$, t-test). Here, the VAI-sensor was used to detect PAI in clinical samples, such as isolates derived from patients affected by cystic fibrosis and bronchial aspiration from patients affected by Gram positive or Gram negative bacterial infections.

The sterile-filtered supernatants of 4 clinical isolates of *P. aeruginosa* grown to saturation were collected and applied to biosensing patches, previously stored in a refrigerator for 1 day, with a cut agar section. After incubation at 37 °C, red pigmentation was visible for 2 samples and weakly visible for the others, all statistically higher than the negative control output ($p < 0.05$, t-test), demonstrating the capability of such ELM to detect molecules directly produced by pathogenic bacteria. By using liquid biosensing assays, the output diversity in the samples was confirmed to be due to differences in PAI production levels among the clinical isolate cultures, with concentrations of 1 μM for the isolates giving the highest RFP output, and under the detection limit of the assay for the others.

Another example for a clinically relevant application was tested, using minimally processed bronchial aspirate samples from patients affected by non-*P. aeruginosa* ($N = 12$) and *P. aeruginosa* ($N = 3$) infections (Fig. 2.9, B). Processing included addition of a solution to decrease viscosity, routinely added upon sampling, and a centrifugation step to retrieve the (unfiltered) supernatant fraction. The non-infected samples were also spiked with PAI at 400 nM to confirm the feasibility of PAI detection in complex matrices. Samples were applied to ELMs and incubated as before. None of the non-*P. aeruginosa* bronchial aspirate samples triggered a relevant red pigmentation, demonstrating high biosensor specificity for other Gram negative and Gram positive pathogens. A large part of the spiked non-infected bronchial aspirate samples (10/12) showed red pigmentation, demonstrating successful detection of PAI in highly complex samples in which growth-inhibiting compounds may be present. Finally, one of the three samples with *P. aeruginosa* also gave visible red pigmentation. While no information was available in terms of bacterial density or PAI concentration in bronchial aspirates, it is not surprising that a large variation occurs among clinical samples, in which

a wide range of PAI levels was reported, from picomolar to low micromolar concentrations. The pairwise comparison between values of spiked vs non spiked condition in individual samples is reported in Appendix A (Fig. A.2).

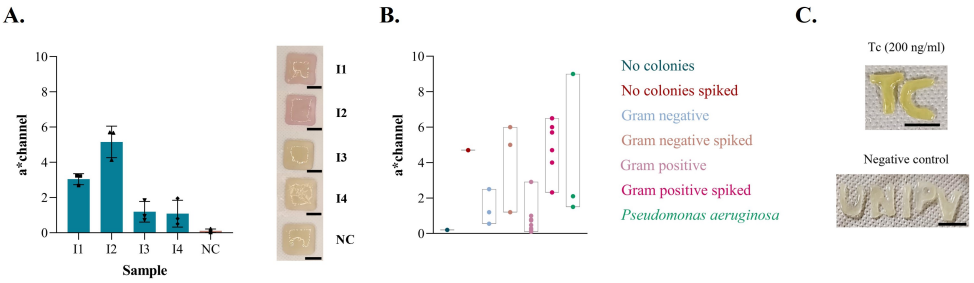

Figure 2.9: ELMs relevant for healthcare. A) ELM response upon PAI sensing from filter-sterilized supernatants of four *P. aeruginosa* clinical isolates (I1-I4). The a* values are reported to quantify the red pigmentation and the corresponding pictures are shown. Negative control (NC) refers to the supernatant of an MG1655-Z1 strain grown at 37 °C, 220 rpm overnight, not producing PAI. ELMs were stored at 2-8 °C for 1 day before use. Bars represent mean values and error bars represent standard deviations (N = 3). Scale bar: 10 mm. B) ELM response upon PAI sensing from 15 bronchial aspirate samples with non-*P. aeruginosa* infection (12 samples, evaluated without PAI or spiked with 400 nM of PAI) and with *P. aeruginosa* infection (3 samples). ELMs were stored at 2–8 °C for less than 15 days before use. The a* values quantifying red pigmentation are reported as individual data points for each infection group (Gram positive, non-*P. aeruginosa* Gram negative, no detectable CFUs, *P. aeruginosa*; N = 1) and the bars indicate their range. C) Proof of concept of ELMs for antibiotics detection. ELMs after overnight incubation at 37 °C on LB containing tetracycline, and then stained with catechol. Pictures were taken after overnight incubation and after 1 min from the addition of catechol. Scale bar: 10 mm.

Other synthetic circuits were proposed in literature to detect PAI with lower LOD values, and the bioprinting techniques used in this study may serve in conjunction with such circuits to facilitate the construction, delivery and approval of sensing devices for clinical use, starting from matrices of different complexity and with minimal sample processing efforts.

Overall, the construction of living devices with functioning compatible with real-life applications was demonstrated: the data on single-sensor ELMs demonstrate that effective sensing materials could be engineered, with attractive features beyond the laboratory setting, including successful functioning over time, in harsh conditions, in complex matrices and detecting a compound relevant for healthcare. Our workflow also enabled the fabrication

of other ELMs with different sense-and-respond functions; for instance, a tetracycline sensor with engineered *E. coli* expressing a strong yellow pigmentation (using the catechol 2,3-dioxygenase xylE gene instead, Fig. 2.9, C), showed genetically-designed improvement of ELM reporting capability at naked eye.

2.3 Multi-strain biosensing materials

We fabricated materials composed of multiple bacterial strains, addressing three key applications of ELMs: quantitative output reporting, multiplexed sensing, and interacting microbial strains driving pattern formation.

Quantitative output reporting is of particular interest to measure compound concentration in field contexts in which the input level saturates the sensor output, or in which a trivial quantification of the produced color can be highly variable and poorly informative to understand the actual concentration sensed. To mitigate this issue, we designed a level-bar ELM composed of four different strains with diverse LODs for the same molecule (VAI). To this aim, we constructed a library of isogenic VAI-sensing strains exhibiting different dose-response curves by placing the LuxR-coding gene under the control of constitutive promoters with graded strengths from the Anderson collection. An initial library of 8 strains was screened in liquid culture assays and in manually extruded constructs on solid media at the specified VAI inducer concentrations to assess their difference in LOD (Fig. 2.10, A). Then, four of these strains, showing significant diversity in LODs, were selected for printing a bar material able to trigger red pigmentation in some of the strains depending on VAI concentration. We also quantified the red pigmentation (a* channel) of the same library manually extruded, which confirmed the dose response trend seen in liquid culture (Fig. 2.10, B). Alternative designs could be also adopted without bioprinting multi-strain materials, with the use of an individual strain at different concentrations of the sample containing the compound to be sensed, or the use of physically separated wells for each strain, also applicable for multiplexed sensing. However, the realized multi-strain solution does not require substrate manipulation, is compatible with rapid prototyping and automated construction, and could be able to provide a discrete quantification of the sensed molecule against a standard curve constructed in the same matrix. When calibration curves cannot be constructed, level-bar ELMs could be adopted as semi-quantitative tools indicating discretized low-to-high output categories to be compared with the output bar of other samples, enabling comparisons but not quantification of the target molecule.

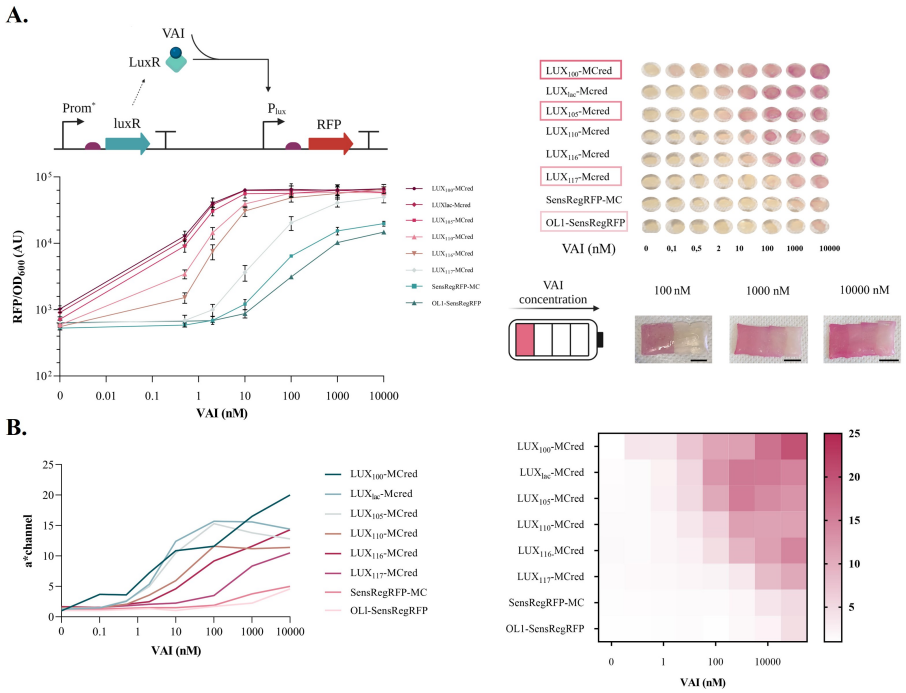

Figure 2.10: Level bar ELM. A) Level-bar detection of VAI. The panel shows the full prototyping process of this multi-strain material: first, a library of VAI-sensing strains was constructed and characterized in liquid cultures. The graph reports the per-cell fluorescence as a function of VAI concentration in liquid culture, with data points representing average values of three independent measurements and error bars representing standard deviations. Second, the same strains were included in manually extruded structures which were incubated overnight on LB agar containing the indicated VAI concentrations. The picture shows the pigmentation as a function of strain and VAI concentration and the four strains selected for the designed material are highlighted. Finally, a level-bar structure was printed, using the four strains selected above. In the scheme of circuit variants shown on top, Prom* are constitutive promoters of diverse strengths, curved arrows are promoters, straight arrows represent genes, half-ovals are RBSs, T-shapes represent transcriptional terminators, light blue diamond is the LuxR protein. B) Quantification of red pigmentation (a* values) on inclusions with the indicated biosensor strains, which differ for the expression level of LuxR and result in diverse switch points and LODs. The same a* values are presented as a heatmap and as dose-response curves, at the indicated VAI concentrations. Data come from a single replicate of the strains tested in parallel on the same day. The response of the sensors was evaluated by manually extruding and crosslinking bacteria-laden inclusions at day 0, applying the inclusions to LB agar containing the indicated VAI concentrations, and incubating the structures overnight at 37 °C; response was evaluated at day 1.

Multiplexed sensing was demonstrated by constructing materials following a shuriken-like structure including strains with independent RFP-producing sensors and information processing circuits. The resulting ELM could successfully sense two inputs (VAI and IPTG) and provide colorimetric outputs resulting from their processing. The four compartments of the ELM act as 1) negative control (non-fluorescent strain), 2) VAI sensor, 3) IPTG sensor, and 4) an AND gate with VAI and IPTG as inputs, respectively (Fig. 2.11, A). This demonstrates that complex patterns could be effectively realized by spatial control of individual strains to engineer materials with multiple outputs.

Finally, we tested ELMs in which multiple strains interact with each other. Even though bioprinting platforms enable the manufacturing of complex patterns in the materials, an additional level of complexity can be enabled by interactions between communicating bacterial strains. To demonstrate this possibility, we printed a material composed of two bioinks, including a sender strain, able to synthesize VAI upon induction with Tc or aTc, and a receier able to sense VAI and express RFP (Fig. 2.11, B).

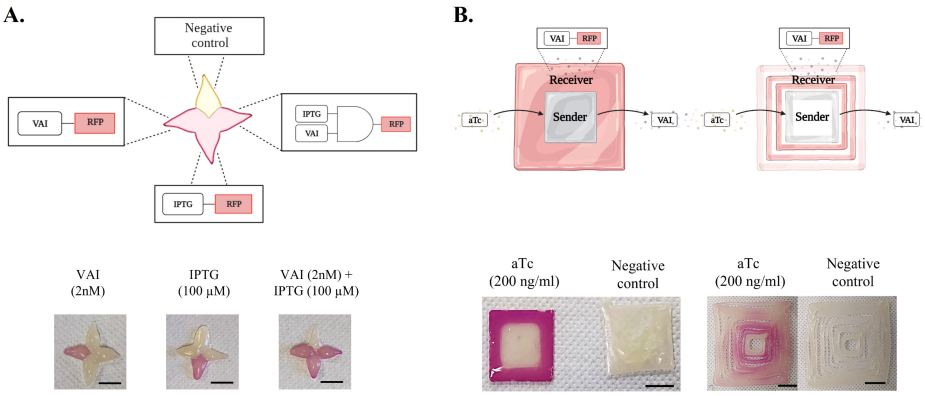

Figure 2.11: Multi-strain ELMs. A) Independent detection and signal processing in a four-strain ELM with a shuriken shape. The four strains are: a VAI biosensor (left point), an IPTG biosensor (bottom point), an AND gate with VAI and IPTG as inputs (right point), and a negative control without fluorescent reporters (top point). The pictures show the ELM at day 1 after overnight incubation on LB agar supplemented with the indicated inducers. B) Patterned gene expression in a two-strain ELM using a sender and a receiver strains. Pictures are shown for two designs in which sender and receiver are printed in adjacent or slightly separated compartments. Patterned and control structures refer to the same designs with 200 ng/ml of aTc or without inducer. In all panels, pictures are shown along with the qualitatively expected output. Scale bar: 10 mm.

Patterns of gene expression were successfully visualized via red pigmentation in the receiver compartment upon aTc induction of the sender strain, in structures in which VAI diffusion occurred between strains in adjacent compartments of the structures or occurred mainly through the solid medium on which the two-strain ELM is placed. The output expression strength could be tuned by changing sender/receiver material geometry, sender induction level and LOD of the receiver strain, thus providing a toolkit for expression pattern formation.

Taken together, these data demonstrate the benefits of rapid prototyping complex multi-strain materials for different applications that were herein used to address key aspects in the biosensing field.

2.4 Final considerations

A bacterial bioprinting workflow was adopted to investigate two key aspects required to streamline the use of engineered living biosensor materials for real world applications: compatibility with field use in different scenarios, and engineering function complexity by materials embedding multiple bacterial strains.

Efficient biosensing of chemicals succeeded in nutrient-poor conditions such as soil or water, relevant for the monitoring of molecules in environmental niches, and in complex matrices such as culture supernatants and bronchial aspirates from patients, relevant for the development of rapid detection kits in clinical samples. Field-relevant features also included the maintenance of cell viability and synthetic circuit stability over two weeks of continuous functioning and the possibility to store the bioprinted materials in refrigerated conditions for more than a month before use. However, dose-response curves of sensors were affected by the environmental context used in detection assays, influencing their sensitivity, and highlighting the need of characterizing their response in conditions similar to the target ones to estimate the application-specific detection limit.

Even though the bioprinting procedure herein used is different from previous reports on bacteria-laden materials, in terms of abiotic component composition, living component content, and printing-crosslinking process, we obtained comparable performances for long-term viability, storage and sensing in water samples, and successfully tested a procedure to prolong cell viability. Our data also showed a remarkable performance of biosensing materials in complex environments such as soil and clinical samples, suggesting that living materials may surpass other technologies such as cell-free approaches, in terms of sensing in complex matrices with no need of sample processing, as we

demonstrated with the detection of the *P. aeruginosa* autoinducer in spiked and real clinical samples. Biocontainment, not addressed in this work and already demonstrated in previous works on engineered living materials, will provide deployable devices for field applications with no genetically modified microorganisms escape.

Then, a number of benefits have been demonstrated by fabricating living materials with more than one bacterial strain, prototyping devices that support the (semi-)quantitative detection of a molecule, the multiplexed detection of different molecules or their combination, and cell-cell communication-mediated patterning of materials. The complexity of such functions, enabled by the precise spatial control of strain printing and by synthetic biology tools to engineer new functions, will boost the potential of biosensing and signal processing capabilities in such devices. Synthetic biology interventions have also been demonstrated to properly tune the response of one of the sensors that provided a too low output range and needed an amplification of the visible readout.

Overall, this part of the work has demonstrated that bacterial bioprinting can be used to fabricate multi-input/multi-output and highly reproducible biosensing devices in terms of shape, performance, longevity, and stability. Such procedure, boosted by the fabrication of material with multiple strains, is amenable to further automation to streamline the whole design and prototyping process of bacteria-laden engineered biosensing materials.

Chapter 3

Biosensing ELMs for environmental monitoring and agro-industrial applications

This chapter describes the construction of 11 biosensors useful for environmental monitoring and agri-industrial processes, along with their characterization and the fine-tuning of the best candidates for each target molecule. In detail, volatile organic compounds (VOCs), acetate, nitrates and phosphates represent out target signals that we aim to sense from different real scenarios. This part of the work involved several collaborations, which were essential not only for obtaining real samples to test the biosensors but also for understanding the significance of each biosensor and providing guidance on choosing parameters for setting up the experiments. These collaborations include professor Anca Macovei from the Department of Biology and Biotechnology "Lazzaro Spallanzani" (University of Pavia), professor Andrea Fiorini, Federico Capra from the Department of Sustainable Plant Production Sciences, professor Alessandra Fontana, Paolo Bellassi from the Department for Sustainable Food Process, and professor Antonio Gallo from the Department of Animal Science, Food and Nutrition (Catholic University of the Sacred Heart, Piacenza). Following the cloning process, the biosensors were tested through liquid assays and the best candidates were better investigated depending on the tasks to be optimized for each of them. The biosensors were then printed using the pipeline as in Chapter 2 and tested in laboratory conditions with standard and real samples. Finally, a physical biocontainment strategy is proposed for the use of the biosensors in the field, among with a straighforward method to detect the sensor response inside the container using a smartphone and a green pointer laser.

3.1 Biosensors construction and functional characterization

To date, synthetic biology in the field of biosensing can boast a wide range of promoters and reporting elements, but it is still necessary to identify and integrate the appropriate sensor for a given application, especially outside the laboratory, in which real-world application require sensing activities in diverse matrices. Here, we characterized 11 biosensors, starting from native promoters in *E. coli* already seen in the literature, to develop a set of devices useful for specific agro-industrial and environmental applications (Fig. 3.1).

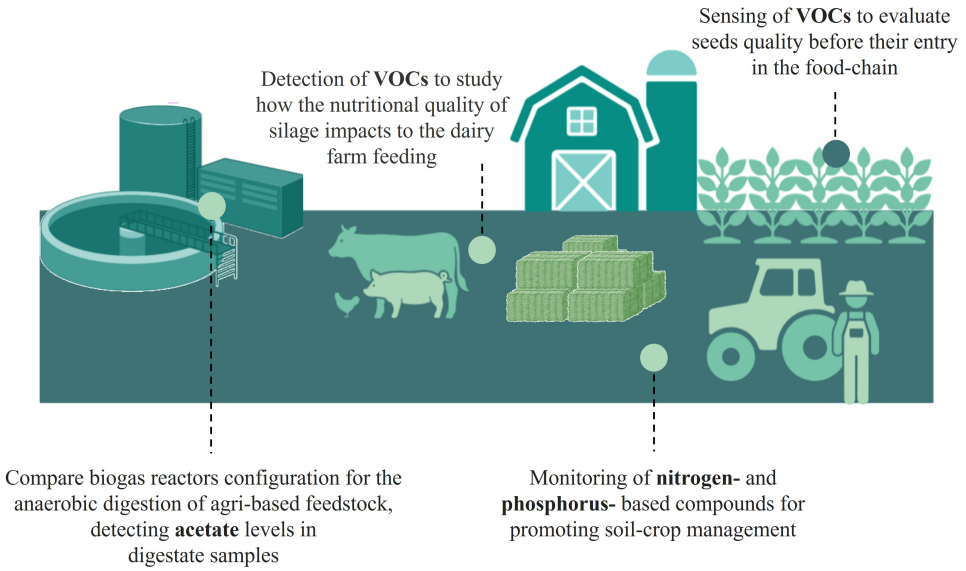

Figure 3.1: Overview of our biosensors for agro-industrial and environmental applications. Synthetic biology, through the use of biosensors, offers innovative solutions promoting sustainable agri-industrial systems. It enables the detection of VOCs to assess the nutritional quality of silage in dairy farm feeding, monitors seed quality before entering the food chain, and enhances biogas production tracking acetate levels in digestate. Additionally, biosensors facilitate the monitoring of nitrogen and phosphorus-based compounds to improve soil-crop management practices.

The promoters required for the eleven biosensors (Table 3.1) were individually cloned into a medium-copy plasmid, using RFP as a reporter gene and TOP10 or MG1655 cells as the *E. coli* chassis strain, except for specific sensors that required genomic deletions to avoid transcription interference. The dynamics of each sensor were investigated by exposing cells harboring the various plasmids to different concentrations of inducers under aerobic

or low-oxygen conditions (Appendix A). The OD_{600} were recorded for 24 h of growth to exclude any toxicity of the molecules, which having been chosen according to concentration ranges seen in other works, and therefore have proven to be non-toxic. The RFP (AU), or the RFP normalized to the OD_{600} to account for differences in growth parameters, and fold change (FC) were used to parameterize the performance of each sensor and to compare them. Then the selected biosensors were further investigated to develop their respective ELMs. For each target molecule, a brief introduction of the task aim comes first than the results of the response function in liquid assay.

Promoter	**Regulation**	**Sensor input**	**Previous work**
prprA	Activator	etOH, metOH, acetone	[77]
pcpxP	Activator	etOH, metOH, acetone	[77]
pompC	Activator	etOH, metOH, acetone	[77]
pfrmR	Activator	Acetaldehyde	[78]
pglnaP2	Activator	Acetic acid	[79]
pglnaP2 (truncated version)	Activator	Acetic acid	[80]
pcfaP	Activator	Acetic acid	[81]
pyeaR	Activator	Nitrate	[82]
pnorV	Activator	Nitrate	[83]
pphoA	Repressor	Phosphate	[84]
pphoB	Repressor	Phosphate	[84]

Table 3.1: Biosensors selected for agri-industrial and environmental applications. From left: promoter's name, type of regulation, the molecule detected in this work and the previous work seen in literature.

3.1.1 Characterization in liquid culture

VOCs

In agriculture, unexpected losses in seed viability negatively impact seed sales and production schedules, costing the industry millions of dollars each year. Since all seeds deteriorate over time, the main goal of the seed industries is to optimize crop production and seed storage by understanding when and how deterioration takes place [85]. Although the asymptomatic phase of seed deterioration is difficult to observe as it is not characterized by evident physical changes in the seeds, some chemical reactions occur and lead to a slow loss of seed vigor. A link between seed deterioration and the release of VOCs was documented for the first time in 1989, when a significant correlation between seed germination/vigor and the relative abundance of volatile

aldehydes released by soybean seeds heated to 130 °C for 2 h was observed [86]. VOCs are a large group of carbon-based chemicals that easily evaporate at room temperature. The production and release of VOCs depend on the chemical reactions that occur and are influenced by different factors, e.g. seed chemical composition, storage conditions in terms of temperature and moisture content [87]. Zhang et al. detected a total of 24 volatile compounds released from dry seeds of 47 species during storage at 23 °C, demonstrating that VOCs production and release occur from dry seeds in different storage conditions. VOCs detection might represent an important aid to predict the quality of the seed, with positive impacts on the seed market before their entry into the food-chain.

The detection of VOCs plays also a crucial role in assessing the nutritional quality of silage in dairy farm feeding. Silages are considered as an important source of nutrients and carbohydrates for the animals, and when feeding animals with silage of any kind, the most critical point having effect on the production of animals is the quality of silage [88]. Silage quality is largely determined by the fermentation process, which is essential for preserving the forage [89]. VOCs, such as organic acids, alcohols, aldehydes, and esters, are byproducts of this fermentation. By analyzing VOCs, the efficiency and success of the fermentation process can be estimated and since silage is a key component of dairy cow diets, its nutritional quality influences animal performance. VOCs may serve as early indicators of whether the silage has the right balance of nutrients, leading to a better feed efficiency, perhaps healthier cows.

Here, we took inspiration from the work of [77] where the authors quantified the patterns of activity produced by the two-component systems EnvZ, OmpR, CpxAR, and RcsCDB when cells are stimulated with different VOCs and stimuli. In this work the ompC, cpxP, and rprA promoters have been used as sensors for ethanol, methanol and acetone since they are our target VOCs. Considering that there are many types of VOCs, which belong to different chemical groups (e.g., alcohols, aldehydes, and hydrocarbons), we tried to understand whether using three sensors in a combined manner could be a strategy since we do not know a priori which VOC profile is emitted by seeds or silage samples. In addition, we searched for a sensor that could work for acetaldehyde and then characterized the sensor based on the frmR promoter.

Given the volatility of the molecules, we studied these biosensors in low-oxygen condition in closed vials to avoid any evaporation, investigating both the exponential phase 3 hours after growth and at 24 and 30 hours (the stationary data are reported at 24 hours as they are not different from those at 30 hours). For ethanol, methanol, acetone and acetaldehyde, a range of

concentrations was used taking inspiration from the literature, staying below the toxicity threshold as reported in the papers for each molecule [90, 91, 78].

Starting from exponential phase, what emerges is that the M9 medium leads to a higher leakiness than the LB for all three sensors (Fig. 3.2, A vs B). The media composition is, indeed, one of the most impacting factor for some sensors output. This phenomenon has been previously observed, where certain chemicals only induce these two-component systems under specific growth conditions, such as low temperature or a specific carbon source for growth [92].

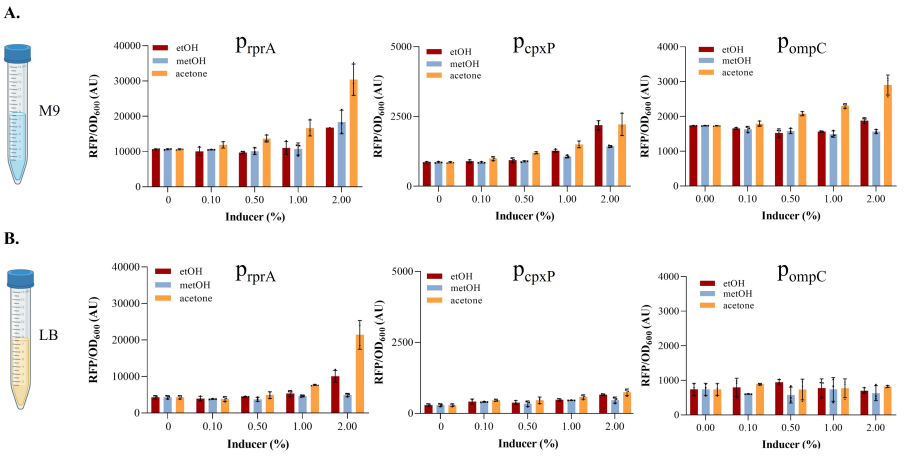

Figure 3.2: Dose and response of VOCs sensors in exponential phase. Gene expression data of the three sensors upon induction in exponential phase, in M9 medium (A) or in LB (B). Ethanol, methanol, and aceton were used as inducers at the concentration of 0, 0.1, 0.5, 1 and 2 %. Bars are the average of a biological triplicate, error bars the standard deviation and the black points represent each value.

All sensors, except ompC, showed a dose-dependent response when exposed to their cognate inducer, though with a relatively low dynamic range. In particular, rprA reported a FC > 2 in LB medium for both ethanol and acetone at the highest concentration tested (Fig. 3.2, B prprA), while in M9 only for acetone 2% (Fig. 3.2, A prprA). Similarly, cpxP achieved a FC > 2 for ethanol and acetone at the highest concentrations in both culture media (Fig. 3.2, A-B pcpxP). However, for the ompC-based sensor data are not promising (Fig. 3.2, A-B pompC), and we expected this result because in the work of Clark et al. this promoter was more sensitive to other molecules such as indole, pentanol and butanol to name the first three with FC > 3 [77].

What emerges from the comparison between the output after 3 and 24 h is that all of them became more active upon entry into stationary phase, and this has been observed also in [77]. Both rprA and cpxP reported a dose-dependent response: in M9 the promoter rprA reached better results for ethanol and methanol, while LB resulted the best condition for acetone which led to cells death in M9, probably due to a combination of the high concentration, therefore toxic after 24h, and the growing medium not as rich as LB (Fig. 3.3, A-B prprA). In detail, in M9 a FC of 2 was obtained for the highest concentration of ethanol, and a FC > 3 for methanol 2%. In LB only the highest concentration of acetone reached a FC > 2. For the promoter cpxP, LB medium proved to be the best condition for methanol, while M9 the best for ethanol and aceton (Fig. 3.3, A-B pcpxP). In particular, in M9 it resulted in a FC > 2 for both ethanol and methanol 2%, and aceton 1%, while reaching a FC > 3 for acetone 3%. In LB a FC > 3 was recorded for the highest concentration of methanol and acetone.

Regarding the ompC-based sensor, also in this case it did not work in either medium tested (Fig. 3.3, A-B pompC).

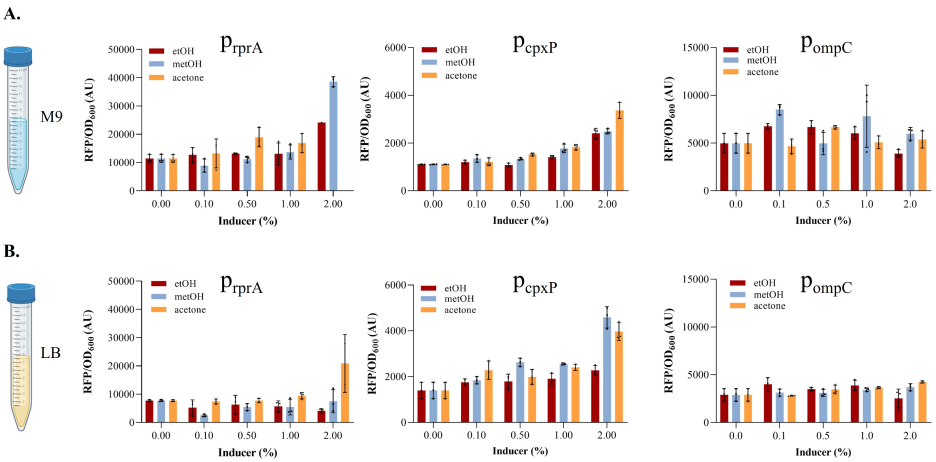

Figure 3.3: Dose and response curve of VOCs sensors in stationary phase. Gene expression data of the three sensors collected in exponential phase, in M9 medium (A) or in LB (B). Ethanol, methanol, and aceton were used as inducers at the concentration of 0, 0.1, 0.5, 1 and 2 %. Bars are the average of a biological triplicate, error bars the standard deviation and the black points represent each value.

Acetaldehyde ($CH_3HC{=}O$), differs from formaldehyde only by replacement of a carbonyl-bonded proton with a methyl group. This made us think to investigate in a well-known sensor for formaldehyde based on frmRAB

promoter and its aspecific response. Neither the exponential nor the stationary phase (Fig. 3.4), using M9 or LB as a culture medium, showed relevant output changes upon induction. This led to the conclusion that the sensor does not work in the presence of acetaldehyde at the concentrations tested.

From previous studies [78] we know that the FrmR system in *E. coli* is not specific, but formaldehyde is by far the most effective inducer. Authors reported an enzymatic activity in response to acetaldehyde lower by about 3 fold compared to that obtained with formaldehyde. This contrasts with the FrmR system in *Salmonella typhimurium*, which do not respond to acetaldehyde or organic alcohols (in the same type of experiment mentioned for [78]), suggesting sequence differences between the two proteins around the sensory site could affect selectivity [93].

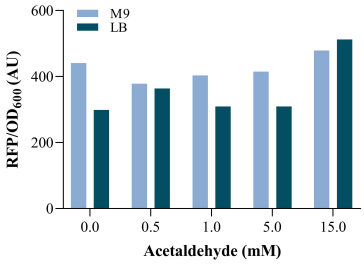

Figure 3.4: Dose and response curve of a formaldehyde sensor using acetaldehyde as inducer, ranging from 0 to 15 mM. Data refer to the stationary phase, and are collected using M9 or LB as culture medium. Bars are the value of one replicate.

Overall, rprA-based sensor it has proven to be the strongest promoter, reaching levels of RFP visible to the naked eye, comparable with the constitutive RFP strain in medium copy that we tipically use as positive control in the bioprinting experiments. The cpxP promoter obtained the best dose and response behavior, especially in stationary phase. The two inducible promoters could represent a promising tool for detecting high levels of VOCs, as they might be present in insilate samples, even though tests on real samples still need to be carried out. On the other hand, their induction characteristics make them unsuitable for highly sensitive detection of VOCs, as it is required in quality control of vegetable seeds, and different sensors need to be prototyped for this applications.

Even if two of these sensors could give hope for improvements with gene circuit amplification techniques, we have not reported in this thesis further experiments in liquid and for the ELM versions because the concentrations of the VOCs profiles emitted from vegetal seeds are below our detection range, and therefore we are currently working on the search for new promoters for

VOCs.

Acetates

With increasing industrialization and population growth, the production of waste materials has become a significant concern for researchers, while the utilization and valorization of agricultural wastes for energy production and bioeconomy is increasingly gaining significant traction [94]. The circular economy framework emphasizes resource efficiency and waste minimization by promoting the reuse, recycling, and recovery of materials. Wastewater and organic fractions of solid waste may represent feedstocks for biorefinery processes, converting waste into valuable products such as bioenergy, biofuels, and fertilizers, contributing to sustainability and reducing environmental impact. Agri-based feedstocks and byproducts from agro-industrial activities, such as crop residues and animal waste, can be integrated into biorefineries to produce these value-added bioproducts, generating renewable resources from otherwise discarded biomass.

In this context, biogas plants play a crucial role in producing renewable energy sources, such as methane, through the anaerobic digestion of organic waste materials like agricultural residues, food waste, and manure, by specific microbial consortia. Additionally, the byproducts of biogas production (e.g., digestate) can be used as nutrient-rich fertilizers, supporting the circular economy practices. Specifically, anaerobic digestion occurs in four successive stages: hydrolysis, acidogenesis, acetogenesis, and methanogenesis. Single-stage and two-stage processes are different approaches that are designed with all the phases occuring in the same reactor by a unique microbial consortium (single-stage), or with different phases occurring in different reactors under distinct conditions and microbial consortia (two-stage). In the digestion process, complex organic materials are broken down into simpler compounds, with acetic acid being one of the key intermediates formed during acetogenesis. The presence and concentration of acetic acid are important indicators of process efficiency. Optimal levels of acetic acid guarantee a stable and effective conversion to methane. However, elevated acetic acid concentrations can indicate an imbalance in the system, often due to bottlenecks before methanogenesis, e.g., caused by improper pH conditions or sub-optimal characteristics of the input waste [95], which can inhibit methanogenesis and reduce methane yield. Therefore, monitoring acetic acid levels helps maintain balance in the reactors, ensuring efficient biogas production.

In our investigation of native acetate promoters in *E. coli*, our primary goal was to characterize three sensors in order to develop an ELM capable of detecting acetic acid in digestate samples.

Two of the sensors selected for acetate detection are based on the glnaP2

promoter, which is primarily involved in nitrogen regulation. This promoter is controlled by the Ntr system, functioning through the NtrC/NtrB two-component regulatory system and the σ^{54} transcriptional factor. In its natural setting, the glnaP2 promoter facilitates efficient nitrogen utilization by expressing genes essential for growth under nitrogen-starvation conditions. One of the key regulators in this nitrogen pathway is the NRII sensor kinase, encoded by the glnL gene. NRII can suppress glnaP2 activation, preventing its induction under nonspecific conditions [96]. Consequently, deleting NRII disrupts the regulation of glnaP2, making it responsive to acetyl phosphate, a precursor of acetate [97, 98].

One of the genes strongly induced by acidic and osmotic stress is cfa, which is well-known for encoding the cyclopropane fatty acid synthase (CFAS) enzyme in *E. coli*. CFAS plays an important role in bacterial membrane modification by catalyzing the conversion of unsaturated fatty acids into cyclopropane fatty acids (CFAs). Although cfa is not directly involved in acetate metabolism, it has an indirect link through its influence on membrane composition and stress responses [99, 100, 101]. The synthesis of CFAs, which is upregulated during stationary phase and stress conditions, contributes to the *E. coli* ability to withstand acidic stress. Two promoters regulate cfa transcription: P1, transcribed by σ^{70} during exponential growth in response to low pH, and P2, active in stationary phase under the control of σ^{38} [102].

Taking inspiration by the work of Farmer et al. [79], we utilized glnaP2 as an acetate-inducible promoter in a modified strain of *E. coli* (JW3840, $\triangle$glnL), which makes glnaP2 dependent on extracellular acetate. We characterized this promoter in two different forms: one version extending to a few base pairs downstream of the transcription start site (TSS), and another version truncated at the +1 TSS (referred to as glnAP2 truncated). The truncation was inspired by the work of Moser et al., who demonstrated that it led to reduced promoter leakiness and an increased fold activation in the presence of acetate [80].

The third sensor we tested was based on the cfa promoters P1 and P2, which were cloned together, following the approach taken by [81]. However, in their study, the promoters were examined individually rather than in tandem.

We started by screening the three promoters in liquid assays to identify the most suitable candidate for our sensor. We used the M9 medium (supplemented with casamino acids and with glycerol as the main carbon source) for the experiments, focusing on the stationary phase, while inducing the sensors with different concentrations of acetic acid, ranging from 0 to 30 mM, since they are reported in literature to be no toxic in *E. coli*. The data reported reflected the RFP levels, normalized by cell density, in the absence of acetate and at the highest concentration tested (Fig. 3.5).

The results from the cfaP promoter showed a high normalized RFP level even in the absence of acetate, likely due to effects during the stationary phase occurring for this promoter. Therefore, we decided not to continue investigating this sensor.

By contrast, the response from the full glnaP2 promoter demonstrated significant sensitivity to acetate, with a FC greater than 80. This result is in accordance with data of the induction/noninduction ratio reported previously in another work [79], even if the experimental set up was different. These results led us to select glnaP2 as the best candidate for our acetate sensor. However, for the truncated version of glnaP2, we were unable to replicate the findings reported by Moser et al. [80], which may be attributed to differences in experimental conditions, such as the use of nitrogen-rich media that may have interfered with the glnL knockout effect on nitrogen starvation responses.

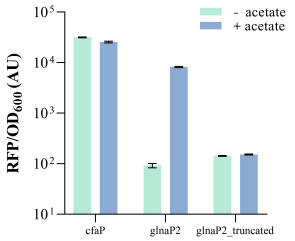

Figure 3.5: Screening for the acetate sensor. Three promoters, i.e., cfaP, glnaP2 and its truncated version, were screened and tested with and without acetate, to choose the one with the best performance. Bars refer to the mean of a biological triplicate, error bars are the standard deviation. Data are collected in stationary phase (24 h).

We then dove into the characterization of glnaP2 by changing medium, pH and testing it in liquid with spiked digestate samples coming from laboratory-scale reactors after anaerobic digestion experiments.

A comparison between M9 and LB demonstrated that this sensor performs better in M9 (Fig. 3.6, A). Recent studies have shown that during *E. coli* growth on glucose, acetate metabolism involves both production and consumption of acetate, with its uptake or secretion depending on the net flux through the Pta-AckA pathway [103]. At higher external acetate concentrations, the net flux was observed to change direction, allowing acetate to flow into the cells. This indicates that excess acetate enters central metabolism and may limit fluxes essential for maximal growth. In light of this, we hypothesized that acetate at 25-30 mM in a nutrient-rich medium like LB could

be toxic due to metabolic imbalances, potentially affecting pathways involved in glnaP induction.

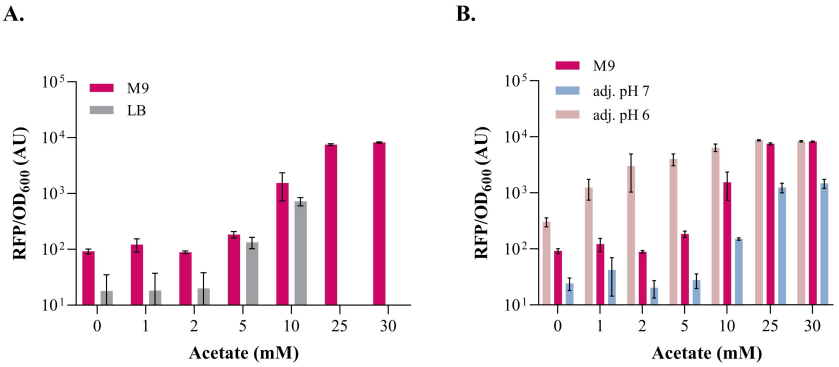

Figure 3.6: Characterization of glnaP2 promoter tuning important parameters. A) Dose response curve of the glnaP2-based sensors upon acetic acid induction, comparing M9 minimal medium and rich LB medium. B) Dose response curve of the glnaP2-based sensors upon acetic acid induction in M9, comparing conditions in which pH was stabilized at 6, 7 or not adjusted. A-B) Bars refer to the mean of biological triplicate and error bars are the standard deviation. Data are collected in the stationary phase in low oxygen conditions.

Regarding pH regulation, we thought it was an important factor to take into consideration, since the inducer of this sensor is intracellular acetate but *E. coli* cell permeability to acetic acid is much higher than the permeability to acetate. For this reason, consistent with the study by Bulter et al., we expected a pH-dependent ratio of extracellular acetate/acetic acid, changing the dose response curve of the sensor because of the different permeability. Without drastically changing the pH, we tried adjusting it to 6 and 7, comparing it to the experiment done in M9 where the pH was not controlled, and therefore the pH of each induction depended on the concentration of acetate added.

The data reported for all the three conditions exhibited a functional a dose response trend of the glnaP2 promoter, but with differences in terms of dynamic, operating range and normalized RFP level reached (Fig. 3.6, B). What we observed is that the pH 7 condition has the lowest basal activity, a dynamic range with a FC of about 61 at the highest concentration tested, but can produce a detectable output from 10 mM. The condition without stabilizing pH reached as mentioned above a FC of 81 at 30 mM of acetate, but again detecting acetate from the concentration of 10 mM. Interestingly, the condition with the lowest pH resulted in a lower FC at the highest concentration (about 27), but a much higher sensitivity, since fluorescence above

the basal level was produced from 1 mM of acetate. However, at pH 6 a much higher leakage activity compared with the previous conditions was observed.

Noteworthy, acetic acid behavior changes significantly based on pH, which directly affects its membrane permeability in bacterial cells [104, 105]. At low pH, acetic acid exists in its undissociated form (CH_3COOH) because the surrounding environment is acidic. In this form, acetic acid is more lipophilic, allowing it to diffuse easily across bacterial membranes. Once inside the cell, where the pH is typically more neutral, the acetic acid dissociates, releasing protons and lowering the intracellular pH. This acidification affects cellular processes, making *E. coli* more vulnerable due to the bacterial stress. In more alkaline conditions, acetic acid dissociates into its ionic form, acetate (CH_3COO^-), and H^+ ions. The acetate ion is hydrophilic and carries a negative charge, making it unable to pass freely through the lipid bilayer of the bacterial membrane. As a result, at high pH, acetic acid (as acetate) has reduced membrane permeability, limiting its ability to enter the bacterial cell and exert its acidifying effect. This reduces the inhibitory or toxic impact of acetic acid on bacteria in alkaline environments.

Therefore, being more permeable at low pH might explain why the sensor's sensitivity at pH 6 is better than pH 7, while the condition without stabilizing the pH reached almost the same results of pH 6 only for high concentration of acetic acid (precisely when the pH results lower).

Nitrogen- and phosphorus- based compounds

Soil monitoring is emerging as a key factor to manage smart farming which has been recommended to have economical food safety and security [106]. In detail, monitoring nitrogen- and phosphorus- based compound levels is essential for sustainable agriculture and environmental health. Studying their levels in soil helps optimizing fertilizer use, preventing and reducing agricultural runoff into nearby ecosystems. Additionally, understanding their dynamics is crucial for improving crop yields while minimizing environmental harm. Regular monitoring can guide farmers in maintaining soil fertility and establish policies aimed at mitigating pollution, making it a critical component of sustainable land management practices.

Nitrogen exists in the soil in many forms and occasionally transforms very easily from one to another, and among these, nitrate (NO_3^-) is the main form absorbed by plants and a key nutrient for their growth [107]. However, its excessive accumulation can lead to water contamination, soil degradation, and the release of harmful greenhouse gases. Phosphorus, usually present in the form of phosphate, aids in plant roots formation, photosynthesis and promote disease resistance; on the other hand, the over-fertilization may lead to nutrient leaching, water pollution, and irreversible harm to aquatic

lives [108]. Therefore, it is fundamental develop sensors for phoshates and nitrates. Traditional methods consists of soil sampling and subsequent laboratory analysis, often costly and time consuming. Alternative and rapid sensors have been proposed and rely on eletrochemical sensing, often based on the installation of probes in the soil. However, the need of frequent calibrations, the power requirements and the heterogeneity of the soil (i.e., with variations in moisture, temperature, pH) are the major disadvantages of this type of sensors.

Here, we sought to perform a screening of four *E. coli* promoters known in the literature, with the aim of selecting those suitable for our final goal of real soil monitoring through the sensing ELMs.

Nitrates

The regulation of nitrate and nitrite in bacterial cells is primarily controlled by the NarX-NarL two-component system, a mechanism that responds to fluctuations in the external environment. Specifically, this system is activated in response to changes in oxygen availability or exposure to nitric oxide [82]. The NarX-NarL system plays a critical role in modulating cellular responses to these stimuli. Prior research has identified the yeaR-yoaG operon as being inducible not only in response to nitric oxide, but also to the presence of nitrate and nitrite [109, 110]. Given our focus on detecting nitrate, we were interested in this operon. However, because nitrite and nitric oxide are also important signaling molecules in various biosensing applications, we decided to further investigate and characterize the yeaR promoter with a specific focus on its potential use in nitrate detection.

In addition to the yeaR promoter, we considered another system of interest: the NorR system. This system is crucial for bacterial defense against nitrosative stress, particularly in detoxification nitric oxide and reactive nitrogen species derived from it. Hutchings et al. previously reported that NorR-dependent activation of norV transcription occurs when the bacterium is exposed to nitric oxide, specifically through exposure to NO+ donors or nitric oxide-generating compounds such as nitroprusside [83]. Based on these findings, we included the norV promoter in our initial investigations, given its role in nitric oxide metabolism and its potential utility in nitrate detection.

We conducted our screening experiments utilizing M9 minimal medium as the growth substrate, since earlier studies that demonstrated lower levels of induction for the yeaR promoter by nitrate when grown in complex medium [82]. Conversely, research has shown that the norV promoter is activated by nitrate in minimal media as effectively as it is by nitroprusside [83]. As our primary objective was to detect nitrate, our initial screening involved conducting an induction assay using ammonium nitrate (NH_4NO_3)

and potassium nitrate (KNO_3) as sources of nitrate, with concentrations ranging from as low as 1 nM to as high as 10 mM.

Our experimental data revealed that, during both the exponential and stationary growth phases, the yeaR promoter outperformed the norV promoter in terms of its effective operational range, at least within the tested nitrate concentrations. Additionally, no significant differences were observed between the two nitrate sources used (Fig. 3.7, A). During the exponential growth phase, the yeaR promoter exhibited saturation starting at nitrate concentrations of around 0.1-1 mM, with a FC of 9 observed at the highest tested concentration. In the stationary phase, the yeaR promoter reached a plateau starting at the 1 mM concentration, with normalized RFP levels increasing by approximately 18-fold between the 0 mM and 10 mM nitrate concentrations. Although the norV promoter is well known for being activated primarily by nitric oxide, we observed significant activation even with nitrate exposure. Specifically, fold changes of 6.5 and 10 were detected at the highest nitrate concentration during the exponential and stationary phases, respectively. These findings align with the work of Gardner et al., who also reported norV transcriptional activation in response to nitrite or nitrate, as both compounds can act as NO+ donors [111].

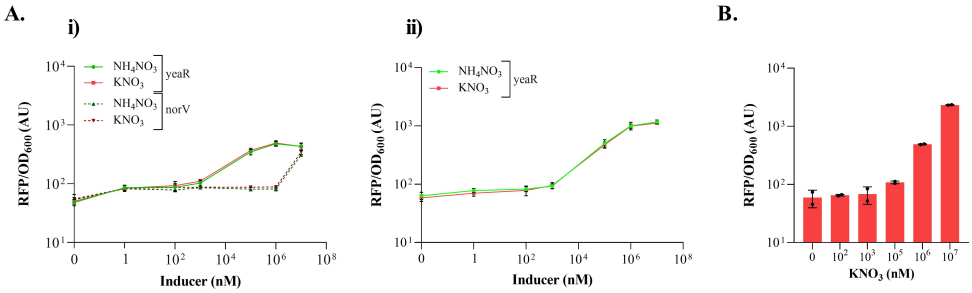

Figure 3.7: Dose response curve of nitrate sensors. A) Response in exponential (i), and stationary phase show only for yeaR (ii). A range of 7 concentrations of NH_4NO_3 and KNO_3 were selected for both of the sensors. The stationary phase response confirmed yeaR as best promoter for a nitrate sensor. Solid and dotted line represent the mean of three replicates for yeaR and norV promoters, and error bars represent the standard deviation. Gain = 50. B) Dose response curve of yeaR promoter upon induction of KNO_3, in low-oxygen condition, in stationary phase. Bars represent the mean of a biological duplicate, black points are the single values and error bars the standard deviation.

Next, we turned our attention to investigating the activity of the yeaR promoter in response to potassium nitrate (KNO_3) under low oxygen con-

ditions, specifically during the stationary growth phase. It is essential to study microbial biosensors under both aerobic and low oxygen conditions in order to fully understand their operational range, limitations, and potential applications. Considering that our goal was to design a promoter system for sensing nitrate in soil environments, we aimed to thoroughly characterize its robustness under oxygen-varying conditions. Upon induction, we observed a similar level of activity up to a concentration of 1 μM. However, at the 10 mM concentration, the yeaR promoter exhibited a substantially higher fold change, around 38 (Fig. 3.7, B). This observed difference between aerobic and anaerobic conditions is likely due to the preferential use of oxygen by *E. coli* during respiration. Oxygen serves as a more efficient electron acceptor than nitrate, meaning that under aerobic conditions, nitrate is not significantly involved in the respiration process, leading to lower activity of the NarX-NarL system. Consequently, the yeaR promoter is less likely to be activated in the presence of oxygen because the bacterial cell does not prioritize nitrate respiration when oxygen is available [112]. This understanding could explain why, under low oxygen conditions, the native yeaR promoter was more strongly upregulated, resulting in higher normalized RFP levels approximately a two-fold increase at the 10 mM nitrate concentration.

In addition to our investigations on nitrate, we extended our study to evaluate the response of the yeaR promoter to both nitrite and nitric oxide under aerobic conditions. For the nitrite experiments, we used sodium nitrite ($NaNO_2$) as the nitrite source, while for nitric oxide, we employed sodium nitroprusside (SNP) as a nitric oxide donor. This choice was made based on previous evidence suggesting that the transcriptional responses elicited by SNP and nitric oxide are highly similar [113].

In our nitrite induction experiments, we explored a range of concentrations, from 0 to 10 mM, to assess the behavior of the yeaR promoter under these conditions. The results demonstrated that, at the highest concentration tested, normalized RFP levels increased by 13-fold during the exponential growth phase and by 17-fold during the stationary phase (Fig. 3.8, A).

However, while these results were promising in terms of promoter response, it is important to consider the practical relevance of these findings for real-world applications. Nitrite concentrations in natural environments, such as soils, are typically very low, generally falling below 1 mg/kg of soil. Given that the concentrations we tested far exceed those commonly encountered in soils, we concluded that further investigation of the yeaR promoter's response to nitrite was not guaranteed. The disparity between the sensor operational range and the actual nitrite concentrations found in soil environments suggested that this promoter is not well-suited for nitrite detection in such contexts, and thus we decided not to pursue additional experiments

focused on nitrite sensing.

For the nitric oxide experiments, we took a more in-depth approach by comparing the response in two different types of growth media: a nutrient-poor version of M9 minimal medium and the standard M9 medium that we typically use. Medium composition is a critical factor in the characterization of biosensors, as different media can have substantial impacts on promoter activity and sensor sensitivity. Previous research has indicated that complex media can alter the yeaR promoter response to SNP, leading to changes in how the sensor detects nitric oxide [82]. Our results supported these findings, as we observed a significantly higher level of promoter activity in the poor M9 medium version. Specifically, in the poor M9 condition, the yeaR promoter activity increased by approximately 2-fold compared to the standard medium (Fig. 3.8, B).

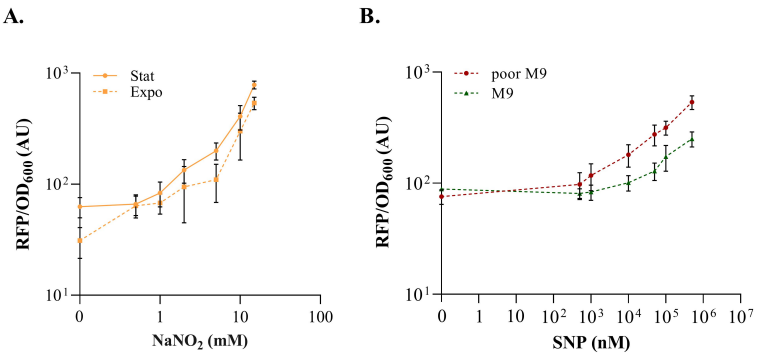

Figure 3.8: Dose and response of yeaR sensor in aerobic conditions upon induction of nitrite and nitric oxide. A) Dose and response of yeaR promoter upon induction of $NaNO_2$, reported for log and stationary phase. B) Dose and response of yeaR promoter upon induction of SNP, in poor or standard M9 medium, in log phase. A-B) Solid or dotted line represent the mean of three replicates, and error bars represent the standard deviation. Gain = 50.

It is important to note that our experimental setup differs from that of the study conducted by Li et al. [82], which used a defined and enriched medium based on MOPS, with or without glucose supplementation. This distinction is crucial because their medium was significantly more enriched than ours, and thus the results of their experiments may not be directly comparable. However, in our setup, the poor M9 medium condition exhibited a FC of approximately 7 at the highest SNP concentration tested, and this fold change increased to greater than 16 during the stationary phase.

These findings highlight the influence of medium composition on the re-

sponse to nitric oxide and emphasize the importance of carefully selecting experimental conditions when characterizing biosensors. Using a nutrient-poor medium, we were able to enhance the sensitivity of the yeaR promoter to nitric oxide, particularly during the stationary phase.

Overall, the data we have collected strongly suggest that the yeaR promoter has significant potential as a versatile biosensor capable of detecting various nitrogen-based compounds. Despite the low sensitivity and operating range, its responsiveness to different nitrogen species, including nitrate and nitric oxide, makes it particularly valuable for a wide range of applications. In the context of nitrate detection, the yeaR promoter could be employed as a reliable sensor in environmental monitoring, specifically for soil analysis, where nitrate concentrations are of crucial importance for agricultural practices and ecosystem health. Accurate nitrate detection is essential for managing soil fertility, monitoring pollution levels, and optimizing fertilizer usage, making the yeaR promoter a promising candidate for such tasks.

Moreover, the promoter's ability to respond to nitric oxide presents additional opportunities in biological and biomedical applications. Nitric oxide is a critical signaling molecule involved in a variety of physiological processes, including immune response, vasodilation, and neurotransmission, as well as being a marker for oxidative stress and inflammation in cells. The yeaR promoter's sensitivity to nitric oxide could be harnessed in the development of biosensors for detecting and quantifying nitric oxide in biological systems, offering valuable tools for research into cellular stress responses or disease diagnostics. For example, Iverson et al. have highlighted the utility of nitric oxide sensors in biological research and therapeutic applications, further supporting the yeaR promoter's potential in this area [114].

In summary, the yeaR promoter demonstrates remarkable versatility as a biosensor, with applications ranging from environmental monitoring to biomedical research, and with the necessary tuning and adjustments to amplify the response or improve the LOD it offers a robust platform for detecting key nitrogen-based molecules.

Phosphates

E. coli tightly regulates its phosphate metabolism through a specialized set of genes known as the Pho regulon, which consists of more than 31 genes organized into eight distinct transcriptional units. This regulatory network is primarily controlled by the PhoR-PhoB two-component system, a well-conserved mechanism that forms a critical global regulatory circuit responsible for managing bacterial phosphate levels [115]. The key components involved in this regulation are the sensor kinase PhoR and the response regulator PhoB. Additionally, the phosphate transporter system Pst (a Pi-

specific transporter) and the regulatory protein PhoU are instrumental in fine-tuning this response by modulating the activity of PhoB in response to environmental phosphate levels [116].

During conditions of phosphate limitation, PhoR is activated, which in turn phosphorylates PhoB. The phosphorylated form of PhoB acts as an active transcriptional regulator, binding to promoter regions containing a specific consensus sequence known as the PHO Box. This binding initiates the transcription of genes that are part of the PHO regulon, which are essential for phosphate acquisition and management under conditions of startvation. Conversely, when phosphate levels are abundant, the interplay between PhoR, Pst, and PhoU leads to the dephosphorylation of PhoB, effectively turning off the PHO regulon and stopping the transcription of these phosphate-responsive genes. The dephosphorylated PhoB is inactive and thus unable to initiate gene transcription, conserving resources when phosphate is plentiful.

Our research focused on characterizing the promoters of two key genes within the PHO regulon, phoB and phoA. These genes have been previously utilized as effective biosensors for monitoring phosphorus bioavailability across a variety of bacterial species.

Given that phosphate was the molecule to be detected in our system, we employed a modified version of M9 minimal medium (described in the next section, 3.1.2) to avoid interference from excess phosphate. This optimized medium contained a low concentration of 0.1 mM phosphate, providing a controlled environment for assessing sensor performance. To investigate further, we conducted induction assays using potassium phosphate (K_2HPO_4) under aerobic conditions.

Our experiments confirmed that both the phoB and phoA promoters were repressed in response to increasing phosphate concentrations (Fig. 3.9, A). Consistent with prior studies, the regulation of the phoB promoter mirrored that of the phoA promoter [84]. The repression of these sensors was evident at phosphate concentrations higher than 100 μM and 200 μM, respectively, with no observable gene expression specifically from 500 μM. Given that the phoB promoter exhibited a smaller dynamic range in its response to phosphate levels, we selected the phoA promoter as the primary phosphate sensor for our system.

As previously mentioned, biosensors designed for detecting pollutants, nutrients, or metabolic by-products in environmental settings must often function in diverse conditions, including both aerobic and anaerobic environments. This is particularly important for applications in soil environments, which can be highly heterogeneous, with some regions being oxygen-rich and others oxygen-poor. In light of this, we extended our investigation to evalu-

ate the performance of the phoA sensor under low oxygen conditions, similar to our prior work with a nitrate sensor. The results from this assay were consistent with those obtained under aerobic conditions (Fig. 3.9, B), showing a similar trend of induction in response to phosphate levels, with a slight increase in promoter activation between 0 and 100 μM phosphate.

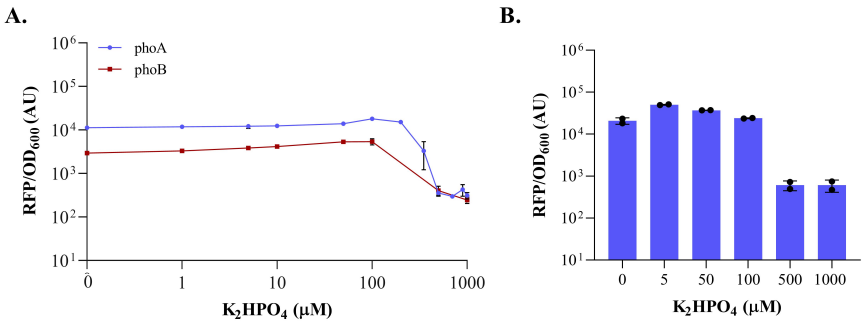

Figure 3.9: Dose and response curve of phosphate sensors in stationary phase. A) A range of 8 concentrations of K_2HPO_4 were selected for both of the sensors (red squares), and extended up to 12 for phoA for a further characterization (blu circles). Solid line represents the mean of three replicates and error bars represent the standard deviation. Gain = 50. B) Dose and response of phoA sensor under low oxygen conditions. Bars represents the mean of two replicates, black points each value, and error bars represent the standard deviation.

These findings demonstrate that the phoA promoter is a versatile and effective phosphate sensor, valuable for monitoring phosphate bioavailability across diverse environmental settings.

3.1.2 Abiotic component optimization

This part of our study focused on the optimization of the M9 medium used to cultivate the microbial sensors, which were later selected and printed as ELMs. One of the key findings that emerged from our initial characterization of the biosensors, conducted in liquid assays, was that the sensors exhibited better performance when grown in M9 minimal medium compared to the commonly used LB medium. However, this improvement in sensor functionality came with a significant challenge. The use of M9 medium in the formulation of our bioink led to issues with the stability of the printed ELMs, causing the material to flake off easily after the crosslinking process (Fig. 3.10, A).

In response to this challenge, we made an initial attempt to optimize the bioink formula by adjusting three key variables: the concentrations of sodium alginate and calcium chloride ($CaCl_2$), and the crosslinking time. The specific combinations of these variables that we tested were as follows: sodium alginate concentrations of 8% (as a reference, since it is the concentration of our protocol), 10%, or 12%; $CaCl_2$ concentrations of 2% or 3%; and crosslinking times of 7 or 15 minutes. To assess and compare the performance of these different conditions, we used a strain of *E. coli* that constitutively expressed RFP.

Neither increasing the sodium alginate concentration to 10% or 12%, nor extending the crosslinking time to 15 minutes solved the flaking issue. In fact, higher $CaCl_2$ concentrations and longer crosslinking times appeared to negatively affect RFP production, possibly due to oxygen depletion in the more densely crosslinked matrix. As a result, we decided to retain our original bioink formula and shift our focus towards investigating the composition of the M9 medium itself, to better understand its role in causing the instability of the printed ELMs.

Our next step was to conduct a preliminary test to qualitatively identify which components of the M9 medium were contributing to the melting of the ELM structures. Through a series of tests, we determined that all medium combinations resulted in material flaking, except the one where the M9 salts were omitted entirely. This observation led us to hypothesize that the issue was related to the presence of M9 salts, which include phosphates such as Na_2HPO_4 and KH_2PO_4, as well as sodium chloride (NaCl) and ammonium chloride (NH_4Cl). We proposed that there might be a competitive interaction between the phosphate ions in the M9 medium and the calcium ions in the bioink formula, resulting in an unstable calcium-alginate barrier. This competition could be disrupting the crosslinking process, thereby compromising the integrity and stability of the 3D structure of the ELMs.

To address this issue, we considered modifying the M9 medium by reducing the phosphate concentration rather than removing it entirely. Phosphate is an essential component for bacterial growth, so its concentration in the medium must be carefully balanced. In minimal media like M9, phosphate is typically supplied in the form of Na_2HPO_4 and KH_2PO_4 at a combined concentration of approximately 69 mM. If the phosphate concentration is reduced too much, it can significantly impact bacterial metabolism. For instance, reducing the phosphate concentration to just 10% of the standard amount in M9 medium has been shown to result in lower cell density and altered metabolic behavior, including increased glucose consumption and elevated acetate production, even though *E. coli* cells can survive with phosphate levels as low as 1% of the typical concentration [117].

In addition to considering the phosphate concentration, we also hypothesized that the removal of phosphate could have affected the pH stability of the medium, which is another critical factor for the proper functioning of biosensors, as mentioned above for example for the acetate sensor. To mitigate potential pH fluctuations, we included Good's buffers in two versions of the modified M9 medium recipes. Good's buffers, such as PIPES and MOPS, are specifically designed to maintain a stable pH and resist changes in ion concentration during biological experiments. By using these buffers, we aimed to create a more stable environment for bacterial growth and gene expression. For the concentration of both PIPES, and MOPS buffer we chose those previously used in the laboratory that had proven compatible with bacterial growth.

To evaluate the effectiveness of the modified media, we conducted experiments to assess both the growth and gene expression of the VAI model sensor, which expresses RFP as a reporter. We tested the sensor under three different concentrations of the inducer (i.e., 0, 2, and 20 nM) in both the exponential and stationary growth phases. In these tests, we selected 0.1 mM KH_2PO_4 as the minimum phosphate concentration necessary to support bacterial growth without compromising the functionality of the bioink. The media conditions we compared were as follows, with standard M9 serving as the reference for both bacterial growth and gene expression:

- M9 without Na_2HPO_4, PIPES 100 mM and KH_2PO_4 0.1 mM;
- M9 without Na_2HPO_4, MOPS 50 mM and KH_2PO_4 0.1 mM;
- M9 without Na_2HPO_4, KH_2PO_4 0.1 mM.

The results demonstrated that all the tested medium recipes were compatible with bacterial growth, and RFP production followed a dose-response curve as expected (Fig. 3.10, B). In the exponential phase, the differences between the various media were minimal. However, during the stationary phase, we observed slight variations in RFP levels across the different conditions. This suggests that while the phosphate concentration and the inclusion of buffers had a limited effect during rapid growth, they may play a more significant role in the regulation of gene expression and biosensor functionality during the stationary phase, probably due to the different buffering properties of the media.

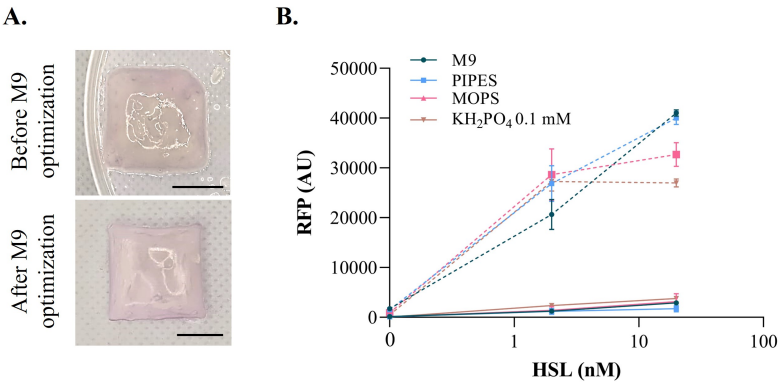

Figure 3.10: Abiotic component optimization. A) Pictures of RFP-expressing ELMs made using standard M9 (on top), and the final optimized M9-PIPES, reducing phosphates (on bottom). Before optimization tha material appeared almost melt and was not as stiff as expected. Scale bars = 1 cm. B) Dose response curve in liquid assay in terms of RFP (AU), using the VAI sensor at three concentrations. Standard M9, phosphate-reduced M9 (KH_2PO_4 0.1 mM) with or without buffers (100 mM PIPES, or 50 mM MOPS) were tested and compared. The solid lines are the exponential phase, while the dashed lines the stationary one.

The medium containing PIPES proved to be particularly effective, reaching RFP expression levels comparable to those achieved with the standard M9 medium. Given this observation, we selected the PIPES-containing medium as the preferred choice for subsequent bioprinting experiments. Our primary objective was to maximize the expression of RFP in the ELMs following induction, and the PIPES-buffered medium fulfilled this requirement.

Moreover, an important aspect of this optimization was the structural integrity of the printed ELMs. No material dissolution or flaking was observed with the use of this modified M9 medium, in stark contrast to the issues encountered with the original M9 formulation. This confirmed the success of the medium optimization process, as the newly formulated medium not only supported robust bacterial growth and RFP production but also maintained the stability of the bioink post-crosslinking (Fig. 3.10, A). This stability is crucial for ensuring that the printed ELMs remain intact and functional throughout the duration of their intended applications, highlighting the effectiveness of the PIPES-based solution in meeting both growth and structural requirements.

3.1.3 In-depth biosensing characterization for the best performing candidates

This section focuses on the series of experiments that were conducted using the newly developed M9 PIPES culture medium with low phosphates concentration. These experiments were carried out prior to advancing to the subsequent steps of printing and characterizing the biosensing ELMs. Although the M9 PIPES medium had already been validated for the VAI sensor, we deemed it necessary to conduct a fresh round of dose-response tests with our most promising candidate sensors, specifically those designed to detect acetate, nitrates, and phosphates. This additional testing was essential because any additional interactions between the biosensing material and the new culture environment (e.g., low phosphates, pH buffer) must be carefully considered and accounted for. Additionally, we aimed to more thoroughly characterize the performance of these sensors considering the real-world conditions for which they were designed. This meant considering specific environmental factors that could impact sensor functionality, such as varying pH levels that could be encountered in such different environments (e.g., digestate, soil). We also explored potential interactions, or cross-talk, between phosphate and nitrate, recognizing that both nutrients coexist in soil. Understanding these interactions was critical for refining sensor performance and ensuring they are robust enough for practical application in field conditions.

Acetate sensor

The sensor glnaP2 was tested upon induction of acetic acid in aerobic and low oxygen conditions, using the customized M9 PIPES adjusting the pH to 6 for each induction or without any stabilization. In fact, from the previous studies we did observe how this sensor in particular is affected by pH changing and acidic environment. Thereferore, before printing the respective ELMs, we sought to better understand its response and which condition would lead to a better sensitivity using the M9 PIPES medium. Both conditions, aerobic and low oxygen, have shown that pH 6 results in a higher level of normalized RFP, as we have seen before, but with a higher leakiness, resulting in a lower dynamic range, with a FC about 2.6 at the concentration od 25 mM (Fig. 3.11, A-B). By contrast, M9 PIPES without changing pH reported a FC about 8 at the highest concentration tested, along with a better operating and dynamic range.

Overall, the medium changing moving from the defined M9 to the low phosphate with PIPES affected the sensor response. This is not surprising, since the Pho regulon is a global regulatory mechanism comprising several genes involved in storage and saving nutrients, such as but not limited to

phosphorus.

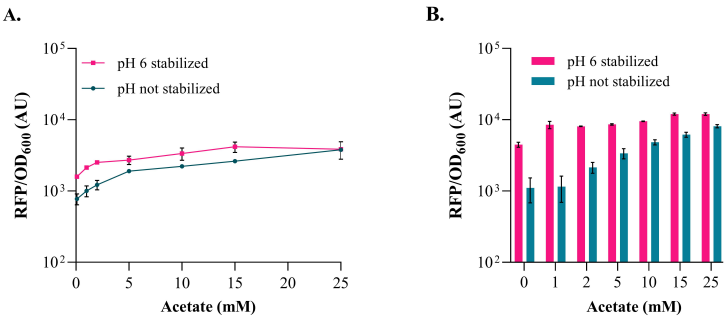

Figure 3.11: Dose and response curve of the acetate sensor using the low phosphate M9 PIPES medium. A) Normalized RFP of the acetate sensor upon induction of acetic acid, adjusting the pH up to 6 (pink) or without any stabilization (teal blue). Solide lines represent the mean of a biological triplicate, error bars indicate the standard deviation. Data are collected in aerobic conditions in the stationary phase. B) Normalized RFP of the acetate sensor upon induction of acetic acid, adjusting the pH up to 6 (pink) or without any stabilization (teal blue). Bars represent the mean of a biological triplicate, error bars indicate the standard deviation. Data are collected in low oxygen conditions in the stationary phase.

Furthermore, putative PHO boxes have been detected in several genes involved in nitrogen metabolism, such as those of the glutamine permease operon glnHPQ and the glnLG two-component system that regulates the glutamine synthetase glnA gene [118]. While the exact mechanism of how PhoP regulates glnA might not always be direct, PhoP can influence glnA expression through its broader role in managing cellular resources during phosphate stress. For instance, PhoP could repress or activate intermediaries in nitrogen metabolism or other global regulators, which in turn affect glnA expression [119]. Higher leakiness of the glnaP2 promoter under phosphate starvation likely arises from the interplay between the PhoP/PhoQ regulatory system and nitrogen regulation through NtrC. This cross-regulation might lead to an increase in basal transcription of glnA, even when nitrogen levels are not limiting, and be part of an adaptive response, allowing the cell to maintain essential nitrogen metabolism during periods of phosphate stress [115, 120].

Nitrate sensor

It has long been established that nitrogen sources and inorganic phosphate content play crucial roles in regulating microbial growth through complex and interconnected regulatory networks [121]. Various studies have explored the impact of limitations in key nutrients, such as phosphate and nitrogen,

as well as the influence of acidic conditions on microbial metabolism. For example, the research conducted by Marzan et al. suggests that metabolic regulation under phosphate and nitrogen limitation, as well as under acidic conditions, is closely interrelated, with significant metabolic shifts occurring particularly during the stationary growth phase [117]. This is particularly relevant for our soil monitoring application, as nitrogen and phosphorus are not only critical for bacterial metabolism but are also essential components of the soil environment, which can exhibit various combinations of nitrate, phosphate, and pH levels ranging from acidic to alkaline.

Despite these insights, there remain numerous unanswered questions regarding the activation and overall function of the entire regulatory system governing these processes. Given these complexities, we decided to investigate the potential interactions between nitrate and phosphate with their respective promoters yeaR and phoA, and to examine how pH variations might influence the behavior of our biosensors.

In terms of nitrate regulation, existing studies suggest that under conditions of phosphate limitation, the regulatory protein PhoP plays a critical role in repressing genes associated with nitrogen assimilation. This is because nitrogen assimilation becomes unnecessary when cellular phosphate levels are insufficient [119]. Motivated by these findings, we set out to investigate how the expression of the yeaR promoter, which is responsible for nitrate sensing, would be influenced by varying nitrate concentrations in combination with increasing levels of phosphate. Specifically, we tested four different concentrations of KH_2PO_4 along side six concentrations of KNO_3, under aerobic conditions, during the stationary phase of bacterial growth.

Our experimental results revealed a clear and positive correlation between the expression of the yeaR sensor and the increasing concentrations of KH_2PO_4 (Fig. 3.12, A). This outcome confirmed our initial hypothesis, which proposed that higher phosphate levels would promote gene expression related to nitrate sensing. This finding underscores the intricate regulatory interplay between nitrogen and phosphate, with changes in phosphate availability influencing nitrate detection mechanisms. Specifically, at the highest concentration of KNO_3 tested, the FC in gene expression ranged from approximately 12 (similar to the FC observed in our defined M9 medium) to around 200, as phosphate concentrations were increased from 0 to 1 mM of KH_2PO_4.

In contrast to the effects of phosphate on yeaR expression, altering the pH of the M9 PIPES medium, which typically hovers around 6.8 to 7.0, did not result in any notable changes to the sensor's dose-response behavior. We tested pH levels of 6.0 and 7.5, but neither pH condition produced a difference in the overall response trend or the normalized RFP signal at the

highest nitrate concentration tested (Fig. 3.12, B). This suggests that the yeaR sensor is insensitive to minor variations in pH within this range, while phosphate presence plays a more significant role in modulating its response.

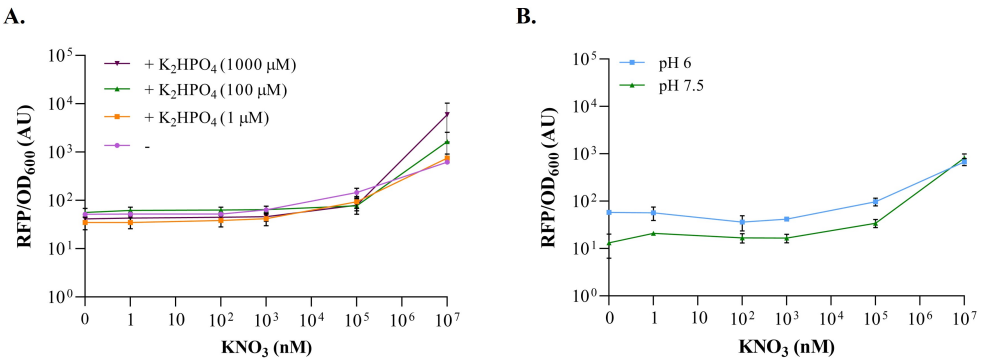

Figure 3.12: Dose response curve of the nitrate sensor tuning some variables. A) The yeaR based sensor's response combining increasing concentration of nitrate and phosphate, to study their interference. B) Dose response curve of the same sensor upon nitrate induction, testing pH 6 and 7.5. A-B) Solide lines represent the mean of a biological triplicate, error bars indicate the standard deviation. Data are collected in the stationary phase, using the low phosphate M9 PIPES.

Phosphate sensor

For the phoA promoter, we applied the same type of detailed characterization that was previously performed for the nitrate sensor. According to findings by Santos et al. [119], under conditions of nitrogen limitation, the members of the phosphate regulon are upregulated, which results in an increase in their transcriptional activity. Conversely, when nitrate concentrations are high, the activity of these regulon members tends to decrease. For a repressor-regulated promoter like phoA, this means that repression can occur at lower phosphate concentrations under certain conditions.

Our experimental data confirmed this behavior. Specifically, as nitrate concentrations decreased, the phoA based sensor became more repressed due to the upregulation of the Pho regulon members (Fig. 3.13, A). This led to a pronounced repression effect, with a clear switch off point occurring at phosphate concentrations about 100 μM. When the concentration of nitrate was increased, not only did the level of repression decrease, but the switch point also shifted significantly. At a high nitrate concentration, such as 10 mM KNO_3, this point dropped dramatically to as low as 1 μM. In this nitrate-rich environment, the sensor exhibited enhanced sensitivity, enabling

detection of phosphate concentrations starting from 1 μM. Under normal conditions, however, the sensor is typically able to distinguish phosphate concentrations only between 100 and 500 μM. These findings underscore the critical importance of considering how the presence or absence of nitrates impacts the phoA sensor's response. For future experiments involving soil samples, it will be essential to generate separate calibration curves for each condition in order to accurately translate the level of RFP expression into the corresponding phosphate output.

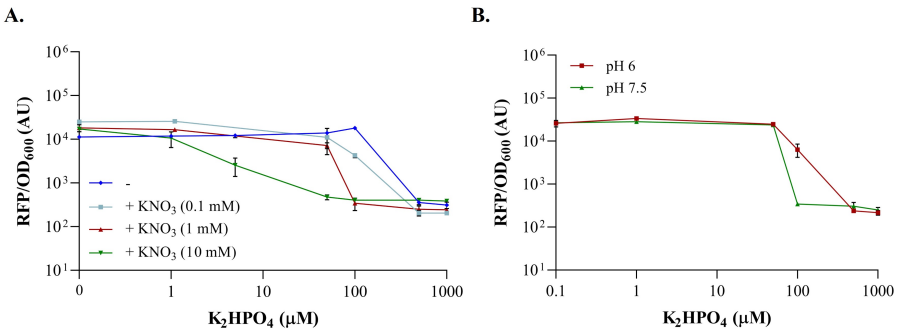

Figure 3.13: Dose response curve of the phosphate sensor tuning some variables. A) The phoA based sensor's response combining increasing concentration of phosphate and nitrate, to study their interference. B) Dose response curve of the same sensor upon phosphate induction, testing pH 6 and 7.5. A-B) Solide lines represent the mean of a biological triplicate, error bars indicate the standard deviation. Data are collected in the stationary phase, using the low phosphate M9 PIPES.

In addition to exploring the nitrate-related effects on the phoA sensor, we also investigated how changes in pH impacted the sensor's performance (Fig. 3.13, B). In contrast to the nitrate sensor, which exhibited minimal variation when the pH was altered, the phoA promoter showed distinct differences in its dose-response behavior depending on the pH level. Specifically, we tested the sensor's response at pH values of 6.0 and 7.5 and observed notable changes in its operating range. Under slightly acidic conditions, with a pH of 6.0, the sensor's behavior was not significantly different from that observed using the M9 PIPES medium, which has a nearly neutral pH of 6.8 to 7.0. However, when we tested the sensor in a slightly alkaline environment with a pH of 7.5, the operating range shifted, with the sensor being effectively turned off at a phosphate concentration of 100 μM.

These findings are consistent with the work of Marzan et al., who showed that genes regulated by PhoB were upregulated under acidic conditions at 6 pH compared to those at 7 pH [117]. Therefore, it is plausible that a

combination of alkaline conditions and the presence of nitrates could enhance the sensitivity of our phoA sensor when used in soil environments.

Overall, this data highlights the necessity of carefully considering environmental factors when developing and calibrating biosensors for real-world applications.

3.2 Biosensing ELMs

As the final step of our biofabrication cycle, we made the ELMs based on glnaP2, yeaR and phoA promoters for testing them as materials, aiming to monitor acetate levels in digestate samples, and nitrates and phosphates in soil samples.

Acetate

The series of experiments conducted with the digestate started by first examining in liquid assays a type of digestate, which was liquid, acetate-free and obtained from a lab-scale reactor based on sewage sludge. The primary goal during this phase was to rule out any potential toxicity that could arise from the digestate, along with evaluating the response of the biological promoter system and detecting any possible interferences that might occur during the process using spiked acetate in digestate. The digestate was first spiked with acetic acid 100X concentrated, added in a microplate as an inducer, and therefore 100X diluted. Having gathered satisfactory results from these initial in liquid investigations, that is not toxicity and a dose response behaviour (Fig. 3.14), we moved forward with the next stage, that is the bioprinting and test of glnaP2-based ELMs.

It is worth emphasizing that the digestate samples, whether they originated from lab-scale reactors or full-scale biogas plants (with detailed information provided in Appendix A), typically exhibited a dark brown to black coloration. This characteristic coloration raised concerns about its potential to interfere with the biosensor readings. Specifically, we were concerned that the dark hue might distort the fluorescent signals, which are crucial for accurately interpreting the activity of the biosensor. However, during our liquid assay experiments, we did not encounter any issues related to the dark coloration of the digestate, as only 2 μl of digestate were used in a total volume of 200. In contrast, for the bioprinting of ELMs, it was necessary to carefully devise an induction protocol that would address the potential impact of the dark color.

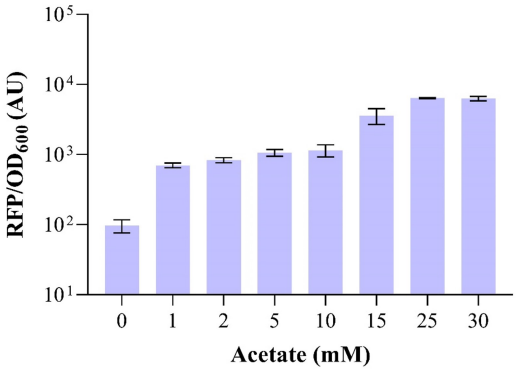

Figure 3.14: Normalized RFP of the acetate sensor upon induction of spiked digestate, using the low-phosphate M9 PIPES medium. Data are collected in the stationary phase, in low oxygen conditions. Bars represent the mean of a biological triplicate, error bars indicate the standard deviation.

To address this issue, we conducted preliminary experiments aimed at identifying the most suitable experimental setup. These exploratory tests involved multiple approaches: first, we attempted to have the digestate absorbed by agar to utilize it as a solid matrix; second, we explored the possibility of using the digestate in its natural, sludge-like form; and third, we considered isolating the liquid phase of the digestate and using it as a standard inducer. Each of these approaches was evaluated to determine the best condition for incorporating the digestate into the experimental system without compromising the accuracy of the biosensor readout.

All experiments were carried out using the glnaP2 sensor system, a construct lacking the RFP serving as a negative control, and a third strain constitutively expressing RFP, acting as a positive control. Including these two controls was essential for several reasons. First, the negative control, which is conveniently used to remove any background of auto fluorescence, here it also exploited to remove the influence of the dark coloration of the digestate. After analyzing more than 200 samples, it became evident that the digestate samples varied significantly in terms of color, dry content, and general appearance. Therefore, we deemed it necessary to include a negative control for each digestate sample in the experimental setup to properly take into account possible fluctuations in the autofluorescence values. On the other hand, the positive control played a critical role in assessing the toxicity of the digestate samples. By monitoring the development of RFP in the positive control, we could determine whether the digestate negatively impacted the biological system.

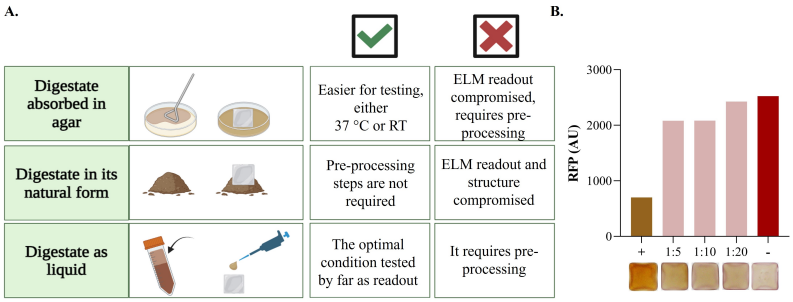

Figure 3.15: Set-up for using digestate samples. A) Three conditions were investigated before establishing a set-up for the detection of acetate in digestate samples: absorbed in agar, its natural sludge form, or in liquid were evaluated in terms of structure integrity, and readout comprimise. The condition in which digestate is used taking only its liquid part was chosen as trade-off between the required pre-processing and the biosensor response. B) Normalized RFP outcome from constitutively RFP expressing ELMs incubated or not with 200 μl of digestate (diluted or not).

In summary, we screened the three experimental conditions, which are digestate absorbed into agar, digestate in its natural sludge form, and digestate in its liquid phase, by evaluating two main criteria: the level of RFP expression and the structural integrity of the materials. After thorough analysis, we eventually selected the condition where the liquid fraction was extracted from digestat as the most suitable for further experimentation (Figure 3.15, A). This choice was based on its superior performance in terms of RFP development and material stability, even though it requires pre-processing steps such as the use of the centrifuge, filtering and dilutions, which are still acceptable as minimal processing steps, not requiring additional reagents. On the other hand, the use of whole digestate did not guarantee reproducible amounts of liquid, as the dry matter considerably varied and data were extremely variable among replicates (data not shown). The need to dilute the digestate comes from wanting it to interfere less with the biosensor output. As preliminary data have shown (Figure 3.15, B), in fact, the output of a constitutively RFP strain significantly decreased its signal, and this led us to choose the 5-fold dilution to avoid interference.

With the optimal setup identified, we started testing the sensor with real digestate samples. For these experiments, which involved a large number of printed ELMs, we used a smaller patch design including a non induced ELM to monitor the basal RFP level. Unlike previous experiments in which a piece of ELM was cut and analyzed, these patches were analyzed in 48-well plates with multiple readings per well.

First, we proceeded carrying out experiments using digestate samples

from both full-scale and lab-scale reactors that did not contain acetate, based on previous gas chromatography (GC) analyses by the Catholic University of the Sacred Heart (Piacenza). We employed spiked acetic acid samples to establish calibration curves. Across all the digestate samples, which varied in origin and color, we observed a clear dose-response relationship with the ELMs (as illustrated in Fig. 3.16, A).

Subsequently, we analyzed two digestate samples derived from a laboratory-scale, two-stage biogas plant operating continuously. The first sample was collected from the initial reactor, devoted to the acetogenesis, while the second sample came from the second reactor, which corresponds to the methanogenesis phase. The first sample containing 7156.91 mg/L acetic acid achieved a clear induction of the sensor with a 7-fold higher RFP level than the second sample containing 299.59 mg/L (Fig. 3.16, B), which was close to the background level of the sensor output. The result obtained is in line with what was expected: considering the 5X dilution, and considering the molar weight of acetic acid, the first sample containing 7156.91 mg/L of acetate after the dilution has a molarity of approximately 25 mM, and reached an RFP level consistent with the calibration curve at the same concentration.

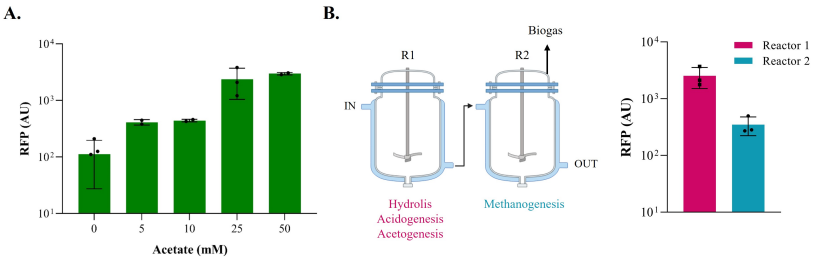

Figure 3.16: Acetate sensing ELMs tested upon digestate induction. A) Dose and response curve obtained starting from a spiked digestate. B) Acetate ELMs tested with digestate samples coming from a two-stages lab-scale plant. A-B) Bars refer to the mean of a biological triplicate, black points are the single values, and error bars the standard deviation. RFP levels are shown after removing the background of the negative control, and the 0 mM condition of graph A was also used as a reference for B as the ELMs were tested and analyzed in the same batch.

The final stage of this study involved testing 200 real samples collected from both full-scale and lab-scale biogas plants. These samples represented digestate from single-stage processes and were characterized by diverse feeding patterns, including continuous and batch processes. The substrates processed included cattle manure, pig slurry, chopped maize, and agri-food waste. We introduced an additional negative control based on the glnaP2

sensor system tested with water. Considering the samples from the three full-scale plants, GC data for a representative number of sampled time points showed an acetate level in the range 0-500 mg/L, which corresponds to a very low content. For all samples, but three, we did not observe RFP signals greater than the negative control obtained with just water induction (Fig. 3.17, A-B). This confirmed the absence of acetate at high levels and attested to the success of the methanogenesis process, thereby assensing the quality of the biogas production process over time.

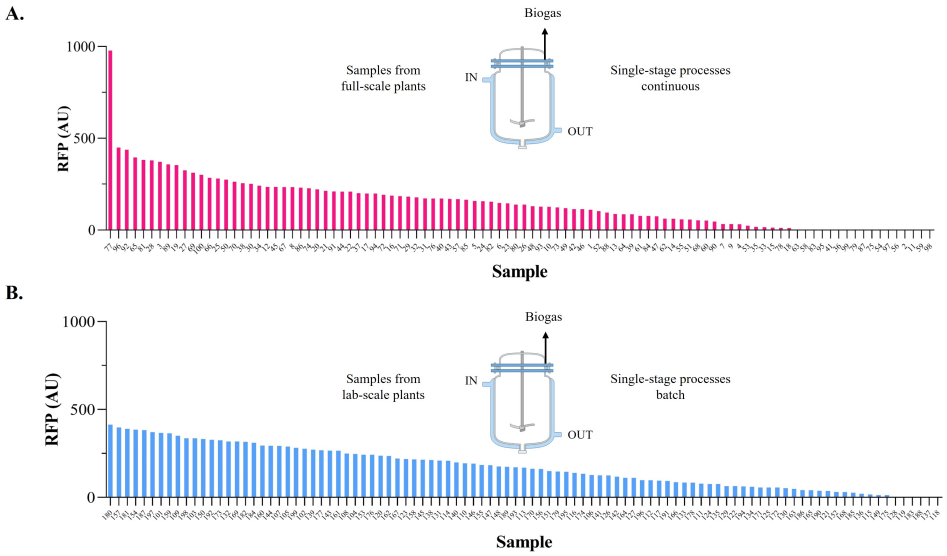

Figure 3.17: Acetate sensor ELMs tested with different types of digestate. The glnaP2-based ELMs were tested with a total of 200 samples of digestate, coming from single-stage reactors, fed in continuous (A) or in batch (B). Bars represent the RFP level of a single replicate. RFP levels are shown after removing the background of the negative control for each digestate, and NC refers to a glnaP2 patch tested with water after subtracting its background in the same condition.

Among the other three samples (all from the first batch), especially one reported an high level of RFP (Fig. 3.17, A sample 77). The respective GC analysis registered a 5451,04 mg/L acetic acid level, that means a molarity of approximately 20 mM after the 5 fold dilution, according to our sperimental set-up. This result, along with the response obtained from the samples 96 and 92 (Fig. 3.17, A second and third in our screeening), which reported high level of acetic acid detected through GC, highlines that the sensor is effectively able to perform in real digestate. Unfortunately, also according to the calibration curve, the actual level of acetate after the 5 fold dilution is

for these samples close to the switch point (especially for 92 and 96, which are lower than 20 mM), so it might be not accurated and sensitive in that range, since it represents the LOD for the ELM sensor.

In conclusion, the data obtained from this research clearly demonstrated the feasibility of using glnaP2-based ELM biosensors to detect acetate in complex and real matrices such as digestate. Additionally, the robustness of the biosensor platform was confirmed by its successful application to digestates from different biogas plants, representing various processes and feeding patterns, as well as different substrates, whether in one or two-stage systems.

Nitrates and phosphates

Since soil is a not liquid-like sample nor can easily be turned into liquid, as we did for digestate, its use with ELMs biosensors required a minimum of design. Previously [74] what we did was pre-incubate the patch at 37 °C overnight and place it into the soil the following day for the induction at room temperature (RT). So far, it has proven to be an effective set up for model sensors (i.e., VAI), but then we thought it would pose a problem for real sensors with both lower detection ranges and fluorescence developed. Therefore, the experiments we carried out for in soil sensing started with the screening to find the optimal set up, tuning temperature and modality of incubation, and precence of additional nutrient supply.

The first screening we performed involved the induction of yeaR-based ELMs under 3 concentrations of KNO_3 diluted in water and subsequently used to induce soil for each condition (as described in Appendix A). The conditions tested are the following (illustrated in Fig. 3.18, A):

- 1) pre-incubation, tested at RT, w/o nutrient supply, (used as reference);
- 2) pre-incubation, tested at RT, with nutrient supply,
- 3) pre-incubation, tested at 37 °C, w/o nutrient supply;
- 4) pre-incubation, tested at 37 °C, with nutrient supply;
- 5) no pre-incubation, tested at 37 °C, with nutrient supply;
- 6) no pre-incubation, tested at RT, with nutrient supply;

We excluded from our analysis the conditions where the ELMs were not pre-incubated and tested without nutrient supply (i.e., conditions 5 and 6). Our reasoning was that these settings would likely lack the necessary conditions for sufficient bacterial growth and subsequent gene expression. Similarly, we chose not to evaluate conditions involving pre-incubation at 37 °C

followed by testing at 37 °C (conditions 3 and 4) because this would result in a total incubation time of two days. We deemed these conditions unreliable, as they would allow for excessive bacterial growth, which could artificially increase the levels of RFP, not because of improved sensing but rather due to the extended growth period.

Indeed, our experimental results confirmed that these two conditions (3 and 4) produced the highest levels of RFP. However, this occurred even in the absence of nitrates, which we anticipated due to the prolonged incubation period (as shown in Fig. 3.18, B). Overall, the experimental set-up that involved overnight pre-incubation at 37 °C emerged as the most effective. Interestingly, the presence or absence of solid agar during testing did not significantly affect the results. For instance, the reference condition (1) ranked third in the overall performance.

One possible explanation for the limited impact of the solid agar medium on RFP production could be the interaction between the soil and the agar. The soil may act as a dehydration agent, absorbing water from the agar and thereby reducing the availability of nutrients for the ELMs placed on top. This observation led us to select the reference condition (1) for further experimentation. Specifically, we aimed to develop a dose-response calibration curve across multiple nitrate concentrations using biological triplicates. The data is presented as milligrams of N-NO_3 per kilogram of soil, which is a common standard for soil analysis.

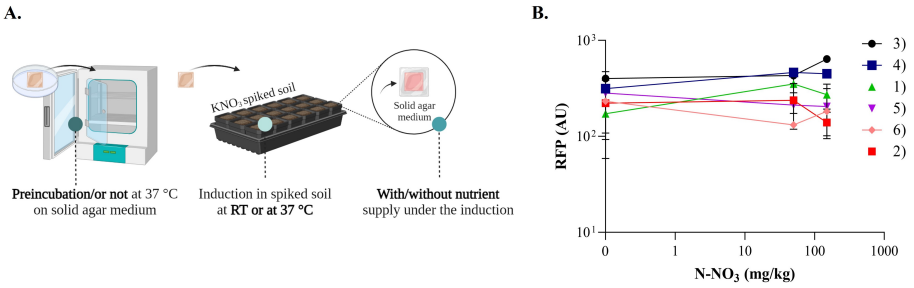

Figure 3.18: Nitrate sensor set-up and dose and response characterization in soil. A) The three levels of tuning for the soil nitrate sensor set-up: pre-incubation, temperature during induction and presence of additional nutrients during the test. By combining these options we kept the 6 most reasonable combinations, eliminating those that would have resulted in not growing. Solid lines are the mean of a biological duplicate, and error bars represent the standard deviation. The label of the 6 conditions (as listed above) are sorted in the legend according to the highest RFP level reached.

Using the initial experimental setup described above, we proceeded to generate a calibration curve to assess the sensor's response to varying nitrate concentrations in the soil (Fig. 3.19.A). From these experiments, we observed significant variability in the sensor response. From these experiments, we observed significant variability in the sensor response. We believe this variability may be attributed to several factors, including having used the set up in which a piece of ELM is analyzed, and not reading the entire patch in the multi-well plates. Second, soil is a non-liquid matrix and therefore inducer diffusion can certainly have more complex dynamics than in the biosensing cases seen so far. Nonetheless, we observed a consistent curve as nitrates increased, especially for concentrations greater than 10^3 mg/Kg of N-NO_3 (Fig. 3.19, B).

Regarding the interference of phosphates and nitrates in soil, our data did not reveal significant differences at the concentrations tested (data not shown).

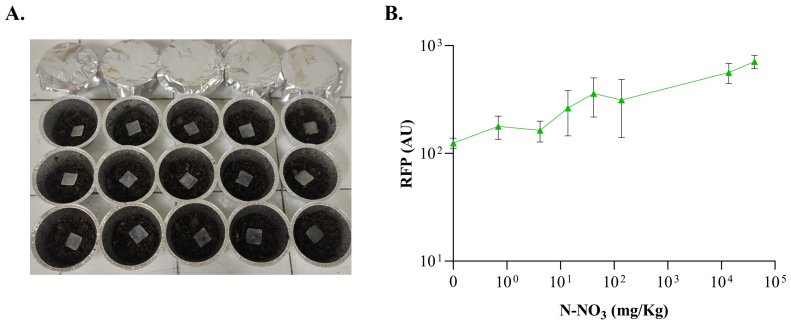

Figure 3.19: The yeaR-based ELMs tested in soil with the final set-up. A) Example of how yeaR ELMs are used in this type of experiment: after the pre-incubation the patch is place on top of the soil, previously mixed with water and KNO_3, in disposable aluminum foil ramikins. B) Dose and response curve obtained from yeaR-based ELMs tested with our refernce protocol for in soil biosensing. Solid lines are the mean of a biological triplicate, and error bars represent the standard deviation.

Our next steps will involve testing the sensor in real soil samples, which can vary considerably in their moisture content, texture (e.g., muddy, dry, or clayey), and other physical properties. Therefore, the experimental setup will require optimization for each specific soil type. It would be ideal to obtain a calibration curve for each soil type to ensure accuracy.

Finally, we shifted our focus to printing phoA-based ELMs, which represent the only repressor in our sensor collection. The first challenge we faced

was determining the optimal method for using this sensor, such as whether to pre-incubate the ELMs and whether to conduct the tests at room temperature. Notably, overnight pre-incubation at 37 °C, a method commonly used in our experiments, is not suitable for this sensor. Since phoA is a repressible promoter, pre-incubation without phosphates leads to RFP production in all tested ELMs, thus compromising the results.

The phoA-based ELMs were printed, and stored in the fridge. The following day we placed them on M9 PIPES agar with a range of phosphates, and eventually tested directly by incubating at 37 °C. The day after, we analyzed the patches using both the microplate reader and the measurement with the a* channel since, being a strong promoter, we expected RFP visible to the naked eye. The experiments with the ELMs confirmed the results obtained in liquid assays, and therefore, concentrations below 100 μM lead to strong RFP, while 1000 μM turns off the sensor. Data from microplate reader and a* channel reported the same type of output with a high correlation (R^2 = 0.903).

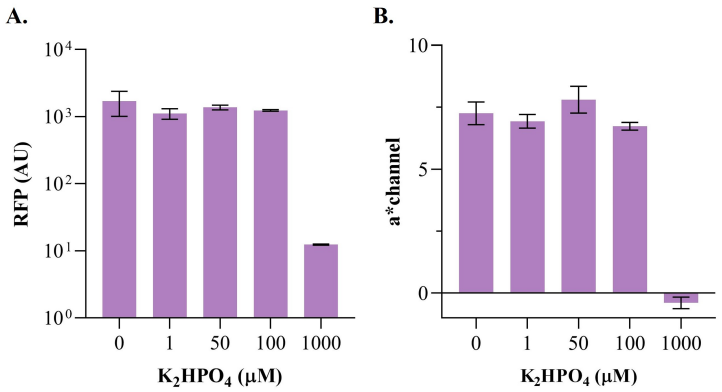

Figure 3.20: Phosphate sensor based ELM testing. A) RFP output from the microplate reading of the phoA-sensor based ELMs, under a range of 5 concentrations. B) Red pigmentation in terms of a* channel of the phoA-sensor based ELMs, under a range of 5 concentrations. A-B) Bars refer a biological duplicate, and error bars are the standard deviation.

Ongoing experiments are aimed at testing this sensor in soil, taking into consideration ranges of physiological phosphates and considering the possible interference based on the presence of nitrates, as emerged in the tests in liquid. This work certainly has limitations, and other experiments will be necessary to conclude the characterization of these last sensors. In addition, considering that the regulation of phoA is based on repression, some extra

considerations must be taken, as in a real scenario it is counter intuitive for the sensor to turn off at high concentrations. In repressor-based circuits, a NOT gate is often used to change the logic. A NOT gate can receive the repressor-based signal and invert the output, allowing for easy sensor readout in field applications. This could be a future modification to consider for our case study, in addition to the precise study of the concentrations that we can detect with the material, increasing the range between 100 μM and 500 μM. Another possible intervention is to prevent RFP accumulation via fast-degradation tag, which will inevitably decrease sensitivity in fluorescence detection, but the phoA promoter is strong enough to provide a detectable signal without issues.

3.3 Safe use of ELM sensor for field applications

As discussed earlier (1.4), the implementation of effective and robust biocontainment strategies is of great importance, especially in the rapidly evolving field of synthetic biology. As the capabilities of genetic engineering and synthetic biology expand, so do the potential risks associated with the unintended release of GMOs into natural environments. These risks are multifaceted and include the potential disruption of local ecosystems, the unintended horizontal gene transfer to native species, and the emergence of new, possibly harmful, pathogens. Such risks underscore the need for biocontainment solutions that are not only technically sound but also reflect an ethical responsibility to safeguard both the environment and public health.

In response to these concerns, a physical biocontainment system is proposed, utilizing a polydimethylsiloxane (PDMS)-based box that is sealed with a polyethersulfone (PES) filter membrane. PES is a versatile membrane usually adopted in applications such as sample preparation and sterile filtrations, since it retains fine particles, bacteria, fungus in aqueous filtrations.

Our system is conceived to prevent the escape of GMOs, while still allowing for the functionality of biosensors within the contained environment. The subsequent sections present detailed results regarding the effectiveness of this physical containment system, specifically in terms of its ability to prevent the escape of microorganisms into the surrounding media, as well as the performance of the biosensor when encased within the box.

3.3.1 Biocontainment strategy and escapers investigation

Initially, a preliminary biocontainment strategy was explored, involving the use of a 0.2 μm PES membrane filter to cover the ELMs as an envelope. This setup is illustrated in Figure 3.21 A. The first phase of experimentation focused on testing the functionality of this biocontainment approach by placing the wrapped ELM on a selective LB agar medium, chosen specifically to prevent external contamination and ensure any bacterial growth could be attributed solely to the organisms contained within the membrane. The purpose of this test was twofold: to verify the diffusion of inducers through the membrane and to assess the viability of the bacteria encapsulated within the ELMs.

The successful diffusion of inducers into the LB agar was confirmed by the production of RFP upon induction of the VAI system, demonstrating that the inducers had permeated the membrane and triggered the expected biological response. Additionally, the viability of the bacteria was confirmed through this RFP production. Importantly, no bacterial colonies were observed growing underneath the PES membrane filter, as anticipated, further validating the containment strategy at this stage.

Following these initial tests on solid media, the next step was to investigate the potential for bacterial escapers in a liquid medium. For these experiments, the ELMs were wrapped in either a single layer (N = 3) or double layers (N = 3) of the PES membrane. The results indicated that the PES membrane was effective in reducing the number of escapers from approximately 10^9 CFU/ml to 10^5 CFU/ml. However, it was noted that this result could potentially be improved with greater attention to the sealing process during the experimental setup (Figure 3.21, C - PES).

Specifically, the use of a thermo-welding machine posed challenges, such as misalignments of the filter strips and the inadvertent creation of microcracks, which may have allowed some bacteria to escape. While these results were promising, it was observed that one of the three replicates using the double-layer PES membrane achieved complete containment, with zero colonies detected. Nevertheless, the manual nature of the sealing process introduced inconsistencies, leading us to conclude that this particular approach was not sufficiently robust for reliable biocontainment. Consequently, we opted to explore an alternative design for the biocontainment system.

We designed a box to contain the ELM biosensor, with the additional flexibility to accommodate a piece of agar medium if required. This box was constructed from PDMS, a transparent material, which allowed for visual monitoring of the biosensor's response (Figure 3.21, B). The exposed face of the PDMS box was sealed using the PES filter membrane, which was

further framed and secured with PDMS glued to ensure a tight seal. The effectiveness of this containment strategy was evaluated using a CFUs assay. The results demonstrated that no colonies were detected for the biocontained ELMs condition, indicating that the physical containment system, combining PDMS and PES, successfully prevented the escape of any bacteria (Figure 3.21, C). This outcome not only confirmed the effectiveness of this biocontainment design but also demonstrated its versatility, as the system can function effectively both in solid-like environments and when fully immersed in liquid.

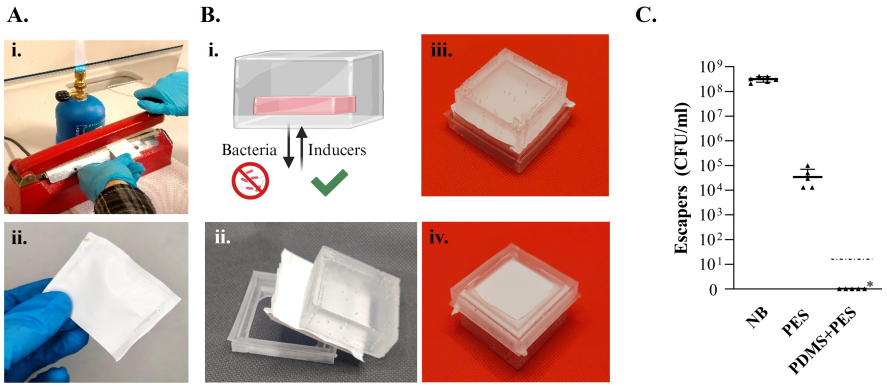

Figure 3.21: Biocontainment strategy through PDMS coupled with PES filter-membrane. A) Our first tentative of biocontainment, using the PES filter to wrap the ELMs. i) ELMs are covered and sealed in the filter. ii) Image of what the ELM biocontained in the PES looks like. B) The PDMS-based box proposed as physical containment. i) Graphic of how the biocontainment was conceived, capable of diffusing the molecules of interest (e.g., inducers, nutrients), but not releasing bacteria. Above the transparent PDMS box, inside the ELM on a layer of PES sealed to the box. ii) The PDMS box, the PES filter and another PDMS component that frames the filter from underneath and seals it to the rest of the container. iii) Top view. iv) Back view. C) Escapers in terms of CFU/ml, comparing the conditions no biocontained (NB), wrapped in the PES, contained in the box (PDMS + PES). Triangles refer to the 5 biological replicates, the thick line is the mean and the error bars are the standard deviation. The dotted line at 10^1 refers to the limit of detection, as 100 ul were plated for the CFU assay.

In addition to the PDMS-PES biocontainment system, we also evaluated a biocontainment strategy based on a pre-characterized PCD device. This PCD system was originally developed and characterized in previous work by our lab [122] with the primary goal of enabling controlled protein release. However, in this context, the PCD device was repurposed to assess its self-destruction potential, due to the enrichment of bacterial cells that escaped the

inducible lysis, and we directly compared its performance against the PDMS-PES containment system described earlier. Given the high mutation rates observed in the PCD device when used in LB medium, we opted to conduct these experiments in selective tap water instead. This medium was chosen due to its lack of nutrients, which would prevent the bacteria from replicating as rapidly, thus minimizing the likelihood of escape due to mutations. The experiments were carried out in two conditions: with and without the VAI inducer, which triggers cell lysis in the PCD system.

As anticipated, the number of bacterial escapers observed in tap water was significantly lower compared to the results obtained in LB medium. This was expected because the absence of nutrients in tap water prevents the bacteria from replicating as efficiently as they would in a nutrient-rich environment like LB (Figure 3.22). Furthermore, the addition of VAI, which activates the PCD mechanism and induces cell lysis, resulted in a reduction in escapers to 10^6 CFU/ml. This represents a 10 fold reduction in escapers compared to the condition without VAI, where the PCD mechanism was not triggered. Moreover, the PCD system with VAI exhibited more than a 100 fold reduction in escapers when compared to the uncontained bacteria in LB medium.

However, despite these improvements, the number of escapers in the VAI-induced PCD condition, while reduced, remained substantial. Although the reduction in CFU/ml was noteworthy, this still did not meet the stringent requirements for an optimal biocontainment strategy. As such, while the PCD-based system demonstrated some effectiveness in limiting bacterial escape, its performance was not sufficient to be considered a reliable standalone solution for biocontainment in synthetic biology applications.

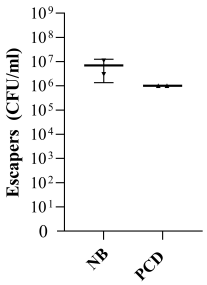

Figure 3.22: PCD mechanism tested as biocontainment for living material in tap water. ELMs were tested in water with or without VAI, PCD (100 nM) and NB respectively. Triangles refer to the biological duplicate, the thick line is the mean and the error bars are the standard deviation. The NB condition in tap water is more 10x lower than the NB in LB, due to the lacking of nutrients.

Overall, the data presented clearly demonstrate that the physical PDMS-PES containment box we developed is highly effective in preventing any escape of GMOs. In contrast, the previously developed PCD system, although exhibiting some degree of control over bacterial escape, does not provide a sufficiently robust biocontainment solution. The physical box successfully ensures total containment, whereas the PCD system, despite its self-destruction mechanism, still allows for a notable number of escapers, making it unsuitable as a reliable biocontainment strategy. This highlights the efficiency of our physical containment approach for applications requiring strict GMO control.

3.3.2 Low cost laser-based readout

The development of accessible, easy to use, and cost-effective methods for reading the output of biosensors is essential for broadening both the accessibility and the potential for innovation in biosensing technologies. This is especially important for applications that are intended for use in field settings. Traditional fluorescence detection instruments, while effective, tend to be prohibitively expensive, often large in size, and typically require expert supervision to operate. These limitations make such systems impractical for use in resource-constrained environments. Recognizing this, significant research efforts have been directed towards integrating fluorescence-based assays into smaller, more portable platforms, such as paper-based devices, hydrogels, and microfluidic systems. In tandem, these assays are paired with portable and easily accessible readout tools, like smartphone cameras or compact optical sensors. The primary goal of these innovations is to facilitate point-of-care diagnostics by offering user-friendly solutions that bypass the need for bulky, expensive laboratory equipment.

As outlined in Chapter 2, two main methods were explored for detecting the RFP used throughout this study. The first strategy involves using a microplate reader, either by cutting a sample from the ELM and placing it in 96-microplates, or by analyzing entire patches in larger wells. The second method is less equipment-dependent: it involves taking a picture of the RFP-emitting patch when it becomes visible to the naked eye. This image is then analyzed by focusing on the red a* channel component in the CIELAB color space. However, this latter approach presents significant limitations. It fails to provide any information when the RFP signal is too weak to be seen with the naked eye, a frequent occurrence when using natural non-engineered promoters, which tend to produce weak signals. Furthermore, even with model sensors, low concentrations of RFP result in insufficient red fluorescence, making the a* channel image analysis method nearly ineffective. To address

these challenges, we hypothesized that even a minimal level of laser excitation might improve detection at lower RFP concentrations without the need for a microplate reader. To test this, we used a green laser pointer in conjunction with a smartphone camera to capture the fluorescence response of the biosensor-embedded ELMs while they remained contained within a PDMS (polydimethylsiloxane) enclosure. Additionally, we applied a red filter to the smartphone camera, which allowed us to block out the green laser's excitation light, ensuring that only the emitted fluorescence (at a longer wavelength) was captured.

We conducted experiments where pictures of the sensing ELMs, induced with three different concentrations of VAI, were taken in a darkroom setting using the green laser pointer. The resulting images were analyzed based on two key parameters in the CIELAB color space: the L* channel and the a* channel (referred to as the a* channel laser when laser excitation was used). Since it was unclear which CIELAB component would be most appropriate for this task, we measured and analyzed both channels. Additionally, images of the ELMs taken under controlled ambient lighting conditions were also collected, focusing specifically on the a* channel (Fig. 3.23, A), in order to investigate any potential correlation between the two methods.

The results revealed a strong correlation between the a* channel values obtained from standard ambient light images and those from the laser-excited images of the biocontained ELMs ($R^2 = 0.998$). Furthermore, when comparing the a* channel from the non-laser images with the L* channel from the laser-excited images of the biocontained ELMs, we observed another high correlation ($R^2 = 0.980$). These findings confirm the reliability of using the laser-assisted procedure. In fact, the data from the L* channel were consistent with the a* channel values typically observed without laser excitation. However, the a* channel values obtained using the new laser procedure were higher, prompting us to prioritize this method moving forward.

We also evaluated the potential influence of the PDMS biocontainment on the RFP detection results. For both the L* and a* channels, a degree of attenuation in fluorescence was observed across all inducer concentrations when the ELMs were analyzed in their biocontained box. Nonetheless, the dose-response trend remained intact, as shown in Fig. 3.23 C-D (green vs. pink bars). These findings support the conclusion that this approach, i.e., using a green laser pointer and a smartphone camera in conjunction with a red filter, all within a darkroom setting, could serve as a practical, portable, and accessible method for users to read biosensor responses directly, without the need for laboratory-grade equipment or any complex preprocessing steps.

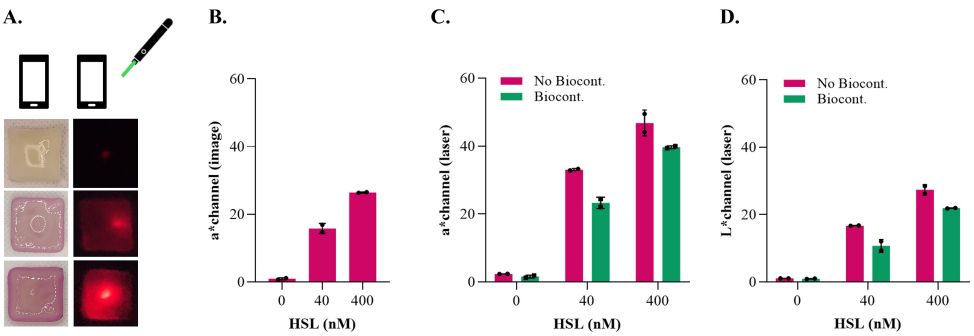

Figure 3.23: Green laser pointer for a low cost RFP readout. A) Example of pictures of ELMs at 0, 40, 400 nM of VAI. The first column is processed for the a* channel to extract the red component. The second column is obtained using the green laser and a red filter in the darkroom, and processed to obtain L* and a* channels. B) The red pigmentation represented in terms of a* channel of the pictures taken under light controlled condition. C) The red pigmentation represented in terms of a* channel of the pictures taken in the darkroom, using the green laser. B-C-D) Bars are the mean of a biological duplicate, black points represent each value, and the error bars refer to the standard deviation.

Next, we aimed to further characterize the dose-response behavior of the model biosensor by employing all three readout methods to verify their sensitivity. The first method, which involves analyzing the a* channel of the images, provided a quantification of red fluorescence for the higher concentrations tested (0.1, 0.2, and 400 nM). However, this method was unable to differentiate the lower concentrations effectively (Fig. 3.24 A). The response measured using the microplate reader, presented at an average gain level, was consistent with the a* channel measurements from the standard image analysis (Fig. 3.24 C).

Surprisingly, the third method, which utilized the green laser pointer to excite the patch, yielded a superior dose-response curve compared to the other two methods (Fig. 3.24, B). Notably, it revealed a LOD at 0.02 nM of VAI, highlighting its enhanced sensitivity. Intuitively, the a* channel data obtained using the laser excitation mode proved to be more effective than the images taken under ambient light conditions. This improvement is likely due to the dark-field illumination provided by the laser, which enhances the excitation of RFP that is not visible to the naked eye. What is particularly noteworthy is that this laser-based approach not only performs well but may even surpass the microplate reader in terms of the LOD. One possible explanation for this is that the laser-assisted image captures the fluorescence signal from the entire patch of ELM, whereas the microplate reader only analyzes a small portion of the material, which can vary in size depending on

the experiment or the user's handling.

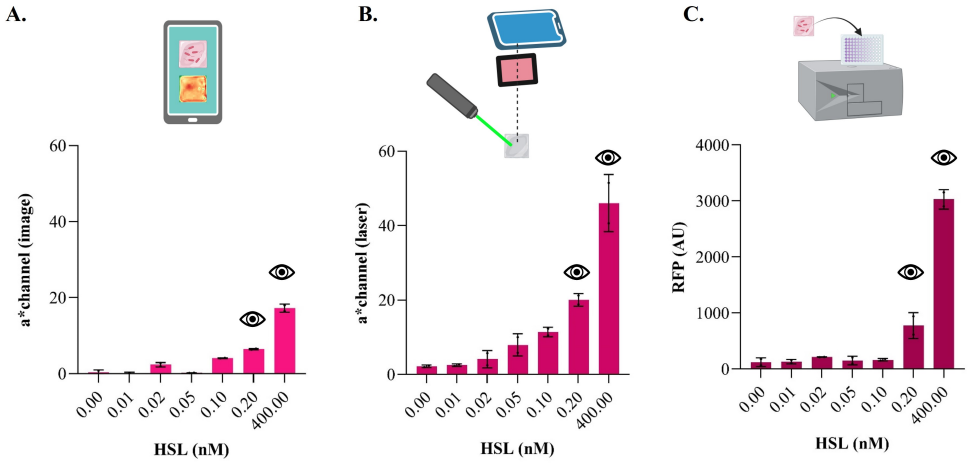

Figure 3.24: Comparison of three different VAI-sensing ELM readouts, ranging the concentration of VAI up to 400 nM. A) a*channel readout analyzed from the picture of the ELMs. B) a*channel readout analyzed from the picture of the ELMs, using the green pointer laser and the red filter in a darkroom. C) Response of the VAI-sensing based ELMs trhough the microplate reader. A-B-C) Bars are the mean of a biological duplicate, black points represent each value, and the error bars refer to the standard deviation. The eye icon means that the RFP was visibile at naked eye.

Interestingly, other studies have demonstrated similar sensitivity and performance using smartphone-based detection systems paired with low-cost, battery-powered lasers. For instance, Ning et al. reported that their prototype smartphone-based device, designed to detect SARS-CoV-2, achieved sensitivity comparable to that of a microplate reader [123]. This was accomplished using a 100 mW laser diode, powered by AAA batteries, to illuminate the assay chip at a low angle, which greatly improved detection sensitivity . Another study by Li et al. [124] utilized a smartphone in combination with a portable blue laser diode to detect four toxic cyanotoxins at low nanomolar levels (1-3 nM). This platform exhibited excellent chemical specificity and performed robustly, even in the presence of interfering substances such as other cyanotoxins.

Although fluorescence-based detection methods remain the gold standard in biosensing due to their high accuracy and reliability, affordability is a critical consideration, particularly for applications in resource-limited settings. Given this need, the results of our experiments suggest that smartphone cameras equipped with today's megapixel resolution camera, often rivaling

high-end photography equipment, coupled with a simple laser pointer, could offer an accurate, low-cost detection method that can be deployed directly in the field.

This approach provides a promising alternative for making biosensing technologies more accessible without compromising on sensitivity or performance.

3.4 Final considerations

In Chapter 2, the bacterial bioprinting workflow was introduced to streamline the use of biosensor based living materials for clinical diagnostic applications. Here, this approach has evolved into a technology for creating devices specifically designed for agro-industrial purposes.

The results shown in this part of the thesis represent the characterization of 11 sensors of molecules of interest such as VOCs, acetate, nitrates and phosphates. Investigations in liquid assays to fully understand the functioning of the biosensors were conducted, appropriately tuning some important parameters depending on the biosensor taken in consideration. Some of these results led to the exclusion of biosensors from the subsequent steps as they were not suitable for the task or did not work in the conditions tested; others highlighted important factors for our work but also for future research. These include the strong influence of pH in glnAP2 promoter when tested with acetic acid and in phoA promoter tested with phosphates, as well as the crosstalk between nitrates and phosphates for both the yeaR and phoA promoters. The devices showed in the last part might represent a great promise for improving agricultural management, allowing farmers to adopt targeted and sustainable fertilization strategies, or they could be useful for industrial process optimization, enabling more precise control of digestion processes and overall improvement of the plant performance. Regarding the ELMs, an optimization phase was required to make the various sensors work, and a new nutrient media was efficiently adopted for the printing purpose. However, ongoing experiments are aimed to wrap up the final characterization of ELM sensors for soil monitoring, including real soil samples, both clay and sandy with known concentration of nitrates (in terms of N-NO_3) or posphates (in terms of P-PO_4). On the other hand, the sensor based on the glnAP2 promoter proved capable of detecting industrially relevant concentrations in digestate samples from biogas plants.

A physical biocontainment strategy was successfully tested showing no bacterial escapers in the surrounding medium. The strategy based on a PDMS-box, sealed with a PES filter membrane resulted in an optimal solu-

tion to avoid GMOs escape, surpassing the containment proposed exploiting a PCD mechanism. In addition, we proposed a straigthforward method for analyzing the output of the ELM biosensors, while still contained in the PDMS-box. Using a smartphone camera and a green laser pointer we obtained promising sensitivity results for reading ELMs directly in the field, with low-equipment scenarios.

Overall, this part of the work taken together with what found from the Chapter 2 pointed out three essential points. First, ELMs technology is truly generalizable, it can be used for the most disparate applications, and it can be customized in different ways considering its levels of tuning. Second, it is noteworthy that moving from model sensors to natural promoters, often not well known, means significantly increasing efforts into the characterization, both in liquid and once printed. This might be caused by the complexity of the metabolic network and the intertwined pathways, but also because natural promoters often result into modest transcriptional strenghts and this clearly represent a limiting step when facing real-world challenges with very low physiological ranges. Another crucial factor is represented by the several challenges arise from the use of real samples. Fors instance, as seen in this work, biosensors are sensitive to environmental conditions such as temperature, pH, and nutrient availability. Maintaining their stability and functionality over time, especially in uncontrolled real-world conditions, is difficult. In addition, real-world samples, in this case soil or digestate, but also other types such as blood, or wastewater, often contain complex mixtures of substances that can interfere with the living material or the signal output of the biosensor. Moreover, cross-reactivity, noise or interference can lead to inaccurate measurements, and it has to be taken into account. Therefore, addressing these challenges requires careful design and biosensors calibration against real-world samples. Finally, comparing ELM based technology for biosensing purposes with cell-free tools, ELMs offer several key advantages. First, they are less affected by matrix-related inhibitions, which can often pose challenges in cell-free systems, which require extensive preparation of the sample before use. Additionally, ELMs can readily utilize promoters regulated by complex pathways or membrane proteins allowing for more intricate and responsive biosensing capabilities. Moreover, achieving similar functionality through cell-free translation would be extremely challenging, further emphasizing the versatility and potential of ELM based systems in biosensing applications.

However, the potential of these biosensing ELMs can only be fully achieved through efforts to increase their sensitivity and the material lifespan, developing strategies to withstand lack of nutrients and improve resilience to harsh environments.

Chapter 4

A cyanobacteria based platform for carbon negative biomanufacturing

This Chapter concerns the work done during the visiting internship at the Wyss Institute for Biologically Inspired Engineering, in the Church lab. A novel S-layer protein in *Synechococcus elongatus* UTEX 2973 (further referred to as UTEX 2973), is proposed as a tool for biomanufacturing, and its capabilities of surface display and protein secretion are described. First, the characterizion of the SLP platform is discussed along with its functionality, testing different proteins and enzymes. Next, a cyano-based workflow to realize bricks with particular focus on carbon fixation and biomineralization is proposed using sodium alginate, gelatin and sand. Cell viability and mechanical properties were characterized for the wild type strain UTEX 2973 within the material. Then, genetic engineering was carried out for the creation of a carbonic anhydrase library, with the aim of increasing the hydration of CO_2 for carbon capture, therefore maximizing the production of calcium carbonate within the living materials. Finally, engineered versions using proteins derived from tardigrades were investigated in terms of survival after desiccation conditions.

4.1 A novel S-layer protein in cyanobacteria

4.1.1 S-layer protein characterization

In an initial bioinformatic screening, we identified three putative candidates with structural features similar to known SLPs in UTEX 2973 (Appendix B). These candidates were subsequently analyzed to determine the

most suitable SLP for use in a secretion and display platform (Fig. 4.1, A). To facilitate detection, each protein was tagged with the 11 amino acid HiBiT epitope, which produces a luminescent signal when it binds to its partner LgBiT [125]. The screening was conducted by evaluating both surface display potential, in which the HiBiT tag was inserted in the middle of each candidate protein, and secretion potential, which was assessed using an N-terminal truncated version tagged before the C-terminal. This approach was based on the known localization of the domains responsible for anchoring (N-terminal) and secretion (C-terminal).

To ensure consistency and simplify the experimental setup, we used the promoter of the first candidate (Uniprot primary accession: Q31NQ2) to drive transcription of all constructs, as the promoters of the other two candidates were not well-characterized. The experimental results revealed that only the first protein displayed a strong luminescent signal on the cell surface (Fig. 4.1, B), indicating efficient surface display. Additionally, this protein demonstrated the highest level of secretion (Fig. 4.1, C).

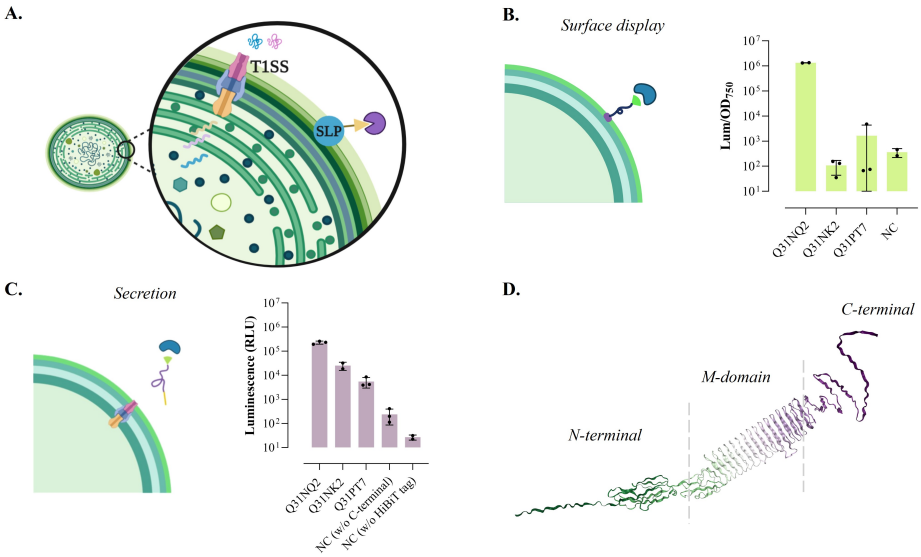

Figure 4.1: SLP screening. A) The screening was performed to select the best SLP candidate to be secreted through the T1SS and to display proteins or enzymes of interest leveraging a small bioluminscent tag. B-C) In order to choose the best S-layer protein for our we screened three putative SLPs both for surface display (B) and secretion (C), comparing their output in terms of luminescence. Bars are the mean of a biological triplicate, black points represent each value, error bars standard deviation. D) The first SLP candidate, VCBS protein, shown among its three domains (e.g., N-terminal, middle domain, and C-terminal).

For the surface display assay, a negative control was included, consisting of a construct containing the first SLP candidate, but without the HiBiT tag. This control was crucial for distinguishing genuine signal from potential system leakage. In the secretion assay, another negative control wass employed: a plasmid encoding the N-terminal truncated version of the first SLP candidate, tagged with HiBiT but further truncated before the C-terminal, thus lacking the SP required for secretion.

Based on these findings, we selected the first candidate, a protein composed of 610 amino acids and referred to as VCBS, for further characterization as our SLP (Fig. 4.1, D).

Gene knockouts are a common method for understanding gene function and creating a controlled environment for genetic engineering without interference from native gene activity. To this end, we knocked out the gene encoding VCBS using homologous recombination and segregation. The success of the knockout was confirmed by colony PCR, with the absence of the target amplicon indicating the removal of the SLP gene. We tested two colonies and observed the complete absence of the expected PCR product.

Transmission electron microscopy (TEM) was performed on cells from both the wild-type UTEX 2973 strain and the △slp knockout strain. In the wild-type cells, the outer membrane appeared intact, continuous, and of uniform thickness (Fig. 4.2, A), with the cell envelope exhibiting a well-organized structure. In contrast, the SLP knockout cells displayed irregularities in the outer membrane (Fig. 4.2, B). These irregularities included sections of the membrane that appeared less smooth and areas with inconsistent thickness, leading to a less defined overall cell shape.

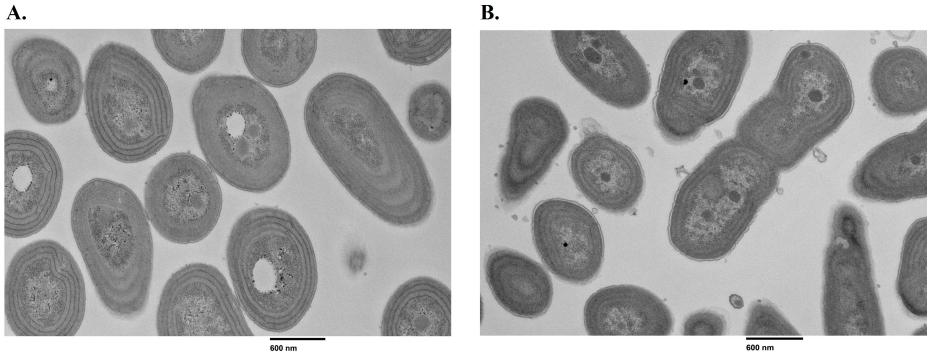

Figure 4.2: Comparison of TEM images between wild type and △slp cyanobacteria. TEM images of fixed cells on grown strains of UTEX 2973 WT (A), and the △slp engineered strain (B).

These data suggest that the knockout of the SLP gene compromises the

structural integrity of the cell, resulting in deformed or irregular cell shapes due to the absence of the ordered lattice typically formed by SLPs. However, contrary to expectations, we did not observe a reduction in the number of membrane layers between the wild-type and knockout strains, which would have been expected with the removal of the S-layer.

4.1.2 Design and testing of a surface display and protein secretion platform

SLP engineering

Using AlphaFold predictions of the SLP structure, we sought to identify the minimal SP sequence required for efficient secretion. To experimentally evaluate this, we tagged the protein with HiBiT at different positions, progressively moving closer to the C-terminal with smaller truncations.

In Type 1 Secretion Systems (T1SS), such as the alpha-hemolysin (HylA) secretion system in *E. coli*, secretion is typically initiated through the recognition of a SP located within the last 50-70 amino acids of the protein's C-terminal region [126, 127]. In our investigation, however, we found that efficient secretion, evidenced by robust luminescent signals generated from the HiBiT tag in the supernatant, required a significantly longer C-terminal sequence, extending beyond 150 amino acids (as demonstrated in Fig. 4.3 A, specifically at the 208th amino acid). In contrast, when the secretion was targeted to only the last 100 amino acids, the resulting signal was notably weak, indicating insufficient secretion.

The discrepancy in the length of the C-terminal region required for effective secretion could be due to structural differences in the secondary conformations of the protein or distinct requirements posed by various bacterial hosts. Despite this variability, a hallmark of RTX proteins is the presence of multiple tandemly repeated nonapeptide motifs, generally situated in the C-terminal region. These repeats are responsible for forming calcium binding sites and adhere to a consensus sequence '1GGXGXDXUX9', where X represents any amino acid, and U denotes a hydrophobic residue such as leucine (L), valine (V), isoleucine (I), phenylalanine (F), or tyrosine (Y). In the C-terminal region of our SLP, these nonapeptide repeats are organized into 10 consecutive tandem repeats (as shown in Table 4.1).

The C-terminal of our SLP is preceded by 10 nonapeptide tandem repeats as reported in Table 4.1.

AA position	RTX motif
242	GG D G N D T I I
278	GG A G A D T I L
287	GG D G A D T I D
296	GG L G N D S I F
323	GG S G N D T I E
360	GG L G N D S I L
377	GG D G S D T I N
395	GG M G N D S I E
457	GG T G A D T L T
466	GG L G S D T F S

Table 4.1: RTX motifs preceding the C-terminal of the SLP protein. The typical consensus sequence 'GGXGXDXUX' is repeated in the SLP, starting from the 242th to the 466th AA, for a total of 10 motifs.

The primary role of the RTX domains appears to be acting as internal chaperones, maintaining the polypeptide in an unfolded state within the calcium-depleted cytosol and facilitating its folding in the calcium-rich extracellular environment [128]. In our experiments, the C-terminal region with all 10 RTX repeats achieved the highest level of secretion (Fig. 4.3, A 460th AA). Interestingly, secretion still occurred without the repeats, consistent with findings by Letoffe et al. [129], who demonstrated that RTX repeats are not involved in T1SS recognition in *E. coli* but are important for secreting large proteins.

Therefore, we selected the final 150 amino acids of the C-terminal region as the SP for designing all constructs aimed at protein secretion.

To optimize transcription, we sought to test the HiBiT-tagged C-terminal using different promoters, comparing the native SLP promoter to characterized ones. In particular, a strong constitutive promoter from the C-phycocyanin operon (Pcp560), medium and low strength based on the modified BioBricks BBa J23119 library of promoters (PJ23107 and PJ23119-v04) were used [130]. All the promoters enhanced secretion levels of the HiBiT tag in the supernatant (Fig. 4.3, B).

To characterize the display capability, we HiBiT tagged 7 locations throughout the SLP (Fig. 4.3, C). A strong luminescent signal was observed in all the positions, except for the tag placed in the 483rd residue, demostrating the homogeneity of the surface (Fig. 4.3, C). According to the predicted protein structure, the 483th residue corresponds to a potential loop conformation and placing HiBiT in a tight loop may reduce signal intensity. Furthermore, to ensure there was no signal in the extracellular environment, we also analyzed

the supernatant of one of the constructs that reported values similar to the negative control confirming no secretion leakiness (data no shown).

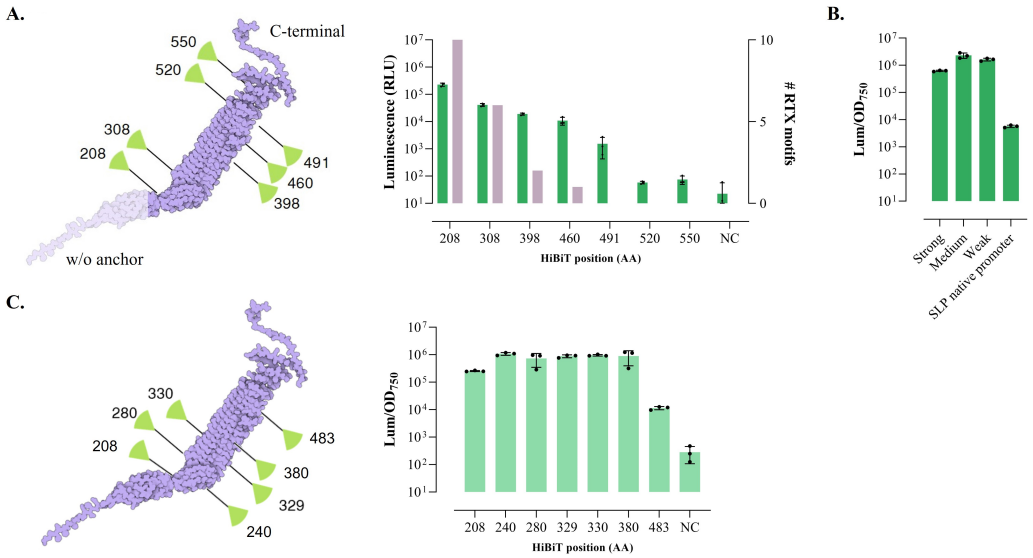

Figure 4.3: Preliminary data of the SLP platform. A) Our SLP, without N-terminal, tagged in different locations resulting in seven trucated versions. The green bars refer to the secretion level for each truncation, and the lilac bars are the number of RTX motifs preceding the C-termianal of each version. B) Comparison of secretion using different promoters. The luminescence detected in the supernatant is normalized by the cell density. C) Detection of HiBiT, in the surface of the cell, inserted across the middle domain. A-B-C) Bars are the mean of a biological triplicate, black points are the single values and errors bars refer to the standard deviation.

Surface display and secretion of heterologous proteins

To assess the potential of our platform for surface display of various heterologous proteins, we replaced the central region (amino acids 208-460) of the native system with two distinct foreign proteins. As a result, we observed a robust luminescent signal for both proteins (Figure 4.4, A), indicating successful surface display. The first protein we utilized was a tardigrade-specific intrinsically disordered protein (TDP), while the second was an elastin-like polypeptide (ELP_{60}). The decision to display these two particular proteins was based on their potential to enhance ELMs, as discussed in Chapter 2. TDP is known to confer desiccation tolerance, making it particularly useful for protecting cells under extreme environmental conditions. In contrast, ELP polypeptide can serve as a structural support material, contributing to the overall architecture of ELMs.

To further evaluate our platform's capacity for protein secretion, we tested a range of relevant proteins across various fields, including material science and therapeutics (Figure 4.4, B). For every target we included a negative control in which the C-terminal was removed from the protein or enzyme, preventing secretion. Strong luminescent signals were detected for TDP, ELP_{60}, and two widely studied enzymes: a bacterial laccase (EcCueO) from *E. coli*, which plays a significant role in bioremediation efforts [26], and a beta-lactamase (BcBla).

To test the platform with a complex target, we attempted to secrete four silk proteins, previously optimized. Silk proteins have garnered attention for their potential in the biomedical scenario, as well as for agri-food applications [131]. However, it also raises considerations that need to be carefully addressed, such as meeting industry standards retaining the properties of natural silk. Silk proteins have complex repetitive structures that contribute to their unique properties, and achieving proper protein folding and assembly can be challenging. Our data showed a lower luminescence level for these proteins, although for ELP_{60} (a similar recombinant protein) there were no secretion issues. Connor et al. found that the recombinant silk proteins, but not the elastin-like peptide, exert toxicity on the *E. coli* host system, possibly through their high degree of intrinsic disorder, which might represent the same issue in *S. elongatus* [132].

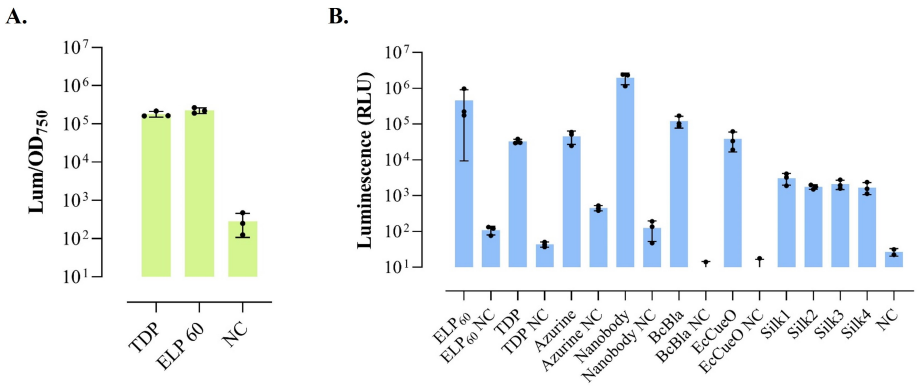

Figure 4.4: Display and secretion of different relevant proteins. A) Our SLP used to secrete TDP and ELP_{60} reported a strong luminescent signal on the surface. B) Different proteins and enzymes, among their negative controls, secreted in the supernatant. A-B) Bars refer to the mean of a biological triplicate, black points are the single values and errors bars represent the standard deviation.

In addition to our material science applications, we also reported two potential therapeutic targets successfully secreted. The first was azurine, an

anticancer biologic drug derived from *P. aeruginosa*, which has been previously reported for biologics release in living materials [133]. The second was the JN241-9 nanobody, determined to be a potent full agonist against the human apelin receptor, a promising target for therapies to treat patients with chronic heart failure [134].

Although T1SS systems are well-characterized for their ability to secrete a broad range of proteins, spanning a size spectrum from under 10 kDa to over 1 MDa [135], their functionality in cyanobacteria remains less extensively explored. In our experiments, we observed significant variability in secretion levels across different proteins, suggesting that multiple factors influence the efficiency of this system. One of the key factors is the choice of the minimal SP, which contains the fewest RTX motifs. The RTX motifs play a crucial role in the secretion process [136], and studies have demonstrated that increasing the number of these motifs can enhance secretion efficiency for certain heterologous proteins [137, 138, 139]. This suggests that optimizing the number of RTX units might be a critical factor in maximizing secretion efficiency in cyanobacteria as well.

In addition to the structural aspects of the secretion peptide, another important consideration is the intrinsic properties of the heterologous proteins themselves. Factors such as the overall charge and isoelectric point of the protein can significantly impact its compatibility with the secretion machinery, potentially influencing the efficiency of secretion. Previous studies have indicated that proteins with unfavorable charges or pI may interact less efficiently with the T1SS [140], leading to lower secretion levels. Thus, tailoring the properties of the protein, either through engineering or selection of compatible candidates, could further enhance the overall performance of the system.

Despite the simplicity and appeal of T1SS as a one-step secretion mechanism, it has inherent limitations, particularly in terms of yield. For example, the highest reported titer achieved using T1SS for an anti-transmissible gastroenteritis virus single-chain fragment was only 1-2 mg/L, with most other reported yields falling within the micrograms per liter range [137]. This relatively low production yield poses a significant challenge for the widespread use of T1SS in industrial applications. However, there is potential to overcome this limitation through genetic engineering of the T1SS components. For instance, overexpression of TolC, a key outer membrane protein responsible for facilitating the final step of protein export into the extracellular space, has been shown to improve secretion efficiency [141]. By enhancing the abundance or activity of such critical components, it may be possible to significantly increase protein yields.

One notable characteristic of the T1SS mechanism is that the C-terminal

sequence of the protein remains intact after translocation, which may pose a challenge when a purified product is required, as is often the case in pharmaceutical applications. In such cases, post-secretion processing becomes necessary to remove the C-terminal tag. One potential solution to this problem is to incorporate a protease cleavage site before the C-terminal sequence. This strategy allows for protease-mediated removal of the tag after secretion. To streamline the process further, the membrane can be engineered to include a protease, enabling in situ processing of the protein once it is secreted into the extracellular space. This modification would allow for the production of proteins with a clean, tag-free C-terminus, which is often desirable for downstream applications.

Finally, while our platform has demonstrated considerable potential in facilitating protein secretion, further research is needed to ensure that the secreted proteins retain their functionality. The detection of the HiBiT tag in the supernatant confirms secretion, but it does not guarantee that the secreted proteins are properly folded or biologically active. To address this, a HiBiT gel blotting experiment will be carry out to show if proteins are intact, since fragmented proteins might still give HiBiT signals. In addition, a more comprehensive investigation, including functional assays, will be necessary to fully assess the effectiveness of the secretion system in producing functional proteins in UTEX 2973. This will involve not only optimizing secretion efficiency but also ensuring that the secretion process does not compromise protein quality, which is crucial for both research and industrial applications.

4.2 Living material for carbon fixation and biocement production

4.2.1 Cyano-bricks prototyping

Workflow

Cyanobacteria-based bricks represent an exciting area of research within the field of ELMs. These bricks leverage the natural abilities of cyanobacteria to photosynthesize, fix carbon dioxide, and precipitate minerals, offering an environmentally sustainable approach to building material production. In our study, we developed a straightforward workflow for creating cyano-based bricks using UTEX 2973. The core components of our bricks included sand (a common fine aggregate in conventional concrete), gelatin (Gel), and sodium alginate (SA), which served as hydrogels for binding all the materials together (Figure 4.5 A). As with the ELMs developed in Chapter 2, calcium chloride ($CaCl_2$) was employed as a crosslinking agent to solidify the hydrogel matrix.

Different SA and Gel concentrations, sand particle size, as well as ratio of hydrogel:sand were tested (Fig. 4.5 B-C).

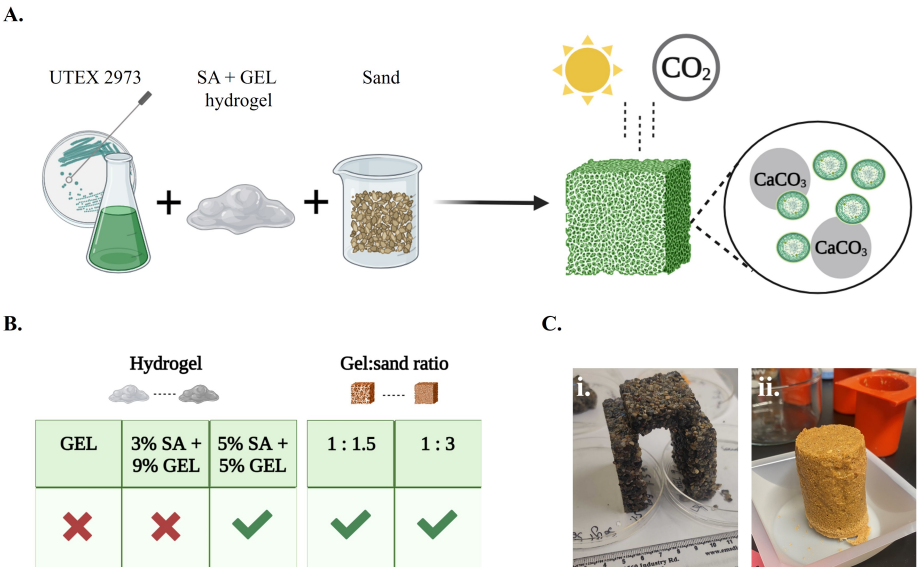

Figure 4.5: Cyanobacteria-based bricks workflow. A) The components used to realize cyanobacterial bio-bricks are shown. Cells, hydrogel, and sand are mixed to obtain a moisture, which is then poured in a mold. The living bricks convert light and carbon in calcium carbonate precipitation. B) Variable tuning before establish the current workflow. C) Bricks pictures showing two different sand types, i) used for the viability test, and ii) used for the mechanical test, due to specific requirements from the instrument.

Drawing inspiration from the work of Heveran et al. [71], we initially attempted to construct bricks using only gelatin. However, gelatin proved unsuitable as it is thermosensitive and melts at incubation temperature, restricting us to working in a refrigerated environment. To overcome this limitation, we incorporated sodium alginate into the hydrogel formulation. Through qualitative testing, we determined that a 5% concentration of both SA and Gel was optimal, as lower concentrations (e.g., 3% SA and 9% Gel) resulted in easily deformable materials.

The ratio of hydrogel to sand was selected based on literature recommendations, and adjustments were made as needed. Ratios of 1:1.5 and 1:3 both yielded materials with a brick-like structure. We experimented with different types and shapes of sand and conducted scanning electron microscopy (SEM) analyses of the bricks after one week of incubation. These analyses revealed the presence of viable cyanobacterial cells, suggesting that the type of sand used did not impede cell survival. This finding allowed us to generalize our

platform for potential use with various types of sand and in diverse applications. Based on these results, we moved forward with the material shown in Figure 4.5, C i) for cell viability tests. However, to perform mechanical testing, which requires specific specimen shapes, we opted to use the material depicted in Figure 4.5, C ii), as it was easier to extract from molds without breakage. This material was subsequently used for all mechanical testing.

Cell viability

We assessed the viability of UTEX 2973 cyanobacterial cells within the bricks over a 5-day period using the same protocol used for ELMs in Chapter 2, and described in Appendix A. In this case, a piece of the brick was weight and then dissolved in a sodium citrate solution to release the cells for counting. Two different hydrogel:sand ratios (1:1.5 and 1:3) were tested to determine if this factor impacted cell survival. The results showed that cell viability ranged between 10^7 and 10^8 CFU/g on day 0 (immediately after the bricks were formed), with a gradual decline over the 5-day observation period (Figure 4.6). No significant differences were observed between the two hydrogel:sand ratios, suggesting that both formulations are compatible with cell growth.

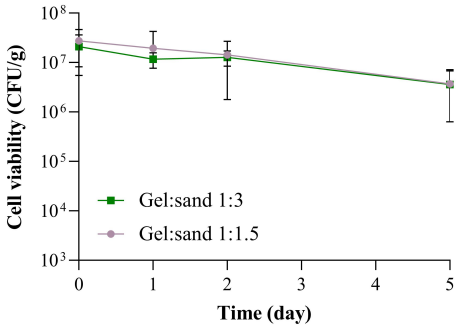

Figure 4.6: Cell viability of UTEX 2973 within the brick. Viability of bacteria included in hydrogel and sand based bricks was investigated in a time span of 5 days with 4 time point (day 0 refers to the day in which bricks were made). The green and lilac curves refers to differnt gel:sand ratio, as reported in the legend. Squares and circles are the mean of a triplicate, and the error bars represent the standand deviation.

It is important to note that the bricks were incubated without the addition of external solid nutrients; therefore, the nutrients supplied by the liquid BG11 medium included in the initial brick formulation were the only available source for cell metabolism. To extend the viability of the cells, a possible strategy would involve placing the bricks on BG11 agar plates and

transferring them to fresh medium as needed, as was done in previous studies referenced in Chapter 2.

One limitation of our current fabrication process is that the bricks are formed by mixing and pouring the components into molds, which does not allow for precise spatial control over the distribution of cells within the material. This lack of spatial organization could result in heterogeneity in both cell viability and gene expression. For example, cells located near the surface of the brick may have better access to light and oxygen, whereas those in the core may be deprived of these essential resources.

Mechanical properties

A preliminary test was conducted to monitor the mass of the living materials over time. This involved regular weighing of the samples to track how their mass changed as they dried out or released moisture. Over the course of a week, the material reached mass equilibrium, allowing us to proceed with the mechanical assessment (Fig. 4.7, A).

Both air-dried cyanobacteria-based bricks and abiotic control samples (i.e., without cells) were incubated for 7 days before their mechanical properties were evaluated. Since both hydrogel-to-sand ratios tested previously showed promising viability, we selected the ratio containing a higher proportion of sand for further analysis. For this evaluation, we performed a uniaxial compression test, complemented by scanning electron microscopy (SEM) and energy-dispersive X-ray spectroscopy (EDS) measurements.

From the compression test results, we observed that the abiotic control samples exhibited lower mechanical strength compared to the wild-type (WT) cyanobacteria-containing samples (Fig. 4.7, B). This was particularly evident in the significant difference in peak stress values (Fig. 4.7, C), with the WT samples reported an higher value ($p < 0.05$, t-test). These findings align with other studies, which have also demonstrated that the incorporation of cyanobacteria enhances the mechanical strength of biocomposite materials compared to abiotic controls [71, 72].

While a one-week incubation period was sufficient to produce dry and rigid materials, with the specimens cleanly breaking into two parts rather than crumbling (Fig. 4.7, D), the appearance of biomineralization deposits can vary based on factors such as the species of cyanobacteria used, environmental conditions (e.g., pH, temperature), and nutrient availability. In some cases, longer incubation times may be necessary to observe significant mineral formation. However, previous research has shown that the presence of mineralizing strains, such as ureolytic bacteria, can improve the mechanical properties of cementitious composites by inducing biomineralization [142]. This suggests that extended incubation periods or the inclusion of specific

strains might further enhance the mechanical strength of these bio-based materials.

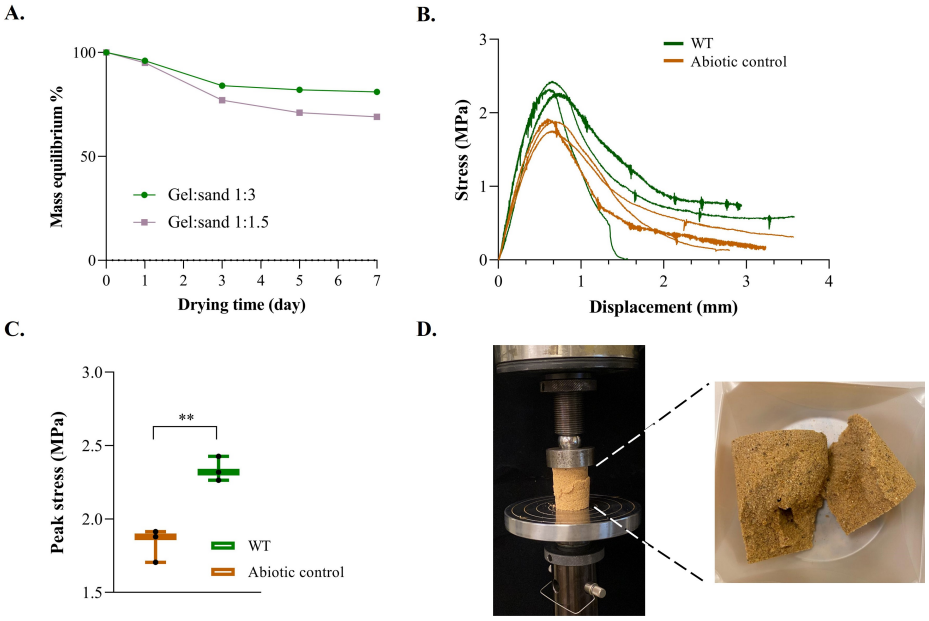

Figure 4.7: Mechanical properties. A) Mass equilibrium in terms of weight loss from day 0, is shown for both ratio hydrogel:sand. A time of a week is required to reach the drying condition. B) Uniaxial compression test was performed using three replicates for each condition (i.e, WT and abiotic control), and reported in the stress-displacement graph. C) The maximum peak stress is reported for each sample (black circle points), as well as the mean of the biological triplicate, shown with the max/min. D) Picture of the compression testing machine and one sample after the break.

In addition to the mechanical analysis, a comprehensive investigation into the mineralization process within the cyano-based bricks was conducted using SEM and EDS analysis. These advanced techniques were employed to examine and compare different sample sets, which included bricks containing bacterial cells with and without the addition of $NaHCO_3^-$ and $CaCl_2$ (required for the biomineralization process), and an abiotic control. These samples were systematically compared in terms of their surface morphology and chemical composition, providing insights into the role of biological and abiotic factors in the formation of minerals on the brick surfaces.

As expected, the presence of bacterial cells was confirmed in all the biological samples, whereas no cells were observed in the abiotic control group (Fig. 4.8). SEM analysis provided a detailed visualization of the surface

structure, while EDS data further revealed the presence of calcium peaks across both biological and abiotic samples, indicating the formation of calcium carbonate ($CaCO_3$). The detection of $CaCO_3$ even in the abiotic control was not unexpected, as this sample was prepared from a solution containing both $NaHCO_3^-$ and $CaCl_2$. This result aligns with findings reported in previous studies, where the chemical precursors used in the abiotic controls also resulted in calcium carbonate precipitation without biological mediation [72].

One critical point to highlight is the difference in the analytical scope between the mechanical tests and SEM analysis. While the uniaxial compression tests encompass the entire bulk of the sample, providing an overall assessment of the mechanical integrity of the bricks, SEM is a more localized technique, offering a detailed examination of specific areas on the sample's surface. This localized analysis might not fully represent the spatial distribution of minerals across the entire sample. In a related study by Obst et al., which focused on cyanobacterial biomineral nucleation and calcium hotspots, the sources of $CaCO_3$ formation were found to develop in close proximity to the outer membrane of cyanobacterial cells particularly near one of the poles of the rod-shaped cells [143]. These hotspots were external to the cells but spatially confined to specific regions. This suggests that in cyanobacteria, biomineralization may occur in highly controlled and localized sites. However, this precise localization of mineralization may not align well with the protocol used in this study, in which manual mixing was involved during sample preparation. Contrary to bioprinting, this manual mixing procedure does not offer fine spatial control over the distribution of bacterial cells within the matrix, potentially leading to a more dispersed or random distribution of mineralization.

It is also possible that with an extended incubation period, more pronounced differences in calcium peaks might emerge when comparing the abiotic control with the samples containing both bacterial cells and biomineralization enhancers. A longer incubation period could allow for more extensive mineral deposition, potentially highlighting differences between biologically mediated mineralization and the abiotic precipitation of calcium carbonate. This hypothesis warrants further exploration in future experiments.

Moreover, it is essential to consider various abiotic factors that can significantly influence calcite nucleation and growth, including environmental parameters such as temperature, pH, alkalinity, and the concentrations of calcium (Ca^{2+}) and bicarbonate (HCO_3^-) ions. In our specific protocol, the concentration of $CaCl_2$ used to promote biomineralization was set at 0.01 M, which is considerably lower than the concentrations typically reported in the literature. The rationale behind using such a low concentration of $CaCl_2$

is twofold. First, $CaCl_2$ serves as the donor of Ca^{2+} ions necessary for the formation of $CaCO_3$; second, it functions as a crosslinking agent within the matrix of the bricks. When added at higher concentrations to the liquid bacterial culture, $CaCl_2$ leads to clumping upon contact with sodium alginate, which is used as a structural component of the bricks. This clumping could potentially interfere with the uniformity of the biomineralization process and the overall mechanical properties of the bricks. As such, careful optimization of $CaCl_2$ concentration is critical to balancing its dual role in promoting mineralization and maintaining structural integrity.

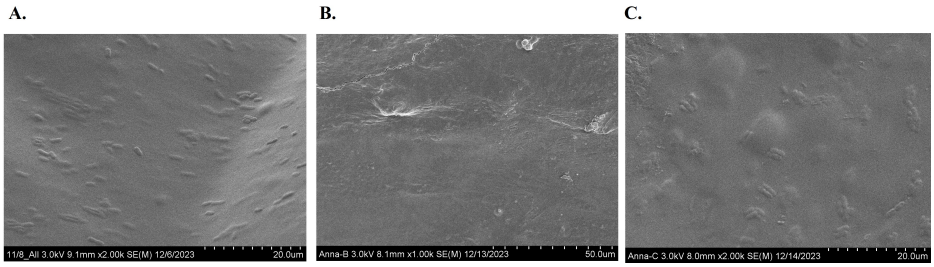

Figure 4.8: Comparison of surface morphology in all samples at similar magnification. Samples with and without cyanobacteria adding the biomineralization enhancers (A-B), and cells without either $NaHCO_3{}^+$ or $CaCl_2$ (C), analyzed through SEM imaging. As expected, bacterial cells were found only in A and C.

In addition to these considerations, the role of cyanobacterial membrane proteins in the biomineralization process should not be overlooked. It is well established that specific membrane proteins, such as the SLP, play a key role in mediating calcite nucleation [144]. The S-layer forms a highly ordered, self-assembling layer on the surface of the cells, providing a structural template that can facilitate the attachment of calcium ions and subsequent nucleation of $CaCO_3$. This protein-mediated process is of particular interest in the context of biomineralization, as it offers a natural and efficient mechanism for directing the formation of minerals at specific sites on the cell surface. Building on this understanding, a potential future direction for improving the biomineralization capabilities of cyano-based bricks involves the use of engineered strains. Specifically, utilizing the SLP platform proposed in this work could help promote stronger attachment between bacterial cells and the surrounding matrix, thereby facilitating more controlled and efficient deposition of calcium carbonate. This approach holds promise for optimizing both the localization and extent of mineralization, potentially leading to enhanced mechanical properties and durability of the bricks.

In conclusion, while the current study provides valuable insights into the mineralization processes within cyanobacteria based bricks, several factors

including the spatial distribution of cells, incubation time, and abiotic influences remain critical areas for further investigation. The use of engineered strains and more precise control over environmental parameters may offer pathways to improve the efficiency and control of biomineralization in future studies.

4.2.2 Carbonic anhydrase library to promote carbonate deposition

In this phase of our work, we focused on the secretion of α carbonic anhydrase (CA) as a novel approach to enhance the biomineralization. Carbonic anhydrase is a well-known enzyme that catalyzes the reversible hydration of carbon dioxide (CO_2) and water to form bicarbonate (HCO_3^-). This process plays a critical role in carbon sequestration, acid-base balance, and other physiological functions across a wide range of organisms, including animals, plants, and algae. Multiple classes of CAs exist, such as α, β, and γ, which all facilitate the same chemical reaction but are involved in diverse physiological processes depending on the organism. These processes can range from ion exchange, respiration, and pH regulation to CO_2 enrichment mechanisms, all of which are integral to photosynthesis. Of particular interest are specific CAs that promote calcium carbonate precipitation through a series of chemical reactions. First, gaseous CO_2 dissolves in water, forming aqueous CO_2. Then, the dissolved CO_2 reacts with water to generate carbonic acid (H_2CO_3), which subsequently dissociates into protons (H^+) and bicarbonate ions (HCO_3^-). Under alkaline conditions, bicarbonate further ionizes to form carbonate ions (CO_3^{2-}) and water. Finally, these carbonate ions react with calcium ions (Ca^{2+}) to form calcium carbonate ($CaCO_3$), which precipitates out of solution.

Despite the increasing interest in using such enzymatic processes to mitigate CO_2 emissions, the engineering and optimization of carbonic anhydrases remain relatively underexplored. Only a handful of CA variants, such as bovine α CA II and a thermostable α CA from the bacterium *Thiomicrospira crunogena*, have been widely used in industrial and engineering applications. This represents a significant gap in the field, which we aimed to address by generating a diverse library of alpha CA sequences, utilizing the secretion platform described in this study. To construct this library, we turned to UniProt, which provided a comprehensive dataset of 18,003 unique, full-length carbonic anhydrase sequences spanning all domains of life. Recognizing that the size and charge of CA proteins may influence their ability to be secreted, we analyzed the dataset for relevant trends. We found that the

majority of CA sequences clustered around 250-270 amino acids in length, with a peak in the isoelectric point (pI) distribution between 5.5 and 6.0. To manage the large dataset and work with a feasible number of variants, we employed MMseqs2 for sequence clustering.

From this dataset, we selected 10 CA sequences for further analysis based on protein length, ensuring that they spanned the entire range of sequence lengths observed (115 to 563 amino acids) while keeping their pI values within the peak range. Additionally, we randomly selected 10 more sequences representing a broad range of pIs, from 4.4 to 8.6. Another set of CA sequences was chosen similarly, including another sequences with pIs between 4.3 and 8.7. Bovine α CA II and the thermostable CA served as benchmarks, bringing the total to 31 sequences for initial characterization.

UMAP, a widely used dimensionality reduction technique for exploring complex, high-dimensional datasets, was employed in this study to visualize the CA sequences selected from the initial dataset provided by UniProt. UMAP is particularly effective in biological applications, including the analysis of protein sequence data, due to its ability to preserve both local and global data structure while reducing dimensionality. This makes it an ideal tool for revealing patterns or relationships that may not be immediately apparent in the high-dimensional sequence space.

By applying UMAP, we transformed the multi-dimensional data of our CA sequences into a more interpretable two-dimensional representation, which is shown in Figure 4.9. To generate this visualization, we set the parameters *n neighbors* = 500 and *min dist* = 0.8, which are critical for determining the balance between preserving local versus global structure in the data. A larger value for *n neighbors* allows UMAP to capture broader relationships across the dataset, while the *min dist* parameter controls the compactness of clusters in the two-dimensional space.

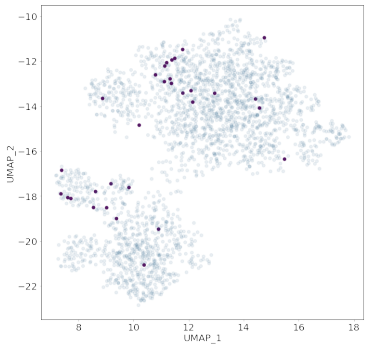

Figure 4.9: UMAP representation of the selected 31 sequences of CAs. In purple the sequences chosen, among the starting dataset of CA versions.

The UMAP projection revealed that the CA sequences we selected, based on both sequence clustering and variation in key features such as protein size and pI, were well-distributed across the two-dimensional plot. This broad distribution suggests that our selection effectively sampled the diversity within the initial UniProt dataset, covering a wide range of CA sequence characteristics. This diverse coverage supports our strategy of selecting sequences that vary across different biological and chemical parameters, ensuring that we explore a broad spectrum of CA functionality in subsequent experiments.

The assessment of the CA library's secretion efficiency was conducted using the HiBiT tag assay. Upon analyzing the results, we found that all constructs within our CA library, with the exception of 10 variants, were successfully secreted (Figure 4.10, A). Among the variants that did not achieve successful secretion, we observed that five of them produced luminescent signals that were significantly lower than those of the negative control, and five showed no statistically significant difference in luminescence compared to the negative control ($p > 0.05$, t-test), suggesting that they were not secreted effectively.

To ensure the functional integrity of the secreted CAs, we sought to investigate their enzymatic activity, particularly in light of the potential for misfolding after secretion (Figure 4.10, B). To this end, we employed a colorimetric assay based on para-nitrophenol acetate, a well-established method for evaluating the activity of enzymes like carbonic anhydrases. Notably, our analysis did not reveal any significant correlation between the pI or the length of the proteins and their enzymatic activity levels. This finding suggests that these characteristics may not directly influence the catalytic efficiency of the CAs we studied. Additionally, we normalized the observed enzyme activity levels by the amount of CA that was secreted. It is possible for a CA to exhibit low activity per-molecule while being secreted in high quantities, resulting in an overall higher activity measurement. The enzyme activity normalized by secretion levels is reported only for those constructs that demonstrated a nitrophenol production level exceeding that of the negative control provided by the assay kit (as shown in Figure 4.10, C).

One particularly interesting observation from our data is that the top-performing CAs in terms of enzymatic activity and secretion are evolutionarily diverse, representing various species including mussels, sheep, and dromedary camels. These CAs exhibited a wide range of pI values, from 4.3 to 8.0, while maintaining a similar length of approximately 250 amino acids. This diversity in origin and biochemical properties underscores the adaptability and functional variability of carbonic anhydrases across different organisms. Intriguingly, despite the fact that most of the high-ranking CAs in Figure 4.10 C originate from the animal kingdom, the first two entries

in our ranking were derived from plant. Another notable result was the inclusion of a thermostable CA, which is not the commonly referenced bovine CA, in the top ten performers of our library.

To further investigate the relationship between evolutionary lineage and enzymatic activity, we constructed a phylogenetic tree to explore the relationships among the various CAs based on multiple sequence alignments performed using the MUSCLE software. We utilized the unweighted pair group method with arithmetic mean (UPGMA) for hierarchical clustering, allowing us to assess whether proteins with similar evolutionary backgrounds exhibited comparable levels of enzymatic activity. However, our analysis did not reveal a clear pattern correlating high activity levels with evolutionary similarity. Instead, it was observed that the CAs exhibiting the highest secretion levels predominantly originated from animal species.

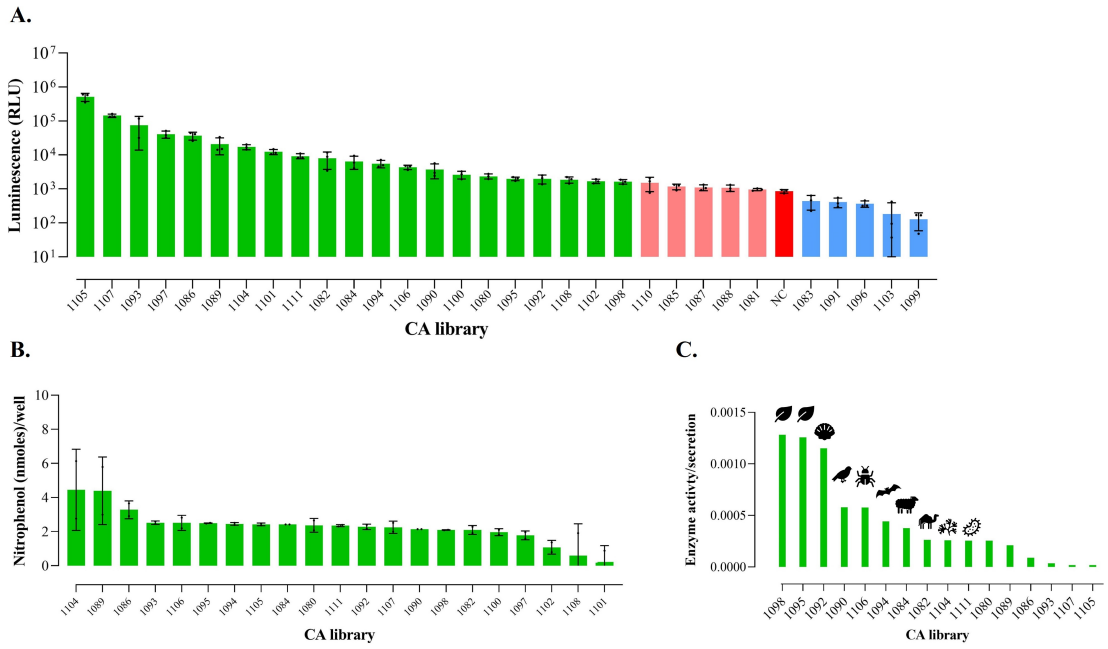

Figure 4.10: Building and testing a carbonic anhydrase library to enhance biomineralization. A) The CAs library, comprising 31 sequences, secreted using our SLP platform. Green bars are the CA variants secreted, pink bars reported no significant differences compared with the negative control, and blue bars resulted in a lower secretion than the negative control. B) Enzyme activity results, obtained using a colorimetric assay, in terms of nmoles/well of nitrophonel. Bars represent the average of a biological duplicate, and error bars are the standard deviation. C) Enzyme acitivity normalized per secretion, showing also the kingdome icon for the top 10 CAs.

Following our initial exploration of the CA library, we set out to construct a second library that would consist of a total of 32 distinct CA variants. This new library was carefully designed to include a variety of CAs aimed at enhancing both secretion efficiency and enzymatic activity. Specifically, it was composed of 25 CAs selected through a systematic probing of the local sequence space surrounding our previously identified highest secreted and highest normalized activity CAs. This approach was guided by the hypothesis that subtle variations in the amino acid sequences of closely related proteins could lead to significant differences in their biochemical properties. In addition, we incorporated one CA sourced from an extremophilic microorganism known for its stability at alkaline pH levels (pH 9). The inclusion of this particular variant was motivated by the potential advantages of alkaline stability for industrial applications, especially in processes that involve CO_2 capture or other biotechnological endeavors where such conditions are prevalent. Furthermore, we also created six additional CA variants using the ProteinMPNN approach. This computational technique leverages deep learning to predict optimal protein sequences based on desired functional and structural characteristics, thereby enabling us to explore a wider range of sequence variations.

In this second round of library construction, we found that 16 of the constructs demonstrated successful secretion, as confirmed by luminescence measurements. In contrast, the remaining constructs yielded luminescence levels that were either lower than those of the negative control or showed no statistically significant difference when compared to the negative control (which is represented by the dotted line in Fig. 4.11, A). When we assessed the enzymatic activity of the secreted CAs, we discovered that only five of the variants exhibited higher levels of enzymatic activity compared to the negative control (Figure 4.11, B). However, it is particularly noteworthy that the activity levels of these five CAs were greater than those observed in the first round of library testing. Among the top five CAs ranked according to their normalized activity (Figure 4.11, C), three were derived from the ProteinMPNN design process. This result might underscore the critical role that rational protein design can play in the development of enzymes with improved yields and heightened functional activity. By leveraging advanced computational tools such as ProteinMPNN, we can achieve results that may not be attainable through random mutations or traditional screening methods.

Overall, the construction and testing of this second library have yielded promising results, indicating that both our selection criteria and the incorporation of novel design methodologies have contributed to the development of a diverse and functional set of carbonic anhydrases. The ongoing investigation of these variants will be crucial for determining their applicability in

various biotechnological contexts, particularly in efforts aimed at improving carbon dioxide fixation and boosting the precipitation in the cyanobacteria materials through innovative enzymatic solutions.

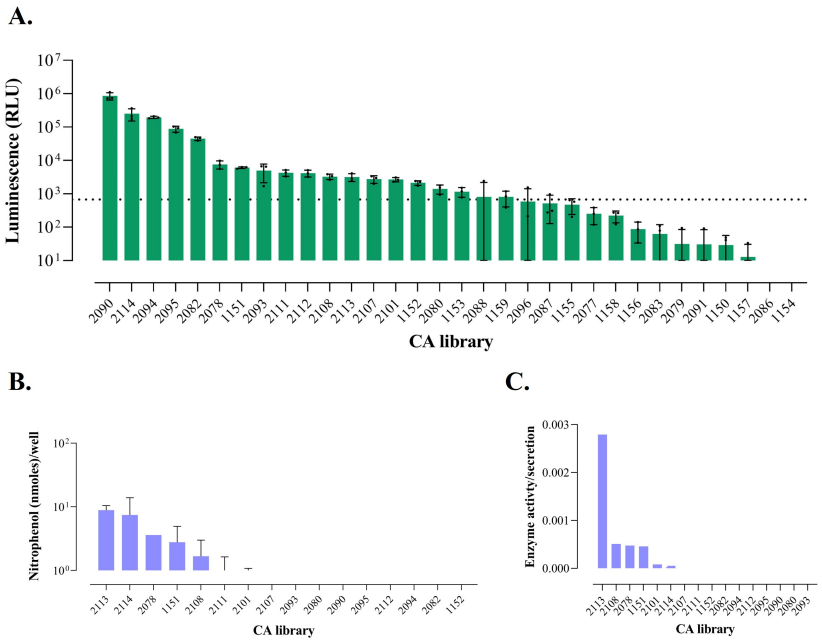

Figure 4.11: Building and testing a carbonic anhydrase library to enhance biomineralization. A) The CAs library, comprising 31 sequences, secreted using our SLP platform. Bars are the mean of a biological triplicate, black circles are the single values, and the error bars represent the standard deviation. The dotted line represents the negative control used as a threshold. B) Enzyme activity results, obtained using a colorimetric assay, in terms of nmoles/well of nitrophonel. Bars represent the average of a biological duplicate, and error bars are the standard deviation. C) Enzyme acitivity normalized per secretion.

In summary, the library of 63 CA variants provided valuable insights into how factors such as protein length, pI, and species of origin affect secretion and activity. While approximately half of the library did not meet the threshold for secretion, the remaining variants, particularly those optimized through computational design, showed promising results. The second round of testing resulted in higher levels of both secretion and enzymatic activity than the first, underscoring the importance of iterative optimization and the potential of machine learning techniques like ProteinMPNN in enzyme design. As a result, this study advances our understanding of how to develop CAs with enhanced functionality, paving the way for their use in carbon capture, environmental remediation, and other biotechnological applications.

4.2.3 Dehydration tolerance through tardigrade derived proteins

To investigate whether tardigrade-derived proteins (TDPs) could serve as effective protectants in environments characterized by extreme stress, we engineered UTEX 2973 to express a specific TDP known as cytosolic-abundant heat soluble protein (CAHS). This protein was sourced from the tardigrade species *Paramacrobiotus richtersi*, which is renowned for its remarkable ability to endure harsh conditions such as desiccation, extreme temperatures, and high radiation. Our goal was to determine whether the introduction of CAHS into UTEX 2973 could enhance the strain's ability to survive under similar stressful conditions, specifically dehydration.

We embarked on this investigation by engineering different versions of the UTEX 2973 strain, each expressing CAHS in distinct ways. These included: regular cytosolic expression, secretion of the protein into the surrounding medium, and surface display, in which the protein would be anchored on the outer membrane of the cell. The expression of these TDPs was facilitated using the secretion platform we developed, as outlined in Section 4.1.2. By exploring various forms of TDP localization within or around the cells, we aimed to uncover the most effective mode of protection against desiccation stress.

The experiment was structured around a desiccation protocol designed to mimic extreme dehydration conditions. The results showed that only versions expressing CAHS, whether through cytosolic expression, secretion, or surface display, demonstrate the ability to survive after five days of dehydration (Fig. 4.12, A). This clearly indicated that the presence of TDPs, in any form, conferred a significant advantage under desiccation stress. Among the three types of TDP-based strains, the strain with intracellular expression of CAHS (light green bar in Fig. 4.12, A) showed the most promising results. This strain maintained a robust level of survival, with CFU/ml counts around 10^7 even after undergoing the desiccation assay (Fig. 4.12, B). The high survival rate observed in this strain suggests that CAHS, when expressed in the cytosol, may be particularly effective at stabilizing cellular components during dehydration and subsequent rehydration, thus preventing irreversible damage to critical biomolecules.

In contrast, the control strains, which included the wild-type UTEX 2973 and a strain carrying an empty plasmid (i.e., without TDP expression), fared much worse in the desiccation test. None of the control strains were able to form colonies following dehydration, indicating a complete loss of viability under these conditions. This difference between the engineered strains and the controls highlights the importance of TDPs in facilitating cellular survival

during extreme stress, as their absence led to a total failure to recover from dehydration.

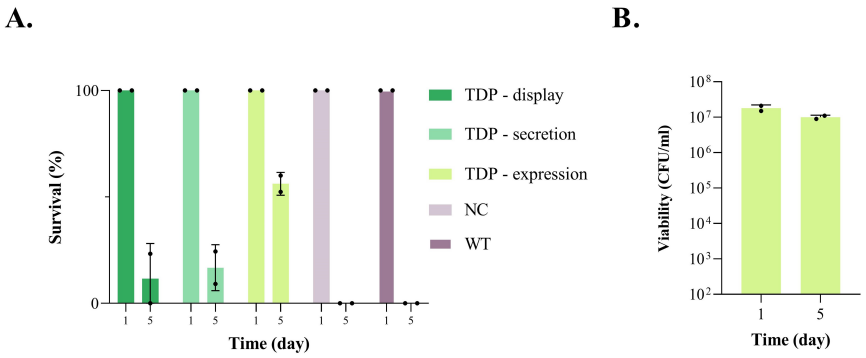

Figure 4.12: A) Viability after dessication condition. Only the conditions in which TDP is present survived after the dessication assay. B) Viability in terms of CFU/ml of the construct in which TDP is expressed as an intracellular protein in a plasmid. Bars are the mean of a biological triplicate, black circles are the single values, and the error bars represent the standard deviation. A-B) Bars refer to the mean of a biological duplicate, black points are the single values and error bars standard deviation.

Taken together, these findings underscore the potential of tardigrade-derived CAHS proteins as potent protectants against desiccation, providing UTEX 2973 with a remarkable degree of resilience in environments that would otherwise be lethal. The fact that the cytosolic expression of CAHS resulted in the highest survival rate suggests that intracellular protection is particularly crucial in safeguarding cells from the damaging effects of water loss. Other studies demonstrated that exogenous expression of CAHS proteins in both prokaryotic and eukaryotic cells is sufficient to increase desiccation tolerance in these systems, like the work of Boothby et al., in which they assessed the ability of engineed yeast and bacteria, subjected to desiccation and rehydration, to increase the desiccation tolerance [145].

Furthermore, they proved that CAHS proteins, like trehalose, vitrify when dried. This might explain why the construct in which TDP is regular expressed, not displayed nor secreted, is the condition in which we found the highest level of survival after 5 days, since the vitrified state might rely on the presence of the protein inside the cell. However, the other forms of TDP expression, such as secretion and surface display, also contributed to survival, indicating that different strategies for protein localization may be worth exploring further in future studies.

Given that the TDP-expressing plasmids were designed to achieve the final brick prototype, we investigated the reliability of plasmid stability without antibiotic selection over a two-week period, which should be sufficient for the cells to complete their biomineralization. Over this timeframe, we streaked four strains expressing TDP under different promoters (with high, medium, and low transcriptional strengths). On days 2, 4, and 14, we selected ten colonies and performed colony PCR to verify the presence of the plasmid in each construct. On days 2 and 4, 100% of the tested colonies showed successful amplification of the expected PCR band, confirming the presence of the plasmid (Fig. 4.13). After two weeks, 80% of the colonies still retained the plasmid across all constructs tested. Interestingly, the strain expressing TDP under a strong, native S. elongatus promoter showed plasmid retention in only 60% of the colonies, potentially due to TDP toxicity at high expression levels or an insufficient number of colonies per PCR, which may have led to this discrepancy.

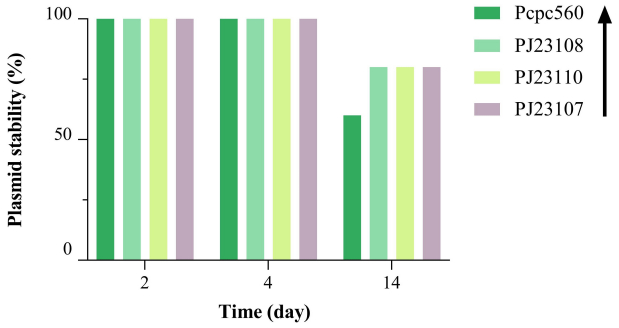

Figure 4.13: Plasmid stability through colony PCR over 14 days. Day 2, 4 and 14 were chosen for picking the colonies from the plates without antibiotic selection. After two weekd a decrese of the stability is shown, especially for the strongest promoter tested native in *S. elongatus* Pcpc560. In the legend from the top the promoters according to their strength.

Nonetheless, the ability to use ELMs in real-world applications for up to two weeks without requiring additional antibiotic selection is a promising starting point. Further improvements could focus on enhancing the stability of the genetic circuits, extending the duration of the experiment, and testing the material's performance in its intended function, as the presence of an insert by PCR serves as proof of plasmid retention, but not necessarily its functionality. An alternative final solution to avoid antibiotic selection would be to integrate the desired function genomically, ensuring stable and long-term expression of the specific trait.

In summary, the results of this study demonstrate that tardigrade-derived proteins, particularly CAHS, can significantly enhance the survival of cyanobacteria under desiccation stress. This opens up exciting possibilities for engineering microorganisms capable of thriving in extreme environments, which could have important applications not only for the ELM research area, but also in biotechnological production, biofuels, and even space exploration, where organisms must withstand challenging conditions.

4.3 Final considerations

A novel S-layer protein was engineered and characterized in the fast-growing UTEX 2973 to realize a platform for two key tools essential in biomanufacturing: surface display and protein secretion. The mininal signal peptide required for secretion was chosen at 150 AA before the C-terminus, then used to realize all the constructs conceived for protein production. From the analysis of the surface, the SLP was able to display a bioluminescent tag in almost all the locations of the middle domain, proving its homogeneity, and one location was chosen to successfully display two proteins relevant in the field of biomaterial and ELMs (e.g., ELP_{60} and TDP).

A number of different proteins and enzymes were tested to validate the secretion platform, which led to the successful transport in the extracellular environment of almost all targets. However, further studies are necessary to understand the correlation between the type of protein and secretion, as well as the yield of the system essential to certify the robustness and the efficiency of the platform.

The feasibility of using cynaobacteria as a phototrophic component to create living building materials has been demonstrated. Without using sophisticated and high-cost technologies, a workflow was established to obtain brick prototypes as a proof-of-concept of materials capable of fixing CO_2, producing biocement and with self-repairing characteristics. Mechanical tests after one week of incubation reported promising results, although SEM analyzes highlighted how the pipeline cannot guarantee spatial control of the cells and therefore homogeneous biomineralization, which was also observed in the negative control due to the presence of $CaCl_2$ and $NaHCO_3{}^+$. To observe a significant increase in biomineralization, prolonged incubation periods and the use of secreted or surface displayed CAs will be investigated.

Engineered versions of CAs have been investogated as they could be used to improve the efficiency of carbon fixation by optimizing CO_2 concentrating mechanisms, overcoming environmental limitations. This might enhance photosynthetic efficiency and biomineralization, which has significant impli-

cations for biotechnological applications. In this thesis, a library of 63 versions of CAs was built and characterized in terms of secretion and activity. ProteinMPNN has proven to be a valid tool for achieving performance levels that would otherwise not be feasible. Overall, a few variants of CA showed promising results and they represent the starting point for further investigations and studies to prove their role in boosting carbonate precipitation.

Another genetic engineering approach linked with cyanobricks is the possibility to make cells able to survive at harsh environments. We this aim, we engineered cells using TDPs and showing how expressing them results in the survival of UTEX 2973 after a dessication assay over 5 days. Finally, the study of plasmid's stability was addressed for field applications with no antibiotics added, and was proven even after 14 days without selection.

Overall, these data confirm that by choosing a fast-growing chassis like UTEX 2973 it is possible to engineer cyanobacteria in a reasonable time and obtain robust tools for various applications. Surface display as a screening method or as a matrix for attaching biomaterials, secretion of proteins relevant for industrial and therapeutic market, a platform for creating living materials with carbon negative building and climate change mitigation purposes have been demonstrated. Ongoing efforts are still needed, but since this field is still in its first years of blooming, the continuous progress of synthetic biology will certainly allow us to move in this direction, towards a greener, and more sustainable research.

Chapter 5

Conclusions

The overarching goal of this PhD research was to develop and refine methods for creating engineered living materials (ELMs) with practical biosensing, biomanufacturing, and environmental applications. This work investigated various key aspects of bacterial bioprinting, the design of biosensor devices for clinical, agricultural, and industrial applications, and the use of cyanobacteria as a phototrophic chassis for biomanufacturing and carbon capture. Across the three parts of this research, significant progress was made in demonstrating the potential of ELMs for real-world deployment, addressing challenges such as environmental compatibility, functional complexity, and long-term stability. The following conclusions summarize the achievements and insights from each section of the thesis, highlighting the technological and scientific contributions of this research.

In the first part of this work, a bacterial bioprinting workflow was successfully developed to fabricate biosensing devices. These biosensors were tested in various environments, including nutrient-poor conditions (e.g., water) and complex clinical matrices (e.g., clinical derived supernatants, and bronchial aspirates). A significant outcome was the demonstration of efficient and reproducible biosensing in these challenging environments, a key requirement for field applications in environmental monitoring and clinical diagnostics. For instance, the successful detection of the *P. aeruginosa* autoinducer in clinical samples demonstrated the potential of these biosensors for use in rapid detection kits. Importantly, these bioprinted materials maintained viability and functional stability for over two weeks and could be stored for more than a month under refrigeration, making them practical for real-world use. However, sensitivity was influenced by environmental factors, necessitating careful calibration for application-specific conditions to optimize detection limits.

Furthermore, by incorporating multiple bacterial strains within the same bioprinted material, it was possible to create devices capable of multiplexed sensing, semi-quantitative detection, and cell-cell communication mediated patterning, significantly enhancing the complexity and capabilities of these biosensing systems.

Overall, this work provided a foundation for further automation of the bioprinting process, streamlining the design and prototyping of bacteria-laden biosensors.

The second part of the thesis expanded on the initial bacterial bioprinting workflow, shifting the focus toward agro-industrial applications. Eleven biosensors were characterized for the detection of molecules relevant to agriculture, such as VOCs, acetate, nitrates, and phosphates. Some biosensors were excluded due to unsuitability for the conditions tested, while others demonstrated promising performance but highlighted the need for extensive optimization. For example, the strong influence of pH on biosensor performance and the crosstalk between nitrate and phosphate detection were key findings that will inform future biosensor design and calibration efforts. Moreover, the prototying process also included a tuning of the non living component of the ELM, to meet a set of specifications to guarantee the bacterial biosensor functioning.

The potential applications of these biosensors in agriculture are significant. By enabling targeted and sustainable fertilization strategies, farmers could reduce environmental impacts while optimizing crop production. Similarly, biosensors could be used in industrial processes to improve efficiency and performance, particularly in digestion systems. However, ongoing experiments are still required to finalize the characterization of ELM sensors for soil monitoring, specifically in real soil samples with known nutrient concentrations.

A critical challenge identified in this section was the impact of environmental variability on biosensor performance. Factors such as temperature, pH, and nutrient availability can significantly affect biosensor stability and functionality, making it difficult to maintain consistent performance in real-world conditions. In addition, complex mixtures of substances in real samples, such as soil or digestate, can interfere with the biosensor signal output, necessitating careful calibration and design to minimize cross-reactivity and signal noise.

The use of a physical biocontainment strategy, such as the PDMS-box sealed with a PES filter membrane, was demonstrated an effective solution for preventing the GMOs escape. Furthermore, a straightforward method for analyzing biosensor output using low-cost equipment, such as a smartphone camera and green laser pointer, was successfully tested, providing a promising

approach for real-time field monitoring in low-resource settings.

The final section of this research explored the potential of cyanobacteria as a chassis for creating living building materials with biomanufacturing and environmental applications. The fast-growing cyanobacterium UTEX 2973 was engineered to display and secrete proteins, providing a platform for surface display, protein production, and biomineralization. A novel S-layer protein was developed and characterized, successfully displaying relevant proteins for industrial and environmental applications. Additionally, this research demonstrated the secretion of various proteins and enzymes, although further studies are needed to optimize protein yield and secretion efficiency.

An innovative aspect of this work was the creation of cyanobacteria-based bricks, living building materials capable of CO_2 fixation, biocement production, and self-repair. While mechanical tests showed promising results, challenges such as uneven cell distribution and biomineralization remain to be addressed. Nevertheless, this proof-of-concept highlights the potential of cyanobacteria to contribute to carbon-negative building materials, a critical technology for climate change mitigation. In addition, a library of 70 engineered versions of carbonic anhydrase was constructed and characterized, with a few variants showing promising results for enhancing carbonate precipitation. These engineered enzymes could improve the efficiency of CO_2 capture and biomineralization in future applications. The engineering of cyanobacteria to survive harsh environments, such as desiccation, was also demonstrated exploiting TDP, further supporting the potential for these organisms to be used in challenging environmental conditions.

Together, these findings demonstrate the feasibility of using cyanobacteria as robust tools for biomanufacturing and environmental sustainability, but ongoing efforts are needed to address current limitations and fully realize their potential.

In conclusion, this PhD research provides a blueprint to achieve a platform for creating ELMs with different purposes, ranging from clinical diagnostics to environmental and industrial monitoring, and climate change mitigation. Although challenges remain, especially considering the outside-the-lab applications, the advances made in this research provide a strong foundation for future developments in the field. With continued progress in synthetic biology, these engineered living systems are poised to play a transformative role in creating greener, more sustainable technologies for the future.

Appendix A

First Appendix

Appendix A comprises all the materials and methods used for carrying out the experiments and work described in Chapter 2 and 3.

A.1 Reagents, media, and strain construction

A.1.1 Bacterial strains

The *E. coli* strains are derivatives of TOP10, MG1655, and MG1655-Z1. MG1655-Z1 is similar to MG1655, with additional constitutive overexpression cassettes for LacI and TetR, which make the PLlacO1 and PLtetO1 promoters inducible.

A.1.2 Cloning

Plasmid construction was performed with the BioBrick Standard Assembly procedure, starting either from available plasmids from the Registry of Standard Biological Parts or from PCR amplification, adding restriction enzymes site through site directed mutagenesis.

Plasmid DNA previously purified via Plasmid kit (Macherey Nagel) was digested with EcoRI/XbaI/SpeI/PstI restriction enzymes (Thermo Fisher). Digestion products were separated on 1% agarose gel electrophoresis, extracted via PCR Cleanup kit (Macherey Nagel), and assembled using T4 ligase (Thermo Fisher). Enzymes and kits were used according to manufacturer instructions. *E. coli* transformation was done by heat shock at 42 °C, using chemically competent cells. Strains were routinely grown at 37 °C, 220 rpm, in 5 ml of L-broth (LB) medium (1% NaCl, 1% tryptone, 0.5% yeast

extract, 1.5% agar for solid media) and long-term stored at -80 °C in 20% glycerol stocks. Sequencing was performed by Eurofins Genomics (Ebersberg, Germany).

A.1.3 Reagents

Ampicillin (100 μg/ml), kanamycin (25 μg/ml), and chloramphenicol (12.5 μg/ml) were used to select *E. coli* with genetic circuits in the pSB1A2, pSB3K3 and pSB4C5, respectively.

The *Vibrio fischerii* autoinducer N-3-oxohexanoyl-l-homoserine lactone (VAI, K3007, Sigma Aldrich), *Pseudomonas aeruginosa* autoinducer (PAI, O9139, Sigma Aldrich), Isopropyl-β-d-1-thiogalactopyranoside (IPTG, I1284, Sigma Aldrich), anhydrotetracycline (aTc, 631310, Clontech), and tetracycline (Tc) were used as biosensor inputs. Sodium alginate (W201502, Sigma Aldrich) and gelatin (G9391, Sigma Aldrich) were used as hydrogel components. Catechol (C9510, Sigma Aldrich) was used at 10 mM for XylE yellow staining.

A.1.4 Digestate

The liquid, acetate free digestate mentioned in Chapter 3 for carrying out the preliminary experiments originates from a mix of civil wastewater sludge, processed through thermophilic anaerobic digestion at 56 °C in a completely stirred tank reactor (CSTR) with a hydraulic retention time (HRT) of 30 days. The digestate has an average pH of 7.96 and a chemical oxygen demand (COD) of 225 g/L. Total solids (TS) make up 4.14%, with volatile solids (VS) accounting for 56.96% of the TS, representing the organic matter. The sludge was fed daily with a mixture of 12g Nortembio molasses and 100 mL tap water, while 15g of pyrochar was injected into the reactor weekly. The organic loading rate (OLR) of the process was 2.5 g COD per liter of digester per day.

A Table reporting the amount of acetic acid (mg/L) for each digestate sample used in the thesis (Figure 3.17) is shown below. Acetic acid was detected through gas chromatography with flame ionization detection (GC-FID), a standard analytical technique commonly used for separating and analyzing volatile organic compounds.

Sample ID	Acetic acid (mg/L)	Sample ID	Acetic acid (mg/L)
1	19,14	**51**	27,41
2	29,52	**52**	22,76
3	86,39	**53**	25,71
4	182,59	**54**	24,31
5	94,61	**55**	21,67
6	261,83	**56**	655,6
7	19,89	**57**	738,72
8	14,81	**58**	80,78
9	20,44	**59**	48,49
10	51,47	**60**	24,87
11	192,02	**61**	39,21
12	344,39	**62**	69,5
13	36,71	**63**	195,15
14	41,36	**64**	63,22
15	86,08	**65**	285,4
16	115,49	**66**	176,52
17	27,11	**67**	249,14
18	46,74	**68**	893,57
19	101,52	**69**	48,32
20	19,71	**70**	30,77
21	31,21	**71**	49,5
22	23,28	**72**	138,34
23	50,98	**73**	43,52
24	72,27	**74**	41,67
25	105,66	**75**	41,45
26	32,09	**76**	41,42
27	109,21	**77**	5451,04
28	90,93	**78**	35,01
29	32,8	**79**	273,87
30	21,03	**80**	213,78
31	74,85	**81**	45
32	20,29	**82**	181,27
33	30,47	**83**	951,8
34	164,58	**84**	64,77
35	61,29	**85**	29
36	256,94	**86**	42,17
37	49,37	**87**	46,45
38	53,23	**88**	51,79
39	60,4	**89**	143,67
40	28,93	**90**	178,12

Sample ID	Acetic acid (mg/L)	Sample ID	Acetic acid (mg/L)
41	98,02	**91**	68,72
42	189,52	**92**	3298,41
43	31,15	**93**	22,79
44	55,74	**94**	12,55
45	165,41	**95**	16,61
46	44,16	**96**	2890,52
47	52,47	**97**	50,32
48	17,48	**98**	36,84
49	209,74	**99**	22,02
50	121,83	**100**	28,99

Table A.1: First round of digestate samples (batch 1-100).

Sample ID	Acetic acid (mg/L)	Sample ID	Acetic acid (mg/L)
101	10,61563	**151**	19,92038
102	9,524623	**152**	15,22998
103	13,03702	**153**	13,92757
104	43,13468	**154**	9,194239
105	14,86101	**155**	12,81192
106	9,197834	**156**	14,75772
107	10,21004	**157**	10,96257
108	10,17519	**158**	12,27962
109	9,90727	**159**	10,23814
110	12,32249	**160**	10,90049
111	13,38935	**161**	12,87639
112	13,88491	**162**	10,56099
113	16,22665	**163**	8,982489
114	10,23796	**164**	26,42321
115	11,511	**165**	13,103
116	15,90106	**166**	8,285631
117	13,20501	**167**	6,782672
118	8,48132	**168**	12,16137
119	8,122971	**169**	11,79824
120	10,0596	**170**	8,690355
121	8,805595	**171**	15,68384
122	13,86954	**172**	13,66179
123	10,22254	**173**	15,22432
124	8,432763	**174**	8,851514
125	16,03306	**175**	36,52986

Sample ID	Acetic acid (mg/L)	Sample ID	Acetic acid (mg/L)
126	14,15039	**176**	7,387392
127	14,19785	**177**	13,18147
128	11,52372	**178**	16,61592
129	11,85358	**179**	11,11167
130	8,53667	**180**	9,542132
131	8,313014	**181**	10,45285
132	10,1514	**182**	10,30681
133	17,13585	**183**	0
134	9,36874	**184**	7,061479
135	12,33075	**185**	29,80228
136	13,79375	**186**	19,64313
137	10,6935	**187**	12,40114
138	9,087757	**188**	10,24805
139	12,63987	**189**	10,73078
140	8,602895	**190**	15,63947
141	10,19881	**191**	12,16763
142	15,17183	**192**	15,22467
143	15,07339	**193**	13,09583
144	14,29698	**194**	8,547462
145	18,00522	**195**	13,25303
146	14,83118	**196**	35,7942
147	6,707263	**197**	10,01773
148	13,77195	**198**	8,35928
149	12,34437	**199**	7,593418

Table A.2: Second round of digestate samples (batch 101-199).

A.2 Bioprinting

A.2.1 Hardware and software

The extrusion-based CELLINK INKREDIBLE+ bioprinter (Cellink AB, Sweden), equipped with two printheads (PHs), was adopted. Structures were designed as CAD files using the Autodesk Inventor Pro software (Autodesk, United States), then the CAD model was sliced using Slic3r, an open-source slicing software. During the slicing process, printing parameters (e.g., layer height, perimeter, printing speed, infill percentage) were defined. After slicing, the specific set of instructions (i.e., G-code) was created and constructs were 3D printed.

A.2.2 Hydrogel and bioink optimization

An 8% (w/v) sodium alginate and 4% (w/v) gelatin hydrogel was prepared one day before use by dissolving gelatin powder in pre-warmed PBS (70 °C) and then dissolving sodium alginate. The hydrogel was supplemented with antibiotics as required, and stored at 4 °C.

Preliminary tests aimed to select bioink composition in terms of hydrogel and nutrients, growth conditions for ELMs, printing support, and crosslinking procedure (Figure A.1). Among the variables tested, hydrogel composition and concentration did not affect cell growth; the nutrient content in the bioink slightly affected it without any visible change in RFP production. The main factor affecting RFP production was the presence of external medium nutrients, which were required to achieve intense red pigmentation. This requirement was expected since bacterial density was slightly lower than previous studies and nutrients could allow for bacterial proliferation after printing [146].

The scheme illustrating all the steps of the defined workflow based on the screening results is shown in Fig. A.1.A. The main variables screened during protocol development are illustrated in Fig. A.1.B: incubation, crosslinking, hydrogel composition, and nutrient concentration. Screening outcomes are reported as double ticks, single ticks, and crosses, qualitatively corresponding to a good condition, a reasonably good condition but not the best among the tested ones, and a non-satisfying condition, respectively. These results are relative to screening procedures carried out with manually extruded or bioprinted structures, as indicated. For bioprinted structures, the minus sign corresponds to non-tested conditions.

The reported pictures and graphs in subpanels show examples supporting the selection of the variables. All the screening experiments were carried out in single or duplicate tests, using RFP expressing (high copy number) strain as the living component. Among the hydrogel conditions tested, the 6% (w/v) alginate concentration gave qualitatively poor structural tone in manually extruded and crosslinked inclusions compared with the other hydrogels, not allowing reliable handling (data not shown), and was not further considered for bioprinting. The other hydrogels gave reasonably satisfactory results, with the addition of gelatin giving superior toughness.

The manually extruded and crosslinked structures with two different hydrogels (8% (w/v) sodium alginate and 8% (w/v) sodium alginate + 4% (w/v) gelatin, both containing 2-fold concentrated LB nutrients) were incubated on solid LB, liquid LB medium, plastic, or PBS. The two conditions with the exogenous LB supported intense color development, suggesting that

additional energy sources to the medium components in the bioink were necessary to support efficient growth and/or expression (panel B-I).

Solid medium was further selected, consistent with previous works, since incubation in liquid media caused a rapid contamination of the liquid by planktonic growth, probably depleting some nutrients, and resulting in a more variable color development across the experiments and in different parts of the inclusions (panel B-II). In addition, all the hydrogels supported cell growth and protein expression in the tested conditions (2-fold concentrated LB in the bioink, incubation on solid LB), based on colony count and visual inspection of intense red color: no difference in cell viability profile was observed over about a week on solid medium in alginate concentrations at 8% and 10% (w/v), and at 8% (w/v) with the addition of 4% (w/v) gelatin (panel B-I).

Removal or addition of LB nutrients had a low impact on cell viability (panel B-IV), evaluated with a 8% (w/v) sodium alginate + 4% (w/v) gelatin bioink, confirming that the exogenously provided nutrients play a major role; among the LB nutrient levels tested in the bioink, the 2-fold concentrated LB condition was selected since it supported a slightly higher cell viability than the standard LB (panel B-IV). The data in panel B-IV further support the selection of solid medium instead of liquid medium due to the superior cell viability over time per mg of dissolved material.

Crosslinking was successfully carried out with manually extruded structures by applying a drop of calcium chloride for 5 min, or by directly extruding the bioink on calcium chloride-supplemented LB. However, the latter procedure failed in the bioprinting because of frequent nozzle clogging probably due to non-perfectly flat media surfaces and it was not further adopted. Finally, bioprinting tests confirmed that the gelatin-including hydrogel could be handled more reliably after crosslinking, without disrupting the structure (panel B-V).

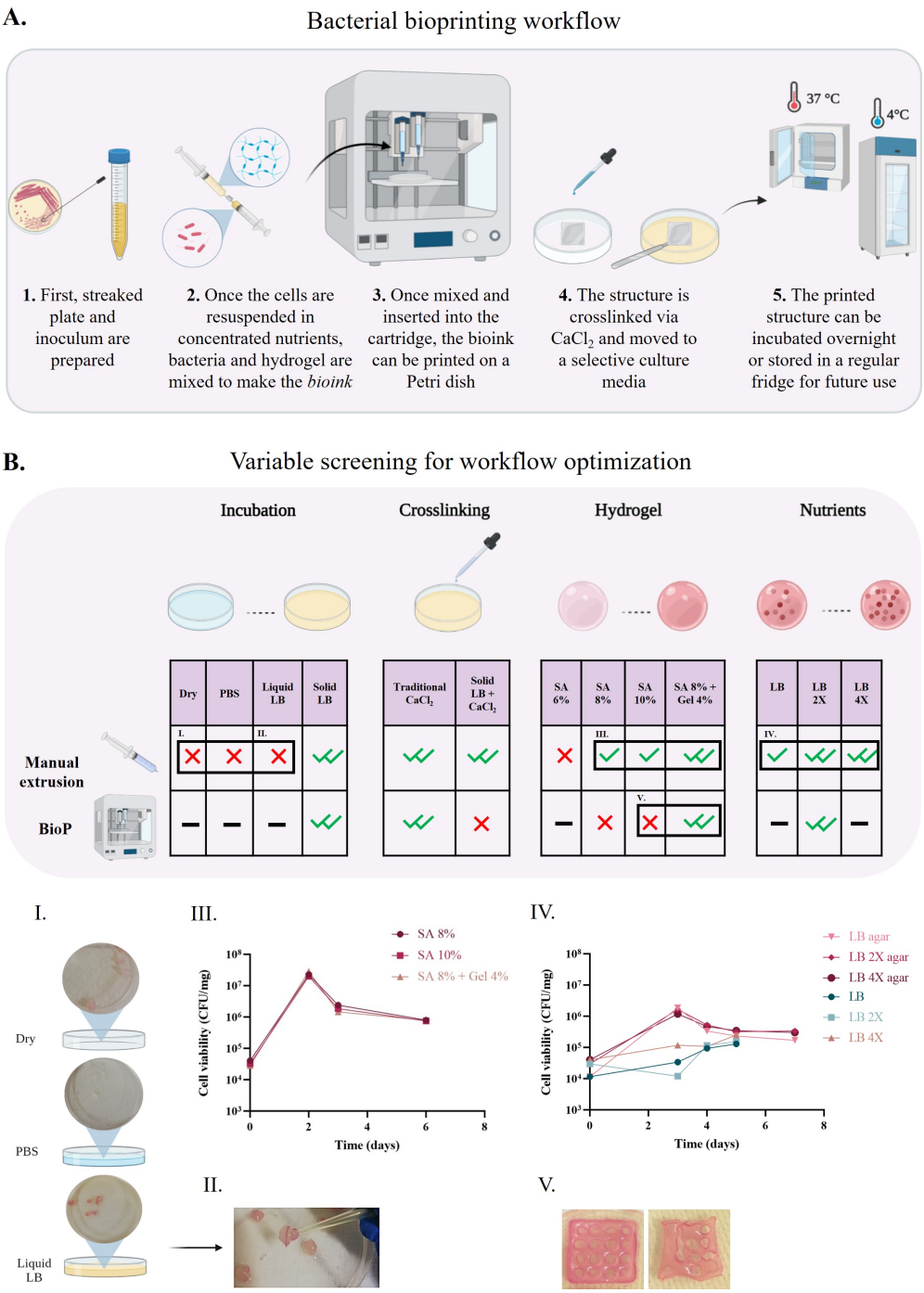

Figure A.1: Bacterial bioprinting workflow used in this work and screened variables.

A.2.3 Printing procedure

Unless otherwise indicated, bacteria from a saturated culture, grown in selective LB medium at 37 °C, 220 rpm, were centrifuged (4000 rpm, 10 min); the supernatant was removed and the pellet was resuspended with the same volume of 2-fold concentrated LB medium. The resuspended culture was mixed at 1:10 ratio with the hydrogel at room temperature using two syringes with a Luer connector. The prepared hydrogel-bacteria mixture, referred to as bioink, was loaded into the printer cartridges and the printing was performed on Petri dishes using a 0.41-mm nozzle, pressure from 15 to 25 kPa, and an extrusion speed of 800 mm/min. After printing, the construct was crosslinked for 5 min using 2% (w/v) calcium chloride, which was removed with a pipette and the structure was moved onto selective LB agar. The structure was then moved to fresh LB agar at specific time points to extend cell viability and crosslinking was occasionally refreshed to maintain structural integrity of printed construct.

A.3 ELM characterization

A.3.1 Microscopy

Fluorescent protein expression by printed bacteria was observed with the Eclipse 80i microscope (Nikon). Fluorescence images were taken via the Image-Pro Plus software. The TRITC (excitation/emission: 520.5/582 nm) and FITC (495/528 nm) channel setups were used to measure the red and green fluorescence of mRFP1 and GFPmut3b, respectively. ELM slices were cut with a scalpel and they were imaged on a microscope slide with a 4× objective.

A.3.2 Cell viability

Bacterial cell viability was quantified via colony counts in dissolved ELMs. A pre-weighted structure was immersed in 2 ml of 0.1 M sodium citrate in a 15-ml tube and incubated at room temperature for 1 h on a rolling shaker set at slow rotation. Serial dilutions were plated on selective LB agar and incubated at 37 °C overnight. Colony count was multiplied by dilution factor and expressed as colony forming units (CFUs) per mg of structure. No detectable toxicity by sodium citrate, in terms of CFUs, was observed in preliminary tests in which liquid cultures were incubated as above in 0.1 M sodium citrate or PBS, used as control, before plating (data not shown).

A.3.3 Preliminary biosensor tests in liquid cultures

Fluorescence assays were carried out in a microplate reader (Infinite F200Pro, Tecan), measuring growth (OD; absorbance at 600 nm) and red fluorescence (RFP; excitation/emission: 535/620 nm) every 5 min. Data analysis included background subtraction from raw absorbance and fluorescence by using media and a non-fluorescent culture, respectively; biosensor output was computed as RFP/OD, expressed in arbitrary units (AU) of per-cell fluorescence. Quantification of unknown PAI concentration in *P. aeruginosa* contaminated samples was carried out using a similar protocol with the VAI-sensing strain, including a standard PAI calibration curve as previously described. After considering the dilution of unknown samples in the biosensor cultures, the lower detection limit was about 200 nM of PAI.

Aerobic condition

Unless differently indicated, strains were grown overnight (37 °C, 220 rpm) in 0.5 ml of selective M9 supplemented medium (M9 salts - M6030, Sigma Aldrich - 11.28 g/l, thiamine hydrochloride 1 mM, MgSO4 2 mM, CaCl2 0.1 mM, casamino acids 0.2%, glycerol 0.4%). They were 100-fold diluted in 200 l of the same medium and incubated in 96-well plates at 37 °C with linear shaking (3 mm, 5 s before sampling). Inducers (VAI, PAI, aTc or Tc) were added in the 200 μl cultures at the specified concentrations.

Low oxygen condition

In this setting, strains were grown overnight (37 °C, 220 rpm) in 0.5 ml of the selective medium chosen. They were 50-fold diluted in 2 ml of the selective medium, in falcon tubes, induced at the specified concentrations, and grown overnight (37 °C, 220 rpm). Exponential phase was studied analyzing the cultures after 3 h of growth, while the stationary phase after 24 or 30 h (diluiting them 2 or 4 fold in PBS solution, before reading at the microplate reader).

A.3.4 Test of biosensor ELMs

Unless differently indicated, biosensing assays with ELMs were carried out by placing patch structures (20 x 20 x 1.4 mm), at specific time points, on selective LB agar containing chemical inducers to guarantee full induction of the respective expression systems (VAI and PAI at 400 nM, aTc and Tc at 200 ng/ml, IPTG at 100 μM), and incubated at 37 °C. RFP output was observed by visual inspection after a specified time. Overnight refers to 16-24 h. XylE assays were performed analogously, with the exception that the structures had letter geometries instead of patches, were removed from the plate and catechol was added to start the enzymatic reaction yielding the

yellow product 2-hydroxymuconic semialdehyde. Induction was carried out at different times to test the robustness of sensing ELMs and day 0 refers to the day of bioprinting. When indicated, structures printed at day 0 were stored at 2-8 °C on LB agar plate for the specified time until further use.

A.3.5 Biosensing tests in environmentally relevant samples

VAI detection in soil

VAI detection by sensing ELM was tested in commercial topsoil (Esselunga, Italy) and tap water. ELMs were printed and incubated in LB agar as above. At day 1, VAI was added to the soil by adding about 10% (w/w) water containing the autoinducer at a 400 nM concentration, and structures were placed in the induced soil. The same concentration of VAI was added to 100 ml of tap water and structures were immersed overnight. Incubation was carried out at room temperature.

Nitrate detection in soil

For nitrate sensing in soil samples, we used an aluminum container with a volume of approximately 56.55 cm^3. Given that the volumetric moisture content (VMC) was set at 53%, we added 10 ml of water induced with KNO_3 to 5 grams of soil (previously dried for three days in an oven at 50 °C). Unless otherwise indicated, the biosensors were pre-incubated overnight at 37 °C on agar medium, then placed on the soil and covered with aluminum foil at room temperature overnight. The results were then expressed as nitrate nitrogen per kilogram of soil.

Acetate detection in digestate

For acetate sensing in digestate samples, 5 grams of digestate were weighed and placed into Falcon tubes, followed by centrifugation at 2500 rpm for 5 minutes at room temperature. The supernatant was then filtered and diluted at a 1:5 ratio. Depending on the size of the sensor patches, either 200 μL (for patches with a 2 cm side) or 100 μL (for patches with a 1 cm side) of the diluted liquid were used (spiked or not). Unless otherwise stated, the experiment was conducted in a multi-well format, with incubation and induction overnight at 37 °C.

A.3.6 Biosensing tests in clinically relevant samples

The VAI-sensing ELM was also used to detect PAI in supernatants of *P. aeruginosa* isolates or bronchial aspirates. Clinical isolates of *P. aeruginosa*, collected from patients affected by cystic fibrosis (Padua University

Hospital), were cultured in LB medium for 24 h (37 °C, 220 rpm), cells were spun down and supernatants were 0.2 μm filtered. Bronchial aspirate samples from patients (Padua University Hospital) affected by Gram positive or Gram negative bacterial infections (including *P. aeruginosa*) were diluted at a 1:1 ratio with sputasol (Oxoid), centrifuged and the supernatants collected. Supernatants of clinical isolates or bronchial aspirate samples were stored at -20 °C until further use. Biosensing experiments were carried out by pipetting 200 μl of samples on ELMs with a cut piece of LB agar providing additional nutrients and incubating these structures at 37 °C overnight. Bronchial aspirate samples with no *P. aeruginosa* were tested with and without spiked PAI at 400 nM.

When indicated, structures printed at day 0 were stored at 2-8 °C on LB agar plate for the specified time until further use

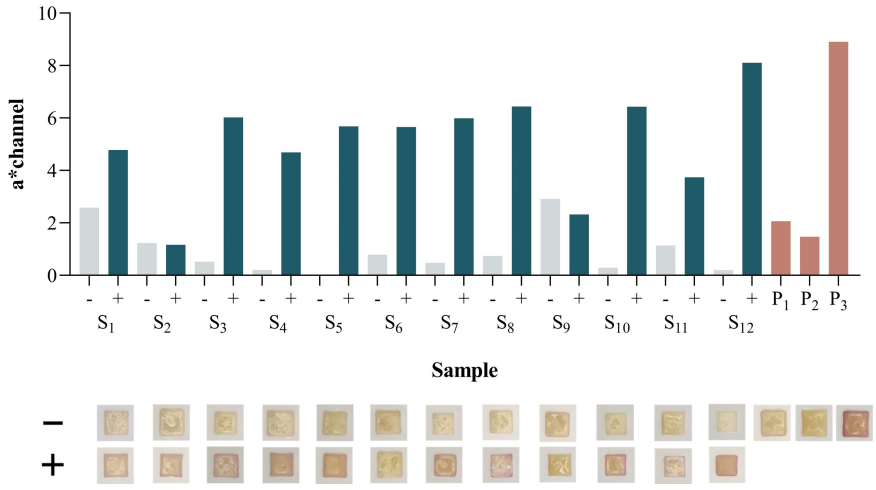

Figure A.2: ELM response upon PAI sensing from bronchial aspirate samples from patients. The S1-S3 samples contained non-*P. aeruginosa* Gram negative bacteria; the S4 sample did not yield any detectable CFU; the S5-S12 samples contained Gram positive bacteria; the P1-P3 contained *P. eruginosa*. ELMs were printed at day 0, moved to LB agar, and stored at 2-8 °C for less than 15 days. Then, LB agar was cut, the ELMs+LB agar pieces were moved to a 6-well plate, and a 200 μl drop of bronchial aspirate sample was applied; ELMs were incubated overnight at 37 °C and then evaluated. The a* values are reported to quantify the red pigmentation and the corresponding pictures are shown below (N=1)

A.4 Image analysis

A.4.1 Shape fidelity of printed ELMs

Images of 20 x 20 mm grid structures with different height and distance between filaments were analyzed using ImageJ to assess the fidelity of strand size and distance between the filaments in terms of coefficient of variation (CV) in at least 30 values measured from the same structure and different structures. The fidelity of square pores in grids was quantified by computing, where L and A indicate pore perimeter and area, respectively. The Pr index is 1 for square pores, lower than 1 for circular pores (0.785 for perfect circles), and higher than 1 for irregularly gelated structures.

A.4.2 Separation of strains in multi-bioink ELMs

Analysis of fluorescence microscopy pictures with ImageJ was used to measure separation and cross-contamination between adjacent sections of the same material, composed of different strains expressing red and green fluorescent proteins.

A.4.3 Quantification of red pigmentation

Images of biosensing patches were cropped and the intensity of red pigmentation was computed using the CIELAB system, a color space based on three opponent color channels, namely black/white (L*), red/green (a*), and yellow/blue (b*). The a* values were quantified using a custom Python script (functions from the skimage and cv2 modules) and were used to compare the intensity level of red in the red/green channel coordinates among different images. The a* values shown in graphs are relative to pictures acquired under similar illumination conditions, except for the experiments with bronchial aspirates that were carried out in a different institute and a different acquisition setup was adopted.

Data of red pigmentation intensity are reported with the specified number of replicates carried out using different bacterial culture batches prepared in the same day and in different days, as indicated. Batch-to-batch and day-to-day variability in the VAI-sensing ELM response were quantified in terms of average CV across all the VAI concentration conditions.

When indicated, red color data derived from pictures were confirmed by red fluorescence measurements of ELMs that were cut and transferred into individual wells of 96-well plates. Red fluorescence was acquired through the

microplate reader using 3-by-3 square-filled acquisitions per well (RFP gain = 30) and averaging the obtained values.

A.4.4 Statistical analysis

Unpaired t-test was used to evaluate statistical differences between two samples using Microsoft Excel. Two-way ANOVA with interactions was adopted to evaluate the impact of two variables (namely, temperature and presence of agar medium) in the same experimental study, using the Matlab R2017b (MathWorks, Natick, US) anovan function. Pearson correlation coefficient (r) and its relative p-value (p) were computed with the Matlab corrcoef function. A p-value cutoff of 0.05 was adopted to evaluate statistical significance.

Appendix B

Second Appendix

Appendix B comprises the materials and methods used in the work shown in Chapter 4.

B.1 Strain construction and in liquid assays

B.1.1 Bacterial cultivation conditions

Cyanobacterial cultures of the strain *Synechococcus elongatus* UTEX 2973 were grown in BG11 liquid medium at 37 °C, 150 mol photons m2 s1 light, and 0.5% CO2 in a Percival Scientific growth chamber with either constant 200 rpm shaking or on plates. For the engineered strains, appropriate antibiotics were applied to BG11 agar plates or liquid medium (kanamycin 50 μg/mL; gentamicin 15 μg/mL; spectinomycin 100 μg/mL). For the experiments related to surface display and protein secretion, the cyanobacterial cultures were grown overnight, the following day diluted to reach OD_{750} of 0.1, and then grown two days before proceeding with the respective assay.

B.1.2 Cloning

Cloning involved plasmid construction, accomplished using Golden gate (NEB, Golden Gate Assembly Mix) or Gibson assembly (NEB, Gibson Assembly Cloning Kit) techniques. Plasmids were first transformed into 10-beta competent *E. coli* cells, and after confirmation of the correct sequencing transformed into WM6026 competent cells suitable for conjugation, to transfer the plasmid into UTEX 2973. For all the experiments related to

protein secretion and surface display of foreigner targets, genes were first codon optimized (using the CDS calculator software, from De Novo DNA).

Gene knockout plasmids were constructed by cloning 1 kilobase fragments upstream and downstream of target genes into a non replicative plasmid flanking antibiotic resistance selectable markers.

B.1.3 S-layer proteins screened

The three SLP candidates screened in this work, comprising their name, Uniprot accession, and length.

Protein	**Primary accession**	**AA length**
Integrins alpha chain	Q31NK2	1434
VCBS	Q31NQ2	610
Calcium-binding protein	Q31PT7	319

B.1.4 Luminescence detection

Luminenescent activity, both in the supernatant or in the cell surface, was measured using the Nano-Glo HiBiT kit (Promega). The assay was performed following the Promega procedure, adding 100 μl of Nano-Glo HiBiT Extracellular Reagent to 100 μl of culture medium (i.e., supernatant for secreted proteins or cell culture for surface displayed proteins) in 96-well plates, gently pipetting.

B.1.5 Desiccation assay

The desiccation protocol was designed to mimic dehydration conditions. Initially, liquid cultures of the strain UTEX 2973 and the engineered versions were grown for two overnights, in standard conditions, on 6-well plates. The cells were then transferred into 2 ml eppendorf tubes, pelleted by centrifugation to remove the supernatant. Subsequently, the pellets were subjected to a five-day dehydration period inside a desiccator chamber, which maintained a low-humidity environment to ensure thorough desiccation. Once the dehydration period was complete, the cell pellets were rehydrated by resuspending them in PBS, and the survival of the cells was evaluated using CFU counts multiplied by the dilution factor. The CFU/ml provided a quantitative measure of cell viability by comparing the number of surviving cells before and after the desiccation process, with the results expressed as a percentage of survival.

B.1.6 Carbonic anhydrase log

The carbonic anhydrase library used in this work, comprising the label used in this thesis, specie's name, theoretically pI (using Expasy, operated by the SIB Swiss Institute of Bioinformatics), and AA length.

ID	Species	pI	AA len
1080	*Ascaris suum* (Pig roundworm)	5.76	115
1081	*Tetradesmus obliquus* (Green alga)	5.90	548
1082	*Camelus dromedarius* (Dromedary)	7.80	265
1083	*Gossypium barbadense* (Sea-island cotton)	5.95	274
1084	*Ovis aries* (Sheep)	5.93	150
1085	*Arion vulgaris* (land snail)	5.95	563
1086	*Carassius auratus* (Goldfish)	8.76	260
1087	*Gossypium tomentosum* (Hawaiian cotton)	6.23	274
1088	*Aphanomyces stellatus* (water mold)	6.17	152
1089	*Paramormyrops kingsleyae* (fish)	4.60	260
1090	*Taeniopygia guttata* (Zebra finch)	8.90	261
1091	*Oryza nivara* (Indian wild rice)	8.36	275
1092	Mytilus edulis (Blue mussel)	5.74	194
1093	*Sinocyclocheilus anshuiensis* (fish)	5.13	261
1094	*Pipistrellus kuhlii* (Kuhl's pipistrelle)	8.54	264
1095	*Sesamum indicum* (Oriental sesame)	8.78	274
1096	*Trichinella nativa* (nematode)	5.86	224
1097	*Danaus plexippus* (monarch butterfly)	6.05	265
1098	*Medicago truncatula* (Barrel medic)	4.52	274
1099	*Leersia perrieri* (cutgrass)	8.87	274
1100	*Rhodnius prolixus* (Triatomid bug)	6.08	272
1101	*Trichinella papuae* (roundworm)	6.08	265
1102	*Eucalyptus grandis* (Flooded gum)	5.52	274
1103	*Actinidia chinensis var. chinensis* (Chinese soft-hair kiwi)	8.71	273
1104	*Pocillopora damicornis* (Cauliflower coral)	5.90	314
1105	*Cuculus canorus* (common cuckoo)	7.21	264
1106	*Cinara cedri*	5.90	275
1107	*Bovine*	6.59	261
1108	*Blattella germanica* (German cockroach)	5.80	433
1110	*Theobroma cacao* (Cocoa)	6.01	275
1111	*Thiomicrospira crunogena*	5.05	298
1150	*Ornithorhynchus anatinus* (Duckbill platypus)	5.94	349
1151	*Carnobacterium iners*	8.39	231
1152	*Anthurium amnicola*	5.43	267
1153	*Gammaproteobacteria bacterium*	5.92	252
1154	*Drosophila virilis* (Fruit fly)	5.40	330
1155	*Aphis craccivora* (Cowpea aphid)	8.15	381
1156	*Triplophysa tibetana*	6.76	253
1157	*Amphibalanus amphitrite* (Striped barnacle)	11.00	298
1158	*Gammaproteobacteria*	5.11	238
1159	*Sinocyclocheilus anshuiensis*	5.13	261
2077	*Zizania palustris* (Northern wild rice)	9.50	280
2078	*Sinocyclocheilus grahami*	8.66	289
2079	*Hermetia illucens* (Black soldier fly)	5.83	272
2080	*Triticum aestivum* (Wheat)	8.55	278
2082	*Nasonia vitripennis* (Parasitic wasp)	7.17	313
2083	*Miscanthus lutarioriparius*	8.36	292
2086	*Oryza meyeriana var. granulata*	9.49	275
2087	*Rhynchophorus ferrugineus* (Red palm weevil)	6.07	266
2088	*Zea mays* (Maize)	8.89	308
2090	*Scleropages formosus* (Asian bonytongue)	4.62	260
2093	*Plutella xylostella* (Diamondback moth)	8.60	301
2094	*Sparus aurata* (Gilthead sea bream)	5.30	273
2095	*Operophtera brumata* (Winter moth)	7.11	219
2096	*Stylophora pistillata* (Smooth cauliflower coral)	9.57	628
2101	*Halalkalibacter nanhaiisediminis*	4.38	274
2107	MPNN_1	5.18	275
2108	MPNN_2	5.63	275
2111	MPNN_3	5.41	275
2112	MPNN_4	5.76	275
2113	MPNN_5	6.24	275
2114	MPNN_6	5.63	275

Table B.1: Carbonic anhydrase library. For each enzyme label, organism's name, pI and length (AA sequence) are reported.

B.1.7 Carbonic anhydrase activity assay

Carbonic anhydrase activity in the supernatant was measured using an Carbonic Anhydrase colorimetric assay kit (Abcam). The supernatant sample was prepared for the assay following the Abcam procedure in a 96-well plate.

B.2 Cyanobacteria living materials

B.2.1 Preparation of bricks

To begin the preparation, BG11 medium is added to a Falcon tube and placed in a water bath heated to 60 °C. The medium is left in the bath for approximately 5 to 10 minutes to allow it to warm up. Afterward, 0.1 M bicarbonate is added to the solution, ensuring it is fully incorporated into the medium. Following this, hydrochloric acid (HCl) is added carefully to adjust the pH of the solution until it reaches a value of 7.5, the desired neutral condition. Next, gelatin (5%) is added to the mixture, and the tube is vortexed to ensure thorough mixing. Following this step, sodium alginate (also at 5%) is introduced into the solution, and the tube is vortexed once more. Sodium alginate tends to form clumps, so a spatula is used to carefully break up any clumps that may have formed. It's crucial to remove all clumps at this stage before moving on to centrifugation. The mixture is then centrifuged for 5 minutes at a speed of 2500 rpm at room temperature. After centrifugation, the tube is removed, and an appropriate volume of cyanobacteria culture is added, where the optical density (OD_{720}) is maintained at 0.3. The culture is mixed into the solution using a spatula, ensuring an even distribution throughout. At this point, the hydrogel is ready to be combined with sand. In the next phase, the prepared hydrogel is mixed with sand in a weigh tray or a similar container. To this mixture, a 0.01 M solution of calcium chloride is added, and the combination is mixed thoroughly to ensure that the calcium chloride is distributed as evenly as possible throughout the sand and hydrogel. This step is important to promote homogeneity in the final product. Once mixed, the hydrogel-sand combination is poured into a mold. Inside the mold, the mixture is gently stirred or mixed again to ensure the hydrogel is spread evenly throughout the sand. The mold is then placed in a refrigerator or cold room, set at 4 °C, for 5 minutes to allow the mixture to set. After the 5-minute period, the brick is removed from the mold and immediately placed into a 2% calcium chloride solution. The brick should remain in the solution for at least 5 minutes, although the exact time may vary

depending on the size of the brick. This step allows for cross-linking to occur, which is critical for stabilizing the structure. Finally, after the cross-linking process, the brick is removed and placed in a clear container and transferred to an incubator. The conditions are set to provide 150 μmol photons m2 s1 light, and 0.5% CO2. The brick is then left to dry under these controlled conditions.

B.2.2 Mechanical testing

Mechanical testing on cyanobacteria based bricks was performed at the MIT Civil and Environmental Engineering Department (Massachusetts Institute of Technology). The Instron model 1331 was used for the uniaxial compression test of both wild type and abiotic control.

B.2.3 Scanning electron microscopy and energy dispersive X-ray spectroscopy analysis

Scanning electron microscopy (SEM) imaging and energy dispersive X-ray spectroscopy (EDS) analysis were performed at the Boston Electron Microscopy Center (Northeastern University). The S4800 Hitachi FE-SEM with EDAX, and 108auto Cressington Sputter Coater with Pt target (40 sec, 20 mA) were used for study the chemistry of possible precipitates and the surface morfology of cyanobacteria based bricks. A piece of the brick was placed on a 2.5 cm Al stub with a double-sided C adhesive tab. Graphite adhesive paste was added to the edges to increase conductivity. To eliminate charging effects in the SEM, a thin layer (about 5 nm) of Pt was sputtered on the surface of the samples.

B.3 Transmission electron microscopy

Transmission electron microscopy (TEM) imaging was performed at the HMS Electron Microscopy Core Facility (Harvard Medical School). TEM analysis of cyanobacteria, both the wild-type and the SLP knockout strains, was conducted to assess structural differences on their outer layer. Cells were fixed using a mixture of 1.25% formaldehyde, 2.5% glutaraldehyde, and 0.03% picric acid in 0.1 M sodium cacodylate buffer (pH 7.4). The fixative was added at a 1:1 ratio to the bacterial cultures, and then pelleted by centrifugation at 3000 rpm for 3 minutes, followed by an additional 1 hour incubation at RT.

Bibliography

[1] Barbara Hobom. Surgery of genes. at the doorstep of synthetic biology. *Medizin. Klinik*, 75:14–21, 1980.

[2] D Ewen Cameron, Caleb J Bashor, and James J Collins. A brief history of synthetic biology. *Nature Reviews Microbiology*, 12(5):381–390, 2014.

[3] Kathryn L Garner. Principles of synthetic biology. *Essays in biochemistry*, 65(5):791–811, 2021.

[4] Timothy S Gardner, Charles R Cantor, and James J Collins. Construction of a genetic toggle switch in escherichia coli. *Nature*, 403(6767):339–342, 2000.

[5] Michael B Elowitz and Stanislas Leibler. A synthetic oscillatory network of transcriptional regulators. *Nature*, 403(6767):335–338, 2000.

[6] Shimyn Slomovic, Keith Pardee, and James J Collins. Synthetic biology devices for in vitro and in vivo diagnostics. *Proceedings of the National Academy of Sciences*, 112(47):14429–14435, 2015.

[7] Ethan M Jones, John P Marken, and Pamela A Silver. Synthetic microbiology in sustainability applications. *Nature Reviews Microbiology*, 22(6):345–359, 2024.

[8] Bradley Walters Biggs, Chin Giaw Lim, Kristen Sagliani, Smriti Shankar, Gregory Stephanopoulos, Marjan De Mey, and Parayil Kumaran Ajikumar. Overcoming heterologous protein interdependency to optimize p450-mediated taxol precursor synthesis in escherichia coli. *Proceedings of the National Academy of Sciences*, 113(12):3209–3214, 2016.

[9] Shota Atsumi, Wendy Higashide, and James C Liao. Direct photosynthetic recycling of carbon dioxide to isobutyraldehyde. *Nature biotechnology*, 27(12):1177–1180, 2009.

[10] Ilenne Del Valle, Emily M Fulk, Prashant Kalvapalle, Jonathan J Silberg, Caroline A Masiello, and Lauren B Stadler. Translating new synthetic biology advances for biosensing into the earth and environmental sciences. *Frontiers in microbiology*, 11:618373, 2021.

[11] SM Tauriainen, MPJ Virta, and MT Karp. Detecting bioavailable toxic metals and metalloids from natural water samples using luminescent sensor bacteria. *Water Research*, 34(10):2661–2666, 2000.

[12] Rosa L Vincent, Candice R Gurbatri, Fangda Li, Ana Vardoshvili, Courtney Coker, Jongwon Im, Edward R Ballister, Mathieu Rouanne, Thomas Savage, Kenia de Los Santos-Alexis, et al. Probiotic-guided car-t cells for solid tumor targeting. *Science*, 382(6667):211–218, 2023.

[13] Ross Cloney. Automating genetic circuit design. *Nature Reviews Genetics*, 17(6):314–315, 2016.

[14] Subhayu Basu, Rishabh Mehreja, Stephan Thiberge, Ming-Tang Chen, and Ron Weiss. Spatiotemporal control of gene expression with pulse-generating networks. *Proceedings of the National Academy of Sciences*, 101(17):6355–6360, 2004.

[15] Stephanie K Aoki, Gabriele Lillacci, Ankit Gupta, Armin Baumschlager, David Schweingruber, and Mustafa Khammash. A universal biomolecular integral feedback controller for robust perfect adaptation. *Nature*, 570(7762):533–537, 2019.

[16] Shijing Chen, Xiaolin Chen, Hongfei Su, Mingzhang Guo, and Huilin Liu. Advances in synthetic-biology-based whole-cell biosensors: Principles, genetic modules, and applications in food safety. *International Journal of Molecular Sciences*, 24(9):7989, 2023.

[17] Maggie Hicks, Till T Bachmann, and Baojun Wang. Synthetic biology enables programmable cell-based biosensors. *ChemPhysChem*, 21(2):132–144, 2020.

[18] Andrea Muras, Paz Otero-Casal, Vanessa Blanc, and Ana Otero. Acyl homoserine lactone-mediated quorum sensing in the oral cavity: a paradigm revisited. *Scientific reports*, 10(1):9800, 2020.

[19] Pradeep K Singh, Amy L Schaefer, Matthew R Parsek, Thomas O Moninger, Michael J Welsh, and EP Greenberg. Quorum-sensing signals indicate that cystic fibrosis lungs are infected with bacterial biofilms. *Nature*, 407(6805):762–764, 2000.

[20] Nilesh Raut, Patrizia Pasini, and Sylvia Daunert. Deciphering bacterial universal language by detecting the quorum sensing signal, autoinducer-2, with a whole-cell sensing system. *Analytical chemistry*, 85(20):9604–9609, 2013.

[21] Peter Q Nguyen, Luis R Soenksen, Nina M Donghia, Nicolaas M Angenent-Mari, Helena de Puig, Ally Huang, Rose Lee, Shimyn Slomovic, Tommaso Galbersanini, Geoffrey Lansberry, et al. Wearable materials with embedded synthetic biology sensors for biomolecule detection. *Nature Biotechnology*, 39(11):1366–1374, 2021.

[22] Cristina V Cardemil, Dana R Smulski, Robert A LaRossa, and Amy Cheng Vollmer. Bioluminescent escherichia coli strains for the quantitative detection of phosphate and ammonia in coastal and suburban watersheds. *DNA and cell biology*, 29(9):519–531, 2010.

[23] Ying Wu, Chien-Wei Wang, Dong Wang, and Na Wei. A whole-cell biosensor for point-of-care detection of waterborne bacterial pathogens. *ACS synthetic biology*, 10(2):333–344, 2021.

[24] Manuel Schaffner, Patrick A Rühs, Fergal Coulter, Samuel Kilcher, and André R Studart. 3d printing of bacteria into functional complex materials. *Science advances*, 3(12):eaao6804, 2017.

[25] Lina M González, Nikita Mukhitov, and Christopher A Voigt. Resilient living materials built by printing bacterial spores. *Nature chemical biology*, 16(2):126–133, 2020.

[26] Debika Datta, Elliot L Weiss, Daniel Wangpraseurt, Erica Hild, Shaochen Chen, James W Golden, Susan S Golden, and Jonathan K Pokorski. Phenotypically complex living materials containing engineered cyanobacteria. *Nature Communications*, 14(1):4742, 2023.

[27] Shimshon Belkin, Sharon Yagur-Kroll, Yossef Kabessa, Victor Korouma, Tali Septon, Yonatan Anati, Cheinat Zohar-Perez, Zahi Rabinovitz, Amos Nussinovitch, and Aharon J Agranat. Remote detection of buried landmines using a bacterial sensor. *Nature biotechnology*, 35(4):308–310, 2017.

[28] Tzu-Chieh Tang, Bolin An, Yuanyuan Huang, Sangita Vasikaran, Yanyi Wang, Xiaoyu Jiang, Timothy K Lu, and Chao Zhong. Materials design by synthetic biology. *Nature Reviews Materials*, 6(4):332–350, 2021.

[29] Junning Ma, Boris Veltman, Zipora Tietel, Leah Tsror, Yang Liu, and Evgeni Eltzov. Monitoring of infection volatile markers using cmos-based luminescent bioreporters. *Talanta*, 219:121333, 2020.

[30] Taylor Rycroft, Kerry Hamilton, Charles N Haas, and Igor Linkov. A quantitative risk assessment method for synthetic biology products in the environment. *Science of the Total Environment*, 696:133940, 2019.

[31] Patricia A Sobecky, Mark A Schell, Mary Ann Moran, and Robert E Hodson. Impact of a genetically engineered bacterium with enhanced alkaline phosphatase activity on marine phytoplankton communities. *Applied and environmental microbiology*, 62(1):6–12, 1996.

[32] Anna M Hartig, Wentao Dai, Ke Zhang, Krisha Kapoor, Austin G Rottinghaus, Tae Seok Moon, and Kimberly M Parker. Influence of environmental conditions on the escape rates of biocontained genetically engineered microbes. *Environmental Science & Technology*, 2024.

[33] Matthew B Amrofell, Sunaina Rengarajan, Steven T Vo, Erick S Ramirez Tovar, Larissa LoBello, Gautam Dantas, and Tae Seok Moon. Engineering e. coli strains using antibiotic-resistance-gene-free plasmids. *Cell Reports Methods*, 3(12), 2023.

[34] Marcus Dröge, Alfred Pühler, and Werner Selbitschka. Horizontal gene transfer as a biosafety issue: a natural phenomenon of public concern. *Journal of biotechnology*, 64(1):75–90, 1998.

[35] Sara Molinari, Robert F Tesoriero, and Caroline M Ajo-Franklin. Bottom-up approaches to engineered living materials: Challenges and future directions. *Matter*, 4(10):3095–3120, 2021.

[36] Bolin An, Yanyi Wang, Yuanyuan Huang, Xinyu Wang, Yuzhu Liu, Dongmin Xun, George M Church, Zhuojun Dai, Xiao Yi, Tzu-Chieh Tang, et al. Engineered living materials for sustainability. *Chemical Reviews*, 123(5):2349–2419, 2022.

[37] Rabia Omer, Muhammad Zubair Mohsin, Ali Mohsin, Bilal Sajid Mushtaq, Xumeng Huang, Meijin Guo, Yingping Zhuang, and Jiaofang Huang. Engineered bacteria-based living materials for biother-

apeutic applications. *Frontiers in Bioengineering and Biotechnology*, 10:870675, 2022.

[38] Daniel J Mandell, Marc J Lajoie, Michael T Mee, Ryo Takeuchi, Gleb Kuznetsov, Julie E Norville, Christopher J Gregg, Barry L Stoddard, and George M Church. Biocontainment of genetically modified organisms by synthetic protein design. *Nature*, 518(7537):55–60, 2015.

[39] Yangteng Ou, Shixiang Cao, Yang Zhang, Hongjia Zhu, Chengzhi Guo, Wei Yan, Fengxue Xin, Weiliang Dong, Yanli Zhang, Masashi Narita, et al. Bioprinting microporous functional living materials from protein-based core-shell microgels. *Nature Communications*, 14(1):322, 2023.

[40] Tzu-Chieh Tang, Eléonore Tham, Xinyue Liu, Kevin Yehl, Alexis J Rovner, Hyunwoo Yuk, Cesar de la Fuente-Nunez, Farren J Isaacs, Xuanhe Zhao, and Timothy K Lu. Hydrogel-based biocontainment of bacteria for continuous sensing and computation. *Nature Chemical Biology*, 17(6):724–731, 2021.

[41] Shuaiqi Guo, Emilien Dubuc, Yahav Rave, Mick Verhagen, Simone AE Twisk, Tim Van Der Hek, Guido JM Oerlemans, Maxime CM van den Oetelaar, Laura S Van Hazendonk, Mariska Bruls, et al. Engineered living materials based on adhesin-mediated trapping of programmable cells. *ACS synthetic biology*, 9(3):475–485, 2020.

[42] Xinyue Liu, Tzu-Chieh Tang, Eléonore Tham, Hyunwoo Yuk, Shaoting Lin, Timothy K Lu, and Xuanhe Zhao. Stretchable living materials and devices with hydrogel–elastomer hybrids hosting programmed cells. *Proceedings of the National Academy of Sciences*, 114(9):2200–2205, 2017.

[43] Francesca Volpetti, Ekaterina Petrova, and Sebastian J Maerkl. A microfluidic biodisplay. *ACS synthetic biology*, 6(11):1979–1987, 2017.

[44] Wil V Srubar. Engineered living materials: taxonomies and emerging trends. *Trends in biotechnology*, 39(6):574–583, 2021.

[45] Pierre Friedlingstein, Michael O'sullivan, Matthew W Jones, Robbie M Andrew, Dorothee CE Bakker, Judith Hauck, Peter Landschützer, Corinne Le Quéré, Ingrid T Luijkx, Glen P Peters, et al. Global carbon budget 2023. *Earth System Science Data*, 15(12):5301–5369, 2023.

[46] Isabella M Goodchild-Michelman, George M Church, Max G Schubert, and Tzu-Chieh Tang. Light and carbon: Synthetic biology toward new cyanobacteria-based living biomaterials. *Materials Today Bio*, 19:100583, 2023.

[47] National Research Council, Division on Earth, Life Studies, Board on Life Sciences, Board on Chemical Sciences, Committee on Industrialization of Biology, and A Roadmap to Accelerate the Advanced Manufacturing of Chemicals. *Industrialization of biology: A roadmap to accelerate the advanced manufacturing of chemicals*. National Academies Press, 2015.

[48] Jingjie Yu, Michelle Liberton, Paul F Cliften, Richard D Head, Jon M Jacobs, Richard D Smith, David W Koppenaal, Jerry J Brand, and Himadri B Pakrasi. Synechococcus elongatus utex 2973, a fast growing cyanobacterial chassis for biosynthesis using light and co2. *Scientific reports*, 5(1):8132, 2015.

[49] Gerald M Cherf and Jennifer R Cochran. Applications of yeast surface display for protein engineering. *Yeast Surface Display: Methods, Protocols, and Applications*, pages 155–175, 2015.

[50] Catherine J Hutchings and Aaron K Sato. Phage display technology and its impact in the discovery of novel protein-based drugs. *Expert Opinion on Drug Discovery*, pages 1–29, 2024.

[51] Valencio Salema and Luis Ángel Fernández. Escherichia coli surface display for the selection of nanobodies. *Microbial biotechnology*, 10(6):1468–1484, 2017.

[52] Mateja Lozančić, Amir Sk. Hossain, Vladimir Mrša, and Renata Teparić. Surface display—an alternative to classic enzyme immobilization. *Catalysts*, 9(9):728, 2019.

[53] Jiaming Yang, Kui Huang, Xiaomin Xu, Yangli Miao, Ying Lin, and Shuangyan Han. Cell surface display of thermomyces lanuginosus lipase in pichia pastoris. *Frontiers in bioengineering and biotechnology*, 8:544058, 2020.

[54] Derek T Fedeson and Daniel C Ducat. Cyanobacterial surface display system mediates engineered interspecies and abiotic binding. *ACS Synthetic Biology*, 6(2):367–374, 2017.

[55] Ivana Cengic, Mathias Uhlén, and Elton P Hudson. Surface display of small affinity proteins on synechocystis sp. strain pcc 6803 mediated by fusion to the major type iv pilin pila1. *Journal of Bacteriology*, 200(16):10–1128, 2018.

[56] Christoph Trautner and Wim FJ Vermaas. The sll1951 gene encodes the surface layer protein of synechocystis sp. strain pcc 6803. *Journal of bacteriology*, 195(23):5370–5380, 2013.

[57] Rachna Agarwal, Julian P Whitelegge, Sanjay Saini, and Amit Prakash Shrivastav. The s-layer biogenesis system of synechocystis 6803: role of sll1180 and sll1181 (e. coli hlyb and hlyd analogs) as type-i secretion components for sll1951 export. *Biochimica et Biophysica Acta (BBA)-Biomembranes*, 1860(7):1436–1446, 2018.

[58] Lisa Yun, Jonathan K Sakkos, and Daniel C Ducat. Population-level heterogeneity complicates utilization of synechococcus elongatus pcc 7942 surface display platforms. *Micropublication Biology*, 2024, 2024.

[59] Olivia Spitz, Isabelle N Erenburg, Tobias Beer, Kerstin Kanonenberg, I Barry Holland, and Lutz Schmitt. Type i secretion systems—one mechanism for all? *Microbiology spectrum*, 7(2):10–1128, 2019.

[60] Freya J Hodges, L Torres Von Vergel, Adam F Cunningham, Ian R Henderson, and Christopher Icke. Redefining the bacterial type i protein secretion system. *Advances in Microbial Physiology*, 82:155–204, 2023.

[61] Ivaylo Gentschev, Guido Dietrich, and Werner Goebel. The e. coli α-hemolysin secretion system and its use in vaccine development. *Trends in microbiology*, 10(1):39–45, 2002.

[62] Uwe B Sleytr, Bernhard Schuster, Eva-Maria Egelseer, and Dietmar Pum. S-layers: principles and applications. *FEMS microbiology reviews*, 38(5):823–864, 2014.

[63] Irena Linhartová, Ladislav Bumba, Jiří Mašín, Marek Basler, Radim Osička, Jana Kamanová, Kateřina Procházková, Irena Adkins, Jana Hejnová-Holubová, Lenka Sadílková, et al. Rtx proteins: a highly diverse family secreted by a common mechanism. *FEMS microbiology reviews*, 34(6):1076–1112, 2010.

[64] Michael C Flickinger. Encyclopedia of industrial biotechnology: bioprocess, bioseparation, and cell technology, 7 volume set. *City: John Wiley & Sons, ISBN*, 2010.

[65] Sara Molinari, Robert F Tesoriero Jr, Dong Li, Swetha Sridhar, Rong Cai, Jayashree Soman, Kathleen R Ryan, Paul D Ashby, and Caroline M Ajo-Franklin. A de novo matrix for macroscopic living materials from bacteria. *Nature communications*, 13(1):5544, 2022.

[66] Jia-Zhong Zhang. Cyanobacteria blooms induced precipitation of calcium carbonate and dissolution of silica in a subtropical lagoon, florida bay, usa. *Scientific Reports*, 13(1):4071, 2023.

[67] Martina UE Merz. The biology of carbonate precipitation by cyanobacteria. *Facies*, 26:81–101, 1992.

[68] Xiao Wang, Xiangxin Kong, Qian Liu, Kun Li, Zaixing Jiang, Hengjun Gai, and Meng Xiao. Effect of clay minerals on carbonate precipitation induced by cyanobacterium synechococcus sp. *Microbiology Spectrum*, 11(3):e00363–23, 2023.

[69] Global status report. `https://www.unep.org/resources/report/global-status-report-buildings-and-construction`.

[70] Nina A Kamennaya, Caroline M Ajo-Franklin, Trent Northen, and Christer Jansson. Cyanobacteria as biocatalysts for carbonate mineralization. *Minerals*, 2(4):338–364, 2012.

[71] CM Heveran, SL Williams, J Qiu, SM Cook, JC Cameron, and WV Srubar III. Biomineralization and successive regeneration of engineered living building materials. matter 2 (2): 481–494, 2020.

[72] Olena Reinhardt, Stephanie Ihmann, Matthias Ahlhelm, and Michael Gelinsky. 3d bioprinting of mineralizing cyanobacteria as novel approach for the fabrication of living building materials. *Frontiers in Bioengineering and Biotechnology*, 11:1145177, 2023.

[73] Rollin J Jones, Elizabeth A Delesky, Sherri M Cook, Jeffrey C Cameron, Mija H Hubler, and Wil V Srubar III. Engineered living materials for construction. In *Engineered Living Materials*, pages 187–216. Springer, 2022.

[74] Francesca Usai, Giada Loi, Franca Scocozza, Massimo Bellato, Ignazio Castagliuolo, Michele Conti, and Lorenzo Pasotti. Design and biofabrication of bacterial living materials with robust and multiplexed biosensing capabilities. *Materials Today Bio*, 18:100526, 2023.

[75] Xueli Liu, Kaixin Tang, and Jinlu Hu. Application of cyanobacteria as chassis cells in synthetic biology. *Microorganisms*, 12(7):1375, 2024.

[76] D Ewen Cameron and James J Collins. Tunable protein degradation in bacteria. *Nature biotechnology*, 32(12):1276–1281, 2014.

[77] Elizabeth J Clarke and Christopher A Voigt. Characterization of combinatorial patterns generated by multiple two-component sensors in e. coli that respond to many stimuli. *Biotechnology and bioengineering*, 108(3):666–675, 2011.

[78] Katie J Denby, Jeffrey Iwig, Claudine Bisson, Jodie Westwood, Matthew D Rolfe, Svetlana E Sedelnikova, Khadine Higgins, Michael J Maroney, Patrick J Baker, Peter T Chivers, et al. The mechanism of a formaldehyde-sensing transcriptional regulator. *Scientific reports*, 6(1):38879, 2016.

[79] William R Farmer and James C Liao. Acetate-inducible protein overexpression from the glnap2 promoter of escherichia coli. *Biotechnology and bioengineering*, 75(5):504–509, 2001.

[80] Felix Moser, Amin Espah Borujeni, Amar N Ghodasara, Ewen Cameron, Yongjin Park, and Christopher A Voigt. Dynamic control of endogenous metabolism with combinatorial logic circuits. *Molecular systems biology*, 14(11):e8605, 2018.

[81] Adam Z Rosenthal, Youngbae Kim, and Jay D Gralla. Regulation of transcription by acetate in escherichia coli: in vivo and in vitro comparisons. *Molecular microbiology*, 68(4):907–917, 2008.

[82] Hsia-Yin Lin, Peggy J Bledsoe, and Valley Stewart. Activation of yeary-oag operon transcription by the nitrate-responsive regulator narl is independent of oxygen-responsive regulator fnr in escherichia coli k-12. *Journal of bacteriology*, 189(21):7539–7548, 2007.

[83] Matthew I Hutchings, Neeraj Mandhana, and Stephen Spiro. The norr protein of escherichia coli activates expression of the flavorubredoxin gene norv in response to reactive nitrogen species. *Journal of Bacteriology*, 184(16):4640–4643, 2002.

[84] Hideo Shinagawa, Kozo Makino, Atsuo Nakata, and S Brenner. Regulation of the pho regulon in escherichia coli k-12: genetic and physiological regulation of the positive regulatory gene phob. *Journal of molecular biology*, 168(3):477–488, 1983.

[85] Christina Walters, Daniel Ballesteros, and Veronica A Vertucci. Structural mechanics of seed deterioration: standing the test of time. *Plant Science*, 179(6):565–573, 2010.

[86] MD Hailstones and MT Smith. Thermally-derived volatile aldehydes in relation to seed viability in soybean seeds. *Seed Science and Technology,*, 1989.

[87] Sara Mira, Lisa M Hill, M Elena González-Benito, Miguel Angel Ibáñez, and Christina Walters. Volatile emission in dry seeds as a way to probe chemical reactions during initial asymptomatic deterioration. *Journal of Experimental Botany*, 67(6):1783–1793, 2016.

[88] AK Bilal, M Adnan, FU Rehman, A Hasnain, M Usman, MS Javed, A Aziz, and R Ahmad. Role of silage in agriculture: A review. *Green Rep*, 2:9–12, 2021.

[89] Frank Driehuis. Silage and the safety and quality of dairy foods: a review. *Agricultural and food science*, 22(1):16–34, 2013.

[90] Brandon Wilbanks and Cong T Trinh. Comprehensive characterization of toxicity of fermentative metabolites on microbial growth. *Biotechnology for biofuels*, 10:1–11, 2017.

[91] R Kyle Bennett, Gwendolyn J Gregory, Jacqueline E Gonzalez, Jie Ren Gerald Har, Maciek R Antoniewicz, and Eleftherios T Papoutsakis. Improving the methanol tolerance of an escherichia coli methylotroph via adaptive laboratory evolution enhances synthetic methanol utilization. *Frontiers in Microbiology*, 12:638426, 2021.

[92] Daisuke Hagiwara, Masahito Sugiura, Taku Oshima, Hirotada Mori, Hirofumi Aiba, Takafumi Yamashino, and Takeshi Mizuno. Genome-wide analyses revealing a signaling network of the rcsc-yojn-rcsb phosphorelay system in escherichia coli. *Journal of bacteriology*, 185(19):5735–5746, 2003.

[93] Deenah Osman, Cecilia Piergentili, Junjun Chen, Lucy N Sayer, Isabel Usón, Thomas G Huggins, Nigel J Robinson, and Ehmke Pohl. The effectors and sensory sites of formaldehyde-responsive regulator frmr and

metal-sensing variant. *Journal of Biological Chemistry*, 291(37):19502–19516, 2016.

[94] PR Yaashikaa, P Senthil Kumar, and Sunita Varjani. Valorization of agro-industrial wastes for biorefinery process and circular bioeconomy: A critical review. *Bioresource Technology*, 343:126126, 2022.

[95] Eleni Anna Economou, Georgia Dimitropoulou, Nikoleta Prokopidou, Ioanna Dalla, and Themistoklis Sfetsas. Anaerobic digestion remediation in three full-scale biogas plants through supplement additions. *Methane*, 2(3):265–278, 2023.

[96] Alexander J Ninfa and Boris Magasanik. Covalent modification of the glng product, nri, by the glnl product, nrii, regulates the transcription of the glnalg operon in escherichia coli. *Proceedings of the National Academy of Sciences*, 83(16):5909–5913, 1986.

[97] JUNLI Feng, MR Atkinson, W McCleary, JB Stock, BL Wanner, and AJ Ninfa. Role of phosphorylated metabolic intermediates in the regulation of glutamine synthetase synthesis in escherichia coli. *Journal of bacteriology*, 174(19):6061–6070, 1992.

[98] William R Farmer and James C Liao. Improving lycopene production in escherichia coli by engineering metabolic control. *Nature biotechnology*, 18(5):533–537, 2000.

[99] Carrie N Arnold, Justin McElhanon, Aaron Lee, Ryan Leonhart, and Deborah A Siegele. Global analysis of escherichia coli gene expression during the acetate-induced acid tolerance response. *Journal of bacteriology*, 183(7):2178–2186, 2001.

[100] Harald Weber, Tino Polen, Johanna Heuveling, Volker F Wendisch, and Regine Hengge. Genome-wide analysis of the general stress response network in escherichia coli: σs-dependent genes, promoters, and sigma factor selectivity. *Journal of bacteriology*, 187(5):1591–1603, 2005.

[101] Ying-Ying Chang and John E Cronan. Membrane cyclopropane fatty acid content is a major factor in acid resistance of escherichia coli. *Molecular microbiology*, 33(2):249–259, 1999.

[102] Ying-Ying Chang, Ai-Yu Wang, and John E Cronan Jr. Expression of escherichia coli pyruvate oxidase (poxb) depends on the sigma factor encoded by the rpos (katf) gene. *Molecular microbiology*, 11(6):1019–1028, 1994.

[103] Brice Enjalbert, Pierre Millard, Mickael Dinclaux, Jean-Charles Portais, and Fabien Létisse. Acetate fluxes in escherichia coli are determined by the thermodynamic control of the pta-acka pathway. *Scientific reports*, 7(1):42135, 2017.

[104] Janja Trček, Nuno Pereira Mira, and Laura R Jarboe. Adaptation and tolerance of bacteria against acetic acid. *Applied microbiology and biotechnology*, 99:6215–6229, 2015.

[105] Zepeng Li, Zhaosong Huang, and Pengfei Gu. Response of escherichia coli to acid stress: Mechanisms and applications—a narrative review. *Microorganisms*, 12(9):1774, 2024.

[106] Md Azahar Ali, Liang Dong, Jaspreet Dhau, Ajit Khosla, and Ajeet Kaushik. Perspective—electrochemical sensors for soil quality assessment. *Journal of The Electrochemical Society*, 167(3):037550, 2020.

[107] Amelia Bellosta-Diest, Miguel Á Campo-Bescós, Jesús Zapatería-Miranda, Javier Casalí, and Luis M Arregui. Evaluation of nitrate soil probes for a more sustainable agriculture. *Sensors*, 22(23):9288, 2022.

[108] Samuel B Adeloju et al. Progress and recent advances in phosphate sensors: A review. *Talanta*, 114:191–203, 2013.

[109] Marta C Justino, Joao B Vicente, Miguel Teixeira, and Ligia M Saraiva. New genes implicated in the protection of anaerobically grown escherichia coli against nitric oxide. *Journal of Biological Chemistry*, 280(4):2636–2643, 2005.

[110] Chrystala Constantinidou, Jon L Hobman, Lesley Griffiths, Mala D Patel, Charles W Penn, Jeffrey A Cole, and Tim W Overton. A reassessment of the fnr regulon and transcriptomic analysis of the effects of nitrate, nitrite, narxl, and narqp as escherichia coli k12 adapts from aerobic to anaerobic growth. *Journal of Biological Chemistry*, 281(8):4802–4815, 2006.

[111] Anne M Gardner and Paul R Gardner. Flavohemoglobin detoxifies nitric oxide in aerobic, but not anaerobic, escherichia coli: evidence for a novel inducible anaerobic nitric oxide-scavenging activity. *Journal of Biological Chemistry*, 277(10):8166–8171, 2002.

[112] Gottfried Unden and Johannes Bongaerts. Alternative respiratory pathways of escherichia coli: energetics and transcriptional regulation in response to electron acceptors. *Biochimica et Biophysica Acta (BBA)-Bioenergetics*, 1320(3):217–234, 1997.

[113] Charles M Moore, Michiko M Nakano, Tao Wang, Rick W Ye, and John D Helmann. Response of bacillus subtilis to nitric oxide and the nitrosating agent sodium nitroprusside. *Journal of bacteriology*, 186(14):4655–4664, 2004.

[114] Nicole M Iverson, Eric M Hofferber, and Joseph A Stapleton. Nitric oxide sensors for biological applications. *Chemosensors*, 6(1):8, 2018.

[115] BARRY L Wanner et al. Phosphorus assimilation and control of the phosphate regulon. *Escherichia coli and Salmonella: cellular and molecular biology*, 1:1357–1381, 1996.

[116] BL Wanner. Gene regulation by phosphate in enteric bacteria. *Journal of cellular biochemistry*, 51(1):47–54, 1993.

[117] Lolo Wal Marzan and Kazuyuki Shimizu. Metabolic regulation of escherichia coli and its phob and phor genes knockout mutants under phosphate and nitrogen limitations as well as at acidic condition. *Microbial Cell Factories*, 10:1–15, 2011.

[118] Antonio Rodríguez-García, Alberto Sola-Landa, Kristian Apel, Fernando Santos-Beneit, and Juan F Martín. Phosphate control over nitrogen metabolism in streptomyces coelicolor: direct and indirect negative control of glnr, glna, glnii and amtb expression by the response regulator phop. *Nucleic Acids Research*, 37(10):3230–3242, 2009.

[119] Fernando Santos-Beneit. The pho regulon: a huge regulatory network in bacteria. *Frontiers in microbiology*, 6:402, 2015.

[120] Larry Reitzer. Nitrogen assimilation and global regulation in escherichia coli. *Annual Reviews in Microbiology*, 57(1):155–176, 2003.

[121] Janice L Doull and Leo C Vining. Nutritional control of actinorhodin production by streptomyces coelicolor a3 (2): suppressive effects of nitrogen and phosphate. *Applied Microbiology and Biotechnology*, 32:449–454, 1990.

[122] Lorenzo Pasotti, Susanna Zucca, Manuel Lupotto, Maria Gabriella Cusella De Angelis, and Paolo Magni. Characterization of a synthetic

bacterial self-destruction device for programmed cell death and for recombinant proteins release. *Journal of biological engineering*, 5:1–12, 2011.

[123] Bo Ning, Tao Yu, Shengwei Zhang, Zhen Huang, Di Tian, Zhen Lin, Alex Niu, Nadia Golden, Krystle Hensley, Breanna Threeton, et al. A smartphone-read ultrasensitive and quantitative saliva test for covid-19. *Science advances*, 7(2):eabe3703, 2021.

[124] Zheng Li, Shengwei Zhang, Tao Yu, Zhiming Dai, and Qingshan Wei. Aptamer-based fluorescent sensor array for multiplexed detection of cyanotoxins on a smartphone. *Analytical chemistry*, 91(16):10448–10457, 2019.

[125] Marie K Schwinn, Thomas Machleidt, Kris Zimmerman, Christopher T Eggers, Andrew S Dixon, Robin Hurst, Mary P Hall, Lance P Encell, Brock F Binkowski, and Keith V Wood. Crispr-mediated tagging of endogenous proteins with a luminescent peptide. *ACS chemical biology*, 13(2):467–474, 2018.

[126] I Barry Holland, Mark A Blight, and Brendan Kenny. The mechanism of secretion of hemolysin and other polypeptides from gram-negative bacteria. *Journal of bioenergetics and biomembranes*, 22:473–491, 1990.

[127] Vassilis Koronakis, Eva Koronakis, and Colin Hughes. Isolation and analysis of the c-terminal signal directing export of escherichia coli hemolysin protein across both bacterial membranes. *The EMBO journal*, 8(2):595–605, 1989.

[128] Ulrich Baumann. Structure–function relationships of the repeat domains of rtx toxins. *Toxins*, 11(11):657, 2019.

[129] SYLVIE Létoffé and CECILE Wandersman. Secretion of cyaa-prtb and hlya-prtb fusion proteins in escherichia coli: involvement of the glycine-rich repeat domain of erwinia chrysanthemi protease b. *Journal of bacteriology*, 174(15):4920–4927, 1992.

[130] Ravendran Vasudevan, Grant AR Gale, Alejandra A Schiavon, Anton Puzorjov, John Malin, Michael D Gillespie, Konstantinos Vavitsas, Valentin Zulkower, Baojun Wang, Christopher J Howe, et al. Cyanogate: a modular cloning suite for engineering cyanobacteria based on the plant moclo syntax. *Plant physiology*, 180(1):39–55, 2019.

[131] Benedetto Marelli and Adam Behrens. Silk protein can extend shelf life and improve food security. *Nature Reviews Bioengineering*, 1(11):788–790, 2023.

[132] Alexander Connor, Caleb Wigham, Yang Bai, Manish Rai, Sebastian Nassif, Mattheos Koffas, and R Helen Zha. Novel insights into construct toxicity, strain optimization, and primary sequence design for producing recombinant silk fibroin and elastin-like peptide in e. coli. *Metabolic Engineering Communications*, 16:e00219, 2023.

[133] Anna M Duraj-Thatte, Avinash Manjula-Basavanna, Jarod Rutledge, Jing Xia, Shabir Hassan, Arjirios Sourlis, Andrés G Rubio, Ami Lesha, Michael Zenkl, Anton Kan, et al. Programmable microbial ink for 3d printing of living materials produced from genetically engineered protein nanofibers. *Nature Communications*, 12(1):6600, 2021.

[134] Yanbin Ma, Yao Ding, Xianqiang Song, Xiaochuan Ma, Xun Li, Ning Zhang, Yunpeng Song, Yaping Sun, Yuqing Shen, Wenge Zhong, et al. Structure-guided discovery of a single-domain antibody agonist against human apelin receptor. *Science advances*, 6(3):eaax7379, 2020.

[135] T Jarrod Smith, Holger Sondermann, and George A O'Toole. Type 1 does the two-step: type 1 secretion substrates with a functional periplasmic intermediate. *Journal of Bacteriology*, 200(18):10–1128, 2018.

[136] J-M Nicaud, N Mackman, L Gray, and IB Holland. The c-terminal, 23 kda peptide of e. coli haemolysin 2001 contains all the information necessary for its secretion by the haemolysin (hly) export machinery. *FEBS letters*, 204(2):331–335, 1986.

[137] Lisa Ann Burdette, Samuel Alexander Leach, Han Teng Wong, and Danielle Tullman-Ercek. Developing gram-negative bacteria for the secretion of heterologous proteins. *Microbial cell factories*, 17:1–16, 2018.

[138] B Kenny, R Haigh, and IB Holland. Analysis of the haemolysin transport process through the secretion from escherichia coli of pcm, cat or β-galactosidase fused to the hly c-terminal signal domain. *Molecular microbiology*, 5(10):2557–2568, 1991.

[139] N Mackman, K Baker, L Gray, R Haigh, JM Nicaud, and IB Holland. Release of a chimeric protein into the medium from escherichia coli us-

ing the c-terminal secretion signal of haemolysin. *The EMBO Journal*, 6(9):2835–2841, 1987.

[140] Hyunjong Byun, Jiyeon Park, Sun Chang Kim, and Jung Hoon Ahn. A lower isoelectric point increases signal sequence–mediated secretion of recombinant proteins through a bacterial abc transporter. *Journal of Biological Chemistry*, 292(48):19782–19791, 2017.

[141] Kamonchanock Eungrasamee, Peter Lindblad, and Saowarath Jantaro. Triple-gene overexpression of the acra-acrb-tolc transporter system in synechocystis sp. pcc 6803 contributes to a higher secretion of free fatty acids in response to nitrogen shortage and salt stress. *International Journal of Molecular Sciences*, 25(22):12131, 2024.

[142] Zhigang Zhang, Yuanzhao Ding, and Shunzhi Qian. Influence of bacterial incorporation on mechanical properties of engineered cementitious composites (ecc). *Construction and Building Materials*, 196:195–203, 2019.

[143] Martin Obst, Jian Wang, and Adam P Hitchcock. Soft x-ray spectrotomography study of cyanobacterial biomineral nucleation. *Geobiology*, 7(5):577–591, 2009.

[144] S Schultze-Lam, G Harauz, and TJ Beveridge. Participation of a cyanobacterial s layer in fine-grain mineral formation. *Journal of Bacteriology*, 174(24):7971–7981, 1992.

[145] Thomas C Boothby, Hugo Tapia, Alexandra H Brozena, Samantha Piszkiewicz, Austin E Smith, Ilaria Giovannini, Lorena Rebecchi, Gary J Pielak, Doug Koshland, and Bob Goldstein. Tardigrades use intrinsically disordered proteins to survive desiccation. *Molecular cell*, 65(6):975–984, 2017.

[146] Benjamin AE Lehner, Dominik T Schmieden, and Anne S Meyer. A straightforward approach for 3d bacterial printing. *ACS synthetic biology*, 6(7):1124–1130, 2017.